COLLECTIVE COHERENT BEHAVIOR AND

CLASSICAL ANALOGUE OF QUANTUM

PHENOMENA IN TERAHERTZ METASURFACES

By

NINGNING XU

Bachelor of Science in physics
Jilin University
Changchun, Jilin
2006

Master of Science in photonics and technology
Nankai University
Tianjin, P.R. China
2010

Submitted to the Faculty of the
Graduate College of the
Oklahoma State University
in partial fulfillment of
the requirements for
the Degree of
DOCTOR OF PHILOSOPHY
May, 2016

COLLECTIVE COHERENT BEHAVIOR AND

CLASSICAL ANALOGUE OF QUANTUM

PHENOMENA IN TERAHERTZ METASURFACES

Dissertation Approved:

Dr. Weili Zhang
_____
Dissertation Adviser

Dr. Daniel R. Grischkowsky
_____

Dr. Daqing Piao
_____

Dr. James P. Wicksted
_____

ACKNOWLEDGEMENTS

First and foremost I would like to express my deepest gratitude to my advisor Dr. Weili Zhang. Words cannot express my gratitude to Dr. Zhang, who accepts me as a Ph. D. student in my tough time in pursuit of the Ph. D. I appreciate all his contributions of trust, concern, training, and support to make my Ph. D. experience productive and stimulating. His enthusiasm for research and wonderful working atmosphere in his group are contagious and motivational for me. Dr. Zhang's knowledge, hard-working and academic attitude foster my development forever in my career and life.

I wish to express my special appreciation and thanks to Dr. Ranjan Singh. He provides me with continuous guidance during my whole candidature period. Many fruitful discussions with him helps me to overcome the difficulties in my work. I cannot express enough thanks to Dr. Singh for encouraging my research and for inspiring me to grow as a research scientist. His advices on my career as well as my life have been invaluable.

I am also privileged to have had Dr. Daniel Grischkowsky as a mentor and a member in my dissertation committee. His passion for research and positive attitude are extremely motivational. I would also like to thank Dr. Daqing Piao, Dr. James Wicksted, and Dr. Girish Agarwal for contributing their knowledge and support throughout my research projects and also for their detailed reviews of my thesis and kind comments.

Other past and present group members that I have had the pleasure to work with and alongside of are Dr. Xinchao Lu, Dr. Yongyao Chen, Dr. Wei Cao, Leena Singh, Alisha Shutler and Dr. Mahboubeh Mandehgar; and the visiting scholars, Dr. Quan Li, Siyu Tan, Xiang hu, Dr. Liang Wu, Dr. Zhiyong Wang, Dr. Fangrong Hu, Dr. Jingjing Zheng, Dr. Lin Chen, Min Chen and Dr. Xi Gao. I also want to thank my collaborators, Dr. Xueqian Zhang, Dr. Kenan Qu, Longqing Cong and Xiaoqiang Su. Thank you all for their helpful contributions to my research.

Lastly, I would like to thank my family for all their loves, encouragements, and sacrifices that they have made on my behalf. And most of all, for my beloved husband Yihong, your true love and support over the past years helped me overcome all obstacles and reach where I am today. To my beloved son Ryder Yang, I would like to express my thanks for being such a good boy and always cheering me up. Thank you!

Name: Ningning Xu

Date of Degree: MAY, 2016

Title of Study: COLLECTIVE COHERENT BEHAVIOR AND CLASSICAL ANALOGUE OF QUANTUM PHENOMENA IN TERAHERTZ METASURFACES

Major Field: PHOTONICS

Abstract: Metasurfaces made of subwavelength resonators exhibit exotic optical properties which do not exist in natural materials. Several of the unique properties of metasurfaces depend on the nearest neighbor interactions in the lattice which is important for the fundamental understanding their effective medium behavior. The collective coherent behavior influenced by the nearest-neighboring meta-atoms interactions in metasurface system has been rarely probed in the past. Therefore, in this thesis, I study the collective coherent behavior in meta-atoms dominated by the near-field and the far-field interactions in the lattice. The interaction effects have been studied in two fundamentally different metasurface systems: Lorentzian and Fano resonant meta-atoms. I identified universal behavior in both types of resonant metasurfaces, where in the Lorentzian resonator, the resonant shift due to nearest neighbor interaction decays exponentially as the lattice constant increases. While, in the Fano meta-atoms, I observed an exponential decay of the Fano resonance linewidth with a universal decay constant as the lattice constant was increased. Apart from the near-field coupling, I also studied the far-field diffraction mode mediated coupling in meta-atoms. Through diffraction mode management, I show that each of the eigenmodes of a Lorentzian resonator can be tailored by matching the fundamental diffractive mode of the lattice. Furthermore, by using these tricks to couple meta-atoms, I designed experiments to demonstrate classical analogue of quantum phenomena such as electromagnetically induced transparency and absorbance by coupling resonance modes of different Lorentzian and Fano resonators. The understanding and the discovery of the universal behavior of coupling effects in this thesis would provide future directions to design efficient metasurface lattices with applications in optical switches, narrow-band filters, modulator and quantum information processing devices across the broad electromagnetic domain extending to radio waves, microwave, terahertz, infrared and optical regimes.

TABLE OF CONTENTS

LIST OF FIGURES

ix

LIST OF SYMBOLS

LC	Inductive-capacitive
TDS	Time-domain spectroscopy
A	Resonance amplitude
c	Velocity of light in free space
SRR	Spilt-ring resonator
l	Length of the resonator
g	Gap of the SRR
P	Periodicity (μm)
P/l	Scaling periodicities
f	Frequency (THz)
$\varDelta f$	Frequency shift
f_0	Intrinsic frequency
λ	Wavelength (μm)
σ	Conductivity
ε	Permittivity
μ_0	Permeability in vacuum
a	Asymmetry degree of the Fano resonator
t	Time decay constant
FDTD	Finite-difference time-domain
Q factor	Quality factor
CMR	Coherent metasurface rule

Q_i	Charges on the location i
$\mathcal{L}$	Lagrange expression
T	Kinetic energy
V	Potential energy
M_H	Mutual magnetic inductance
k_H	Magnetic inductance coupling coefficients
t	Transmission coefficient
r	Reflection coefficient
n	Refractive index
(i,j)	The order of the diffraction mode
P_c	Critical periodicity
EIT	Electromagnetically induced transparency
DEIT	Double electromagnetically induced transparency
ASRR	Asymmetric split-ring resonators
ω	Angular frequency (rad/s)
χ	Susceptibility
δ	Frequency detuning
Ω	Rabi frequency
ρ_{i0}	Density matrix elements
γ	Damping rate
φ	Phase shift (radian)
ε_{eff}	Effective permittivity
μ_{eff}	Effective permeability
κ	Coupling coefficient

CHAPTER I

INTRODUCTION

1.1 Introduction of metamaterial and metasurface

Metamaterials, artificially made by manipulating subwavelength meta-atoms, exhibit unique electric and magnetic properties by engineering permittivity and permeability not attainable in naturally exiting materials. For more than a decade, the metamaterial-based novel photonic device study has been focused on developing reproducibility in the classic and quantum phenomena to replace the conventional bulk materials. The composition components, i.e. subwavelength metamolecules, contribute to light behavior manipulation, leading to numerous studies spurred by novel applications, such as negative refractive index materials, invisible cloaks, super lens beyond diffraction limitation, active photonics and nanoscale photolithography, ultrafast data processing and communications in the optics, terahertz and microwave regimes [1-15].

More recently, followed by the rapid development of the metamaterials, metasurfaces stand out, as the two-dimensional arrays of subwavelength elements have attracted enormous interest due to the reduction of the complex techniques required in the fabrication of three-dimensional metamaterials. Endowed with the artificial planar arrangement of the metamolecules, the interesting physics and optical properties which are limited by rigorous experimental condition are capable of being realized.

in metasurface systems, such as lasing spasers, electromagnetically induced transparency and absorption, complex wave front shaping and parity-time symmetry [16-22]. In this dissertation, we will first study the fundamental exploration of the near-field coupling effect in nearest neighboring resonators, which leads to a collective coherent behavior of the structured periodic lattice on a metasurface. A coherent metasurface ruler is identified to predict the fractional frequency shift with the scaling periodicities in LC and Fano arrays, respectively. In addition to the near-field coupling, far-field coupling diffraction mode management are demonstrated in tailoring the lineshape of all eigenmode resonances. These studies facilitate the design on calibrating the spectral tuning response and optimizing it to reach low radiation loss. Finally, through the near and far-field coupling, we mimic the quantum optics phenomena of the electromagnetically induced transparency and absorption in the metasurface systems. This opens a new avenue to promising applications in light storage and filtering, slow light, and terahertz communications.

1.2 Scope

The metasurface consists of periodic subwavelength metamolecules, and several thousands of the unit cells behave collectively to manipulate the light propagation by reshaping the incident terahertz pulse. Not only do the configuration and dimensions of the metamolecules determine the electromagnetic properties of the metasurface, the interactions either between the neighbors or between different types of resonators within the unit metamolecule are another essential key to dominate their optical properties. In the terahertz region with wavelength around 300 μm, the separations between the metamolecules are usually much shorter than the interactive radiation wavelength, which renders a strong light-matter coupling effect in the metasurface.

We choose two fundamental subwavelength resonator models, namely the Lorentzian resonators and Fano resonators, to study the near-filed coupling in the nearest neighbors by observing a frequency shift

and the linewidth modulation. We identified a coherent metasurface plasmon ruler in the fractional frequency shift and linewidth from their collective coherence behavior for the two types of resonators. Other than the near-field coupling, we found that the far-field diffraction coupling plays an important role in the collective coherent behavior. Through the lattice mode matching, the Q factors of all three eigenmodes of the Lorentzian resonator have been tailored by engineering the periodicities. Next, by designing a planar coupling scheme comprised of the Lorentzian and Fano resonator, we tailored the electromagnetically induced transparency and absorbance through the near-field and far-field coupling. Finally, by exploring the vertical near-field coupling of the metamolecules between tiers in a three-layer metasurface system, we observed an analogue of electromagnetically induced absorption. In a unit cell, the SRR altered the phase of the two dipole resonators to out-of-phase, which lead to magnetic field trapping of the incident wave.

1.3 Outline

The outline is illustrated as follows:

Chapter I, I presents a brief introduction of the metamaterial and metasurface, followed by the scope and outline.

In Chapter II, We present the near-field coupling in the nearest neighbors of the Lorentzian resonators. As a result of the mutual inductance coupling between the SRR, the frequency red-shift of the LC resonance is observed when there is an increase in the lattice constants. Furthermore, we investigated on the decay rates in terms of the linewidth versus the periodicities and demonstrated that they obey the exponential decay.

In Chapter III, another important fundamental resonance mode with asymmetric line shape feature, i. e. the Fano resonance is investigated in the nearest neighbor coupling region. The basic distinct

characteristics of the Lorentzian and Fano mode are illustrated from the prospective of the magnetic and electric dipoles excitation. We observed a frequency red-shift with the linewidth varying in exponential decay in the Fano resonator similar with the findings in the Lorentzian resonator.

In Chapter IV, we conclude the universal behavior in metamaterials by identifying a universal plasmon ruler in the form of fractional frequency shift versus scaling periodicities in the Lorentzian and Fano resonator based on the mutual inductance model and Lagrangian model. In addition, we observed a universal behavior of the linewidth evolution in Fano resonance for three different sizes of the Fano resonator arrays. However, this size-independent linewidth exponential behavior can only be applied in the Fano resonator instead of the Lorentzian resonator.

In Chapter V, we conclude that one of the most efficient way is the diffraction mode management, which can depress the radiation loss and increase the Q factor of the resonance consequently. The diffraction management is demonstrated to be of universal applicability to subwavelength resonators in metasurface system, which is suitable to various resonant modes and diverse resonators' dimensions. The diffraction mode highly depressed the radiation loss of the Lorentzian (n = 1), Dipole (n = 2) and Quadrupole (n = 3) modes. An order of magnitude enhancement in Q factor is achieved by tuning the far-field diffraction through engineering the periodicities. Our work opens a new promising approach on optimization of the design for photonics devices.

In Chapter VI, we demonstrate dual transparency bands with a strong absorbance by coupling an electromagnetically induced transparency peak to a Lorenztian inductive-capacitive resonance in the system due to interference between a bright mode and two dark states. The absorbance spectra are theoretical calculated based on density matrix equations in a four-level tripod quantum interference system. The analogue of the two dark modes are defined as the trapped mode resonance due to asymmetry of the double gap asymmetric Fano resonator and a single gap split-ring-resonator. The proposed metamaterial structure with dual transprency band feature facilitates potential applications in

planar metasurface sensors, light switch, filter and modulator, and light storage in telecommunication networks.

In Chapter VII, we present the manifestation of the electromagnetically induced absorption analogue due to constructive interference in a vertically coupled three-resonator metasurface system that consists of two bright and one dark resonator. The absorption resonance is developed in the electromagnetically induced transparency window due to magnetic resonance induced by the near-field coupling of the three resonators. Theoretical analysis shows that the absorption arises from a magnetic resonance induced by the near-field coupling of the three resonators.

In Chapter VIII, a brief conclusion is reported, followed by a subsequent future plan. We will continue to probe the collective coherent behavior dominant abrupt phase change due to the modulation of absorptive and radiation loss based on a dual-band Fano shape absorber. An experiment on active control of the Fano-lorentzian coupling is proposed and scheduled.

CHAPTER II

NEAR-FIELD COUPLING IN NEAREST NEIGHBOR COUPLED LORENTZIAN

RESONATORS

2.1 Introduction and background

Metasurfaces have undergone a rapid development in the area of subwavelength artificial materials, which modulated the electromagnetic waves with discretionary design not allowed in naturally existing materials. Compared to three-dimensional metamaterials, the fabrication process of metasurfaces, i.e. the two-dimensional thin patterned film on the substrate, is substantially simplified. Diverse functions are attainable in the metasurfaces such as: lasing spaser, arbitrary phase control antennas, hologram, anomalous reflection and complex wave front shaping [16,17,20,23-29]. Lasing spaser was first proposed by Zheludev et al. [16] It is defined as the spatial and temporal coherent radiation source generated from the coherent current in two-dimensional resonator arrays [16]. Such nearest neighbor coupling among the metamaterial resonators in a large array can significantly affect the collective coherent behavior of the metasurfaces.

In recent years, there has been tremendous development in understanding the inter resonator near-field coupling between dipolar resonator pairs in two-dimensional and three-dimensional plasmonic arrays that have also resulted in excellent plasmonic rulers to determine the separations

between the dipolar metal particles. Depending on the varying coupling strength between the resonator, the spectral response of the system is predicted successfully [30-36]. However, the studies on probing the coherent collective behavior of nearest neighbor coupled plasmonic resonators are rare [37-40]. In this scheme, all the individual resonators in the entire lattice are coupled to its nearest neighbor through their near fields [41-48]. The nearest neighbor coupling leads to a coherent behavior of the structured periodic lattice where the scattered near-field of each resonator in the array determines the response of the plasmonic metamaterials. Here we selected the common subwavelength resonator model: split-ring resonators (SRR) to study the collective coherent behavior of the nearest neighbor coupling in two dimension arrays. The SRR is an ideal analog of the LC circuit, which is comprised of an inductor and a capacitor without the dissipation loss from the resistance. Thus, the circular surface currents conserved in the SRR are characterized as a high Q factor LC resonance in the optical regime with low radiation loss. The collective spectral shift of LC resonance show an exponential decay due to the nearest neighboring mutual inductance coupling. Furthermore, we demonstrated that the linewidth versus the periodicity showed an exponential decay curve.

2.2 Sample design and preparation

In order to cover a broad terahertz range from 0.5-1.5 THz, three differently sized SRR sets of 18, 22 and 36 μm in side length were chosen. For the 18 μm SRR size, we fabricated samples with periodicities ranging from 60 to 25 μm; for the 22 μm SRRs the period varied from 90 to 27 μm; and for the 36 μm side length of SRRs, the sample period varied from 180 to 40 μm in a decreasing order. Figure 2-1(a) exhibit the schematic unit cell of the SRR with dimensions: l = 18 μm (22 μm, 36 μm), g = 3 μm and w = 6 μm. The microscopic images of the fabricated SRR samples with sizes of 22 and 36 μm with varying periodicities are showed in Figures 2-1(b) and 1(c). The SRR metasurface with area 10 mm × 10 mm for each pattern was fabricated by a conventional photolithography technique.
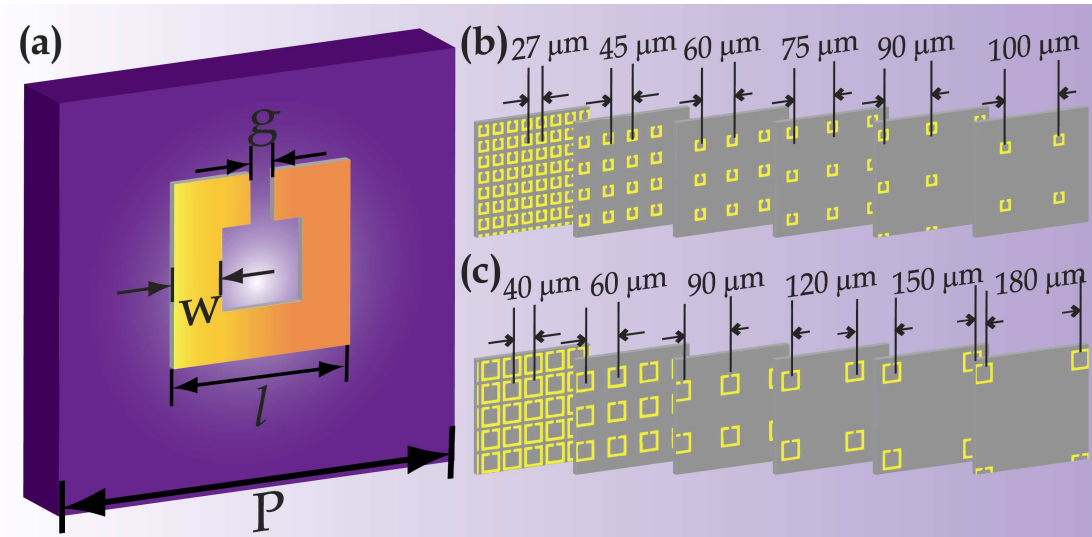
Figure 2-1. Schematic and microscopic images of the metasurface samples (a) Schematic unit cell of the SRR with dimensions: l = 18 µm (22 µm, 36 µm), g = 3 µm and w = 6 µm. (b) Microscopic images of the 22 µm SRR arrays with varying periodicities P: 27, 45, 60, 75, 90 and 100 µm. (c) Microscopic images of the 36 µm SRR arrays with varying periodicities P: 40, 60, 90, 120, 150 and 180 µm (figure adapted from Ref. [48]).

First, we used S1813 positive photoresist to spin coat about 1.5 μm thickness layer on the 640 thick μm

n-type Si substrate with a resistivity of 12 Ohm·cm. Then the sample was exposed to the G-line light

(435 nm) under the dark field structured photo mask, followed by the development process. After

development, the patterned Si wafer was deposited with 200 nm thick aluminum and the bottom

photoresist was lifted-off [48].

2.3 Experimental set-up

We employed an *8f* confocal terahertz time-domain spectrometer (THz-TDS) to measure the amplitude

transmission of the SRR samples and the blank silicon wafer as the reference. The Ti:sapphire laser

pulse with repetition rate 88 MHz, 26 fs, 800 nm shorts the photoconductive antenna gap and radiates

the terahertz wave, as shown in Figure 2-2[49,50]. Excited by the 10 mw optical pulse, the THz

radiation is collected by a silicon lens, passing through an *8f* confocal system consisting of four

parabolic mirrors. The metasurface sample 10 mm × 10 mm is placed at the middle focal plane of the

8f system, where the frequency-independent beam waist is focused to 3.5 mm. The induced time-

dependent voltage across the antenna is measured by shorting the gap with the optical pulse versus the

time delay between the excitation and detection laser pulses. We performed a 17 ps length time delay

scan with 57 GHz resolution in the frequency domain. By using Fourier transform, the frequency-

domain spectrum is obtained from the time-domain signal. Then, the final transmission amplitude is

given $|E_s(\omega)/E_r(\omega)|$ by an average of three measurements.
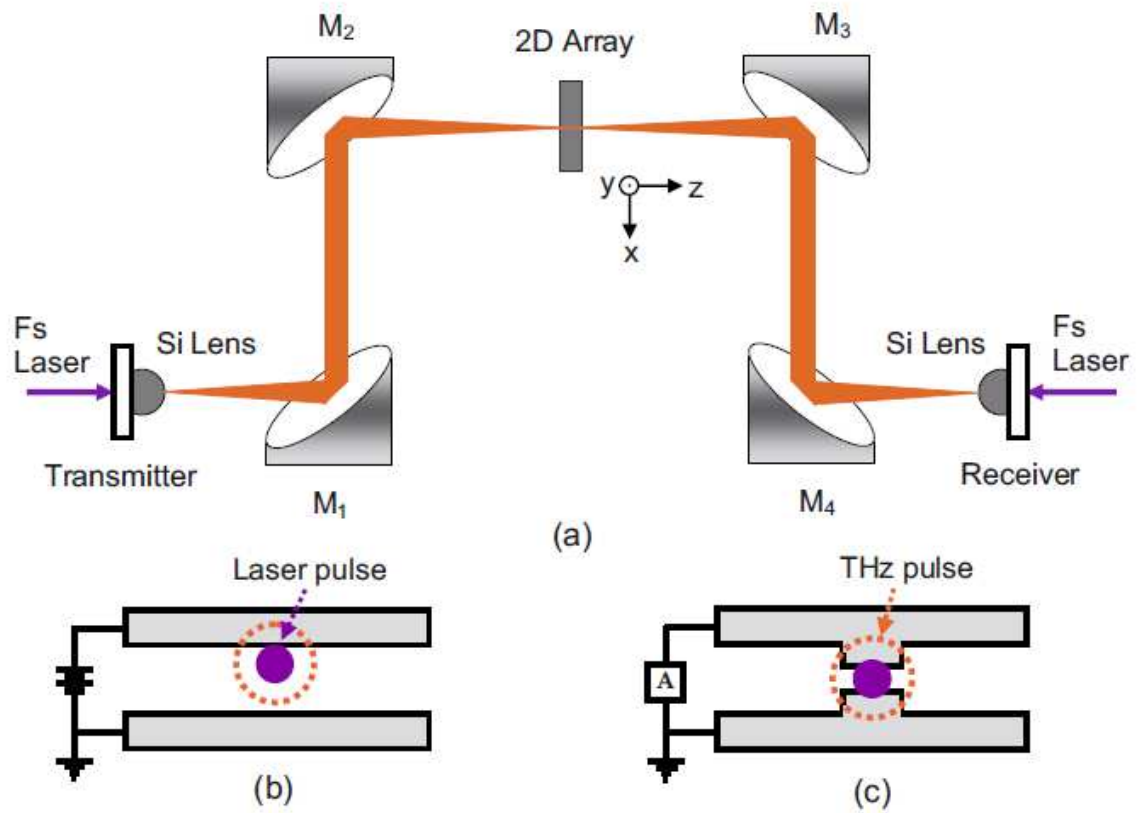
Figure 2-2. Schematic of the *8f* terahertz time-domain spectroscopy (a) *8f* confocal THz-TDS experimental set-up. (b) Transmitter. (c) Receiver (figure adapted from Ref. [50]).

2.4 Simulated and measured result

We use CST Microwave studio frequency domain solver to simulate the transmission amplitude for all the three differently sized SRRs with various lattice constants. Frequency-domain solver on tetrahedral mesh with the boundary conditions set as unit cell for metasurfaces plane and open (add space) for terahertz wave propagation direction. The lossy aluminum with $\sigma = 3.56 \times 10^7$ S/m and lossy silicon with $\varepsilon = 11.96$ are used in the simulation. Figures 2-3(a), 3(b) and 3(c) show the respective transmission response of the 18, 22 and 36 μm sized SRRs with various lattice constants. Normally, the frequency of the LC resonance is determined by the absolute dimensions of the square SRRs, which is expressed as $f = 1/2\pi \, (LC)^{1/2}$. We observe a common trend in all three differently sized SRR sets. The blue shift of the LC resonances persists with the decrease in the period of each of the differently sized SRR metasurfaces. The measured transmission spectra validates the simulated results by showing identical behavior in Figure 2-4(a), 4(b), and 4(c) for the 18, 22 and 36 μm sized SRRs, respectively. The blue shift of the LC resonances in all of the differently sized SRRs with varying periods happens due to enhanced near-field coupling among the nearest neighbors. With the decrease in the lattice constant, the nearest neighbor SRRs give rise to stronger mutual inductance due to overlap of the magnetic flux that is generated from the circulating currents in the SRRs at the LC resonance frequency. As a result of overlapping magnetic flux, the net inductance of the individual SRR given by $L = Ls - M$ reduces with Ls being the self-inductance and M being the mutual inductance between the nearest neighbors. Thus, the decrease in periodicity leads to the increase in the mutual inductance of the SRRs that causes the blue shift of the LC resonance in all the differently sized SRR sets. The kink at ~ 1.45 THz for 60 μm period in Figures. 2-3(a), 3(d) is due to the fundamental order diffractive mode that depends on the index of the substrate and the period of the structure [41].

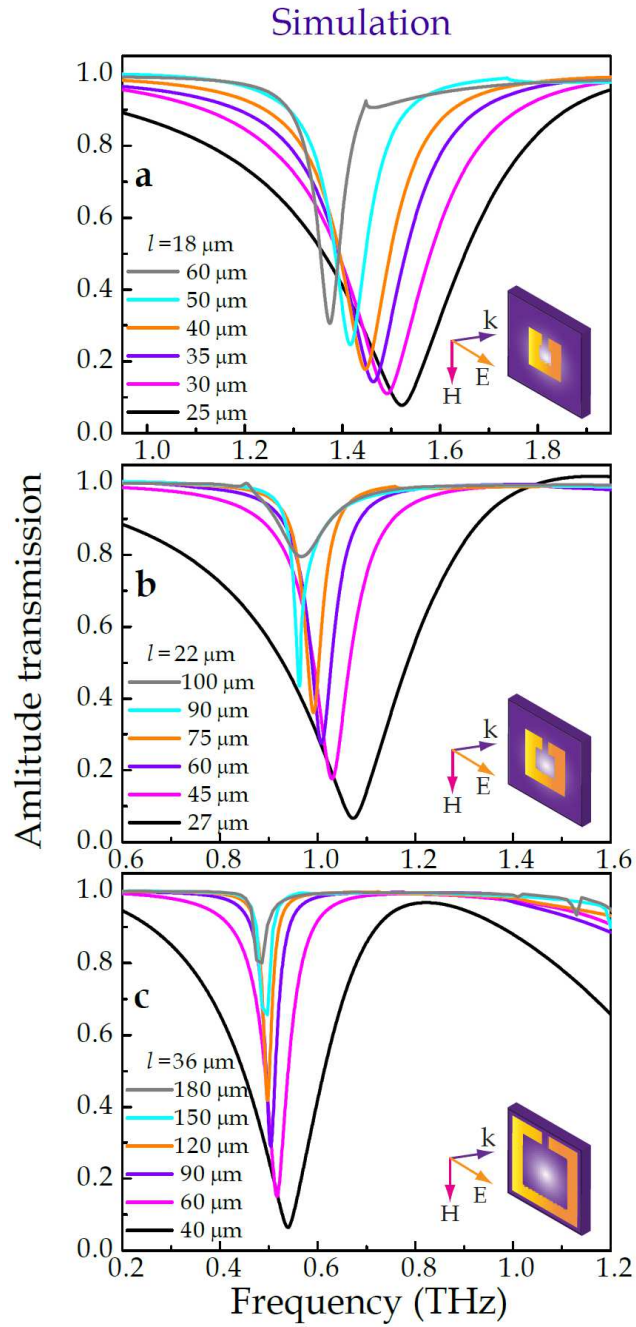**Figure 2-3**. Simulated amplitude transmission. (a), (b) and (c) Simulated LC resonance of the 18, 22 and 36 μm SRR with varying periodicities, respectively.
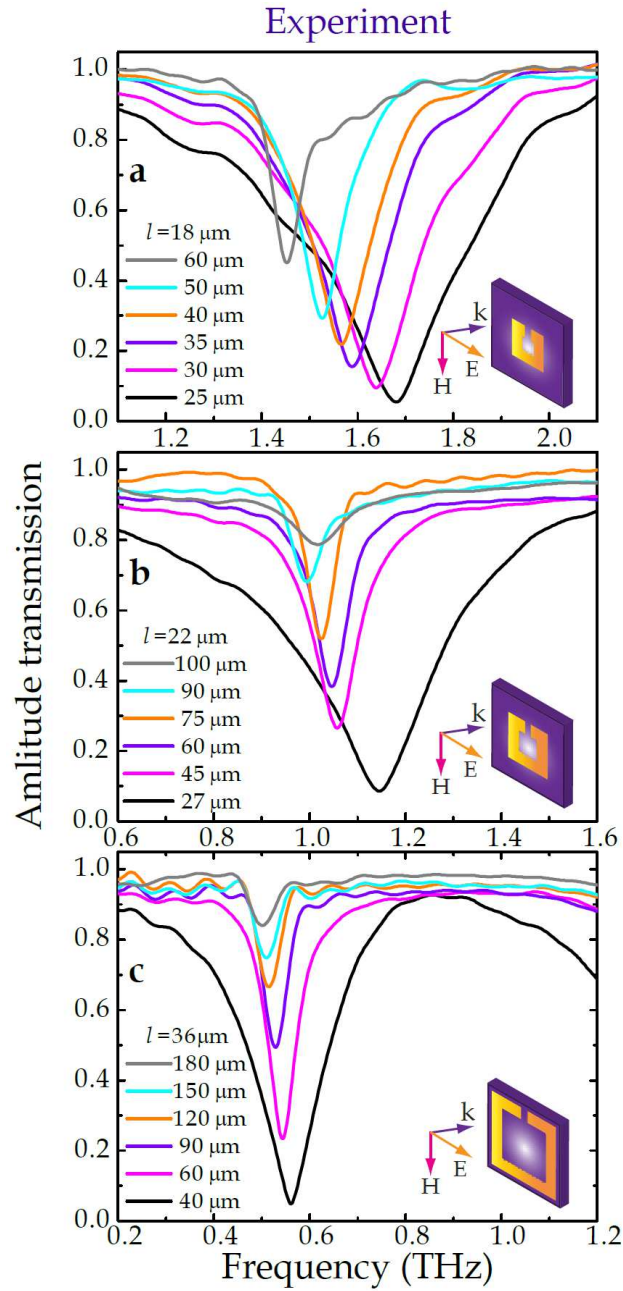
Figure 2-4. Measured amplitude transmission. (a), (b) and (c) measured LC resonance of the 18, 22 and 36 μm SRR with varying periodicities, respectively.

2.4 Data analysis

To analyze the LC resonance shifts in all three differently sized SRR with varying lattice constants we define the relative frequency shift as $\Delta f = f - f_0$, where f_0 is the intrinsic uncoupled LC resonance of the SRRs at the largest periodicity. The intrinsic frequency f_0 of 18, 22 and 36 μm SRRs is the frequency of LC resonance $f_{01} = 1.37$ THz, $f_{02} = 0.97$ THz and $f_{03} = 0.56$THz at 60, 100 and 180 μm periodicities, respectively, when excited by normally incident terahertz wave with electric field polarized along the gap arm of the SRRs. Figures 2-5(a) and 5(b) show the simulated and measured frequency shift as a function of periodicity. We notice that the frequency shift in these SRRs decrease exponentially with an increase in the lattice periodicity but with a different decay constant which we address here as exponential decay length. The frequency shifts were fitted to exponentially decaying curves with a general behavior of exponential decay lengths $y = Ae^{-x/a}$, as shown in Figures 2-5(a) and 5(b). The simulated exponential decay lengths $a_1 = 18.52 \pm 1.58$ for the 18 μm SRRs, $a_2 = 31.90 \pm 2.41$ for the 22 μm SRRs and $a_3 = 58.29 \pm 4.48$ for the 36 μm SRRs while the respective decay lengths from the measurements were found to be $a_1 = 18.26 \pm 2.87$, $a_2 = 25.16 \pm 3.80$, and $a_3 = 55.14 \pm 4.69$. The exponential decay lengths are largest for the biggest SRRs which signifies that the magnetic flux from individual SRR extends over much larger distances in case of bigger SRRs and the nearest neighbors begin to interact at comparatively larger lattice periods. The exponential rise in the frequency blue-shift of smaller sized SRRs with decreasing periods indicates stronger coupling in smaller SRRs where the mutual inductance tends to increase very sharply at close nearest neighbor distances. The decay lengths are shorter in the case of smaller SRRs since the near-field coupling in the lattices is absent in the case of larger periodicities because the magnetic flux of each SRR does not extend up to the magnetic flux of the nearest neighbors and thus they tend to behave as uncoupled nearest neighbors at larger periods. On the other hand, the nearest neighbor coupling in larger SRRs extends over larger periodicities and the blue-shifting of the LC resonance is not as sharp as it is for the smaller SRRs.
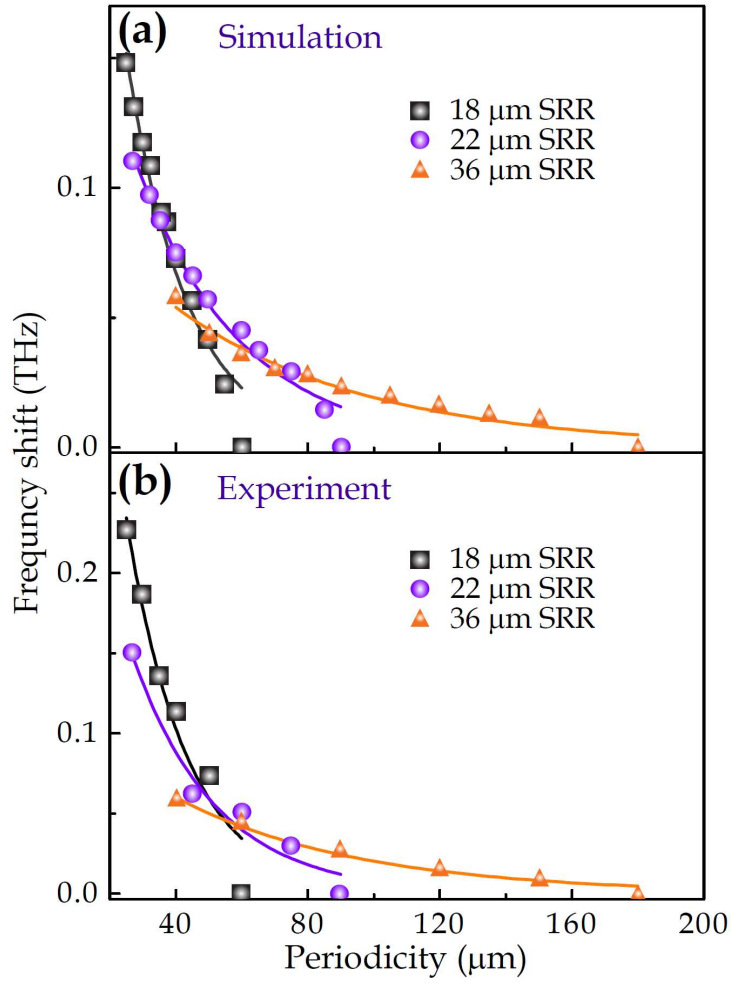
Figure 2-5. Frequency shift with respect to the periodicities (*P*). (a), (b) The simulated and measured frequency shifts of the SRR arrays as a function of periodicities and their exponential decay fitting curves $y = A\,e^{-x/a}$ for 18 (black), 22 (violet) and 36 μm (orange) SRR.

From the simulated and measured transmission spectra, it is clearly shown that there is a distinct difference of the linewidth in the LC resonance between the large and small lattice constants of the SRR arrays. Figure 2-6 shows the simulated linewidth varying with the increase in the periodicity, which is not attainable in the experimental data due to the limitation of the scan resolution. It is worth noting that the linewidth of the resonance keeps narrowing as we increase the periodicity. The dense packing of the resonators results in a hybridization state composed of numerous degenerate levels, which leads to a broadening of the resonance. While in the resonator array with larger periodicity, the isolated resonator renders the energy level more tightly compared to the coupled arrays. It leads to a relative narrow linewidth with more confined electric and magnetic fields. The simulated linewidths exhibiting an exponential decay behavior with respect to the periodicity manifest the near-field coupling field of the neighboring subwavelength resonators interactions obey a decay behavior as the evanescent wave. The corresponding exponential decay curve are indicated as the solid line for 18 (black), 22 (violet) and 36 μm (orange) SRR with the decay rate $t_1 = 13.4 \pm 1.5$ for the 18 μm SRRs, $t_2 = 14.4 \pm 1.6$ for the 22 μm SRRs and $t_3 = 16.2 \pm 2.1$ for the 36 μm SRRs. We observed that the exponential decay rate of the linewidth for the 18 μm SRR persisted with the smallest decay rate, which illustrated that in the smaller resonator, the energy dissipation loss decreases more rapidly than the large resonator. The electromagnetic field from individual SRR extends over a much shorter distance to interact with adjacent neighbors compared to that in the bigger SRRs. Thus we attribute the linewidth versus the periodicities to a size-dependent behavior.
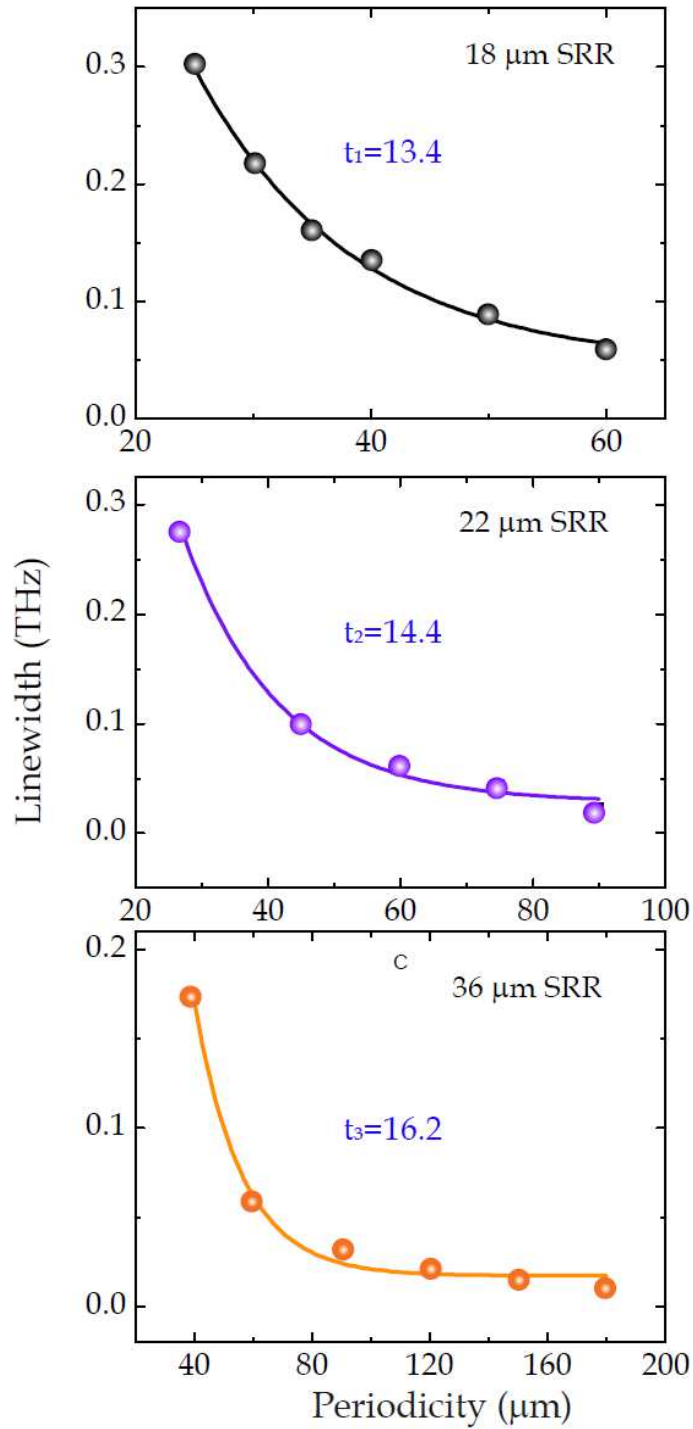
Figure 2-6. Linewidth with respect to the periodicities (*P*). The extracted linewidth of the LC resonance as a function of periodicities from the simulation result and their exponential decay fitting curves $y = Ae^{-x/t} + y_0$ for 18 (black), 22 (violet) and 36 μm (orange) SRR.

2.5 Conclusion

We observed a frequency shift in forms of the exponential decay for all three differently sized SRRs. Near-field coupling of the nearest neighbor can mediate the mutual inductance coupling by observing the LC resonance red shift with the increase in the periodicities in the transmission. The dominant coupling mechanism in our square lattice is magnetic in nature. Furthermore we study the mechanism of the linewidth gradually varying with the respect of the lattice constant from the prospective of the energy levels hybridization. The size-dependent dissipation loss feature is pointed out by showing the different exponential decay rates of the linewidth in three sets of the SRR arrays.

CHAPTER III

NEAR-FIELD COUPLING IN NEAREST NEIGHBOR FANO RESONATORS

3.1 Introduction and background

Lorentzian resonance can be applied to fit various resonant modes according to the symmetric linewidth nature. Apart from this fundamental symmetric feature of the resonance, the other fundamental resonance with asymmetric feature is essential to explain the mode nature with the asymmetric principle. It was first demonstrated by Ugo Fano in 1961, where a pronouncedly asymmetric peak in excitation spectra was observed by the interference of discrete levels with a continuum energy level in theoretical physics [51,52]. Then the Fano resonance was extended to various research fields to explain interesting physical observations based on the mechanism of asymmetry.

The Fano resonance has been reported in various systems such as semiconductor quantum dots and quantum wells system by coupling a discrete level and continuum levels, in asymmetrically arranged plasmonic nanoparticles, nano cavities or metallic waveguides with light interference destructively [53-60]. In metamaterial platform the fundamental Fano type resonance can be easily realized in an asymmetric double SRR [61-63]. By breaking the asymmetry between the double gaps of the SRR, a new mode exhibiting the asymmetric lineshape feature, namely the Fano resonance is formed by destructive interference of the surface currents. Distinct from the dipole

resonance, in which the mode induced a constructively interference of the surface currents in the symmetric double-SRRs. The magnetic dipoles are induced from the out-of-phase surface currents perpendicular to the metasurface plane. Consequently, it can hardly couple the external magnetic field to the Fano resonator arrays, since the external magnetic field oscillated in the metasurface plane. This unique property renders a sub-radiative system nature of the Fano resonance, where the re-radiative magnetic field scattered from the individual Fano resonators is repeatedly trapped in the other resonator arrays without radiative to the environment [17]. In recent years, most of the work on the Fano resonance are aimed at tailoring the Fano behavior in the unit of individual resonator such as engineering the degree of the symmetry. There are few works on exploring the collective behavior of the Fano resonance influenced by the nearest neighbor interactions through the near-field coupling.

In this chapter, the fundamental optical properties consisting of the frequency shift and the linewidth varying are demonstrated by engineering the lattice constants of the Fano resonator arrays with holding the constant asymmetry feature. We found that the frequency red-shift with increase in periodicities can be modeled from the Eulerian-Lagrange model. To probe the dissipation loss in this sub-radiative system, we show that the linewidth varies in the form of exponential decay with respect to periodicities. Consistent with the defined sub-radiative system for the Fano system, linewidth dictated by the energy radiation loss is several times lower in the Fano arrays than that in the radiative SRR arrays.

3.2 Sample design

The Fano resonance is excited under normal incidence with the electric field perpendicular to the double gaps of the SRR. Firstly, we performed extensive simulation by using the CST Micro wave studio based on Finite difference time-domain (FDTD) method. Frequency domain solver with boundary conditions set as unit cell for metasurfaces plane is carried out. In the simulation, we set the lossy aluminum with $\sigma = 3.56 \times 10^7$ S/m and lossy silicon with $\varepsilon = 11.96$. Based on the simulation result, we selected three differently sized Fano resonators with the length of 24, 33 and 60 μm with the displacement of the gap assigned as 4, 6 and 10 μm, respectively to adjust the Fano resonance covering from 0.5-1.5 THz. In our scheme, the asymmetry of the Fano resonator is fixed with the asymmetry factor maintained about 9%, which is defined as:

$$a = \frac{l_1 - l_2}{l_1 + l_2} \tag{3-1}$$

where l_1 and l_2 are the perimeters of each arm. Then for the 24 μm Fano resonators, we fabricated samples with periodicities ranging from 60 to 29 μm; for the 33 μm Fano resonators arrays, the period varied from 118 to 39 μm; and for the 60 μm side length of SRRs, the sample period varied from 180 to 70 μm in a decreasing order, as shown in Figure 3-1. The unit cell of the Fano arrays are designed with dimensions: $l = 24$ μm (33 μm, 60 μm), $g = 3$ μm and $w = 6$ μm. The Fano resonator arrays with an area 10 mm × 10 mm for each pattern was fabricated by conventional photolithography technique. The transmitted terahertz spectra of the Fano arrays are measured by photoconductive antenna based 8f confocal THz-TDS with the same blank 640 μm blank silicon wafer as the reference. After Fourier transform, the amplitude transmission is calculated as $t(\omega) = |E_s(\omega)/E_r(\omega)|$ with $E_s(\omega)$ and $E_r(\omega)$ being the transmitted terahertz signals of the sample and the reference.
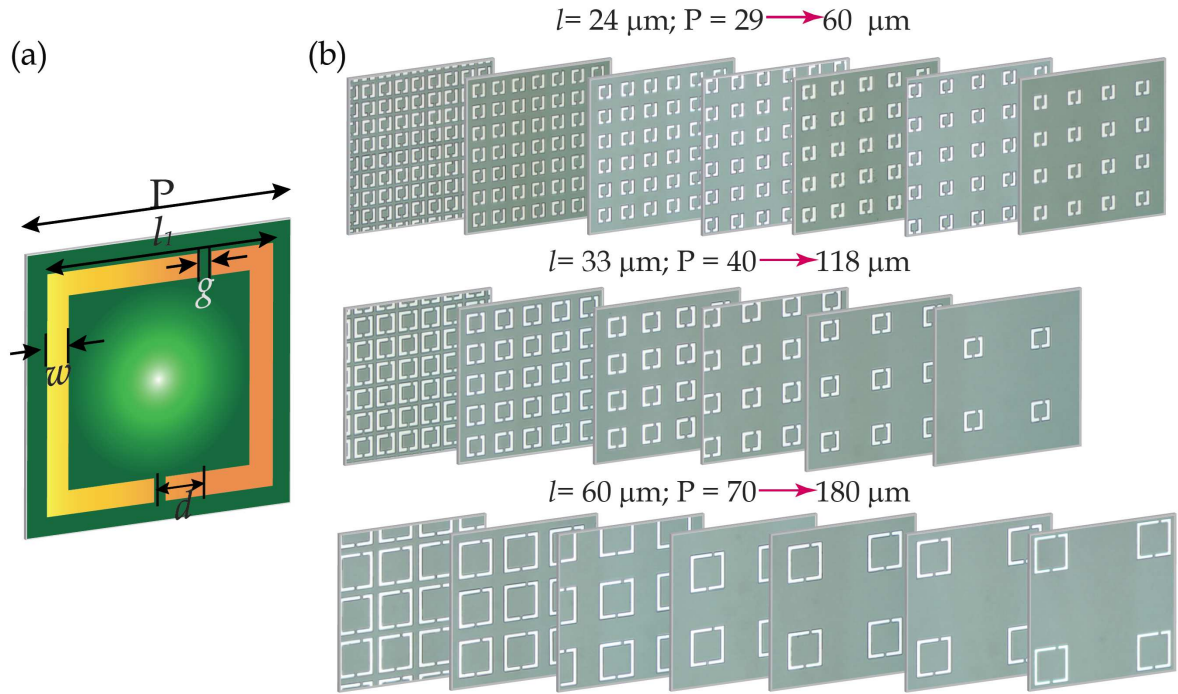
Figure 3-1. Schematic and microscopic images of the metasurface samples (a) Schematic unit cell of Fano with dimensions: $l = 24$ μm (33 μm, 60 μm), $d = 4$ μm (6 μm, 10 μm), $g = 3$ μm and $w = 6$ μm. (b) Microscopic images of the 24 μm Fano arrays with varying periodicities P: 29, 35, 40, 45, 50, 55 and 60μm; 33 μm Fano arrays with varying periodicities P: 39, 50, 60, 70, 90 μm; 60 μm Fano arrays with varying periodicities P: 70, 80, 100, 120, 140, 160 and 180 μm.

3.3 Simulated and measured result

Figures 3-2(a), 2(b) and 2(c) present the simulated amplitude transmission resonance response of the three sets of 24, 33 and 60 μm sized Fano resonator arrays with various lattice constants. It is worth noting that there is a common trend in the spectral response in all three different sized Fano resonator arrays. With increase in the lattice constant, the Fano resonance frequency red-shifts due to weaker near-field coupling between the nearest neighbors. In an individual Fano resonator, the out-of-phase surface currents conserved on the left and right arm induced a strong magnetic coupling dipole. As the lattice period decreases, the nearest neighbor performed the stronger magnetic inductance coupling due to overlap of the magnetic flux, which leads to the Fano resonance moved to a higher frequency. The dense packing Fano resonator arrays with strong magnetic dipole coupling in the nearest neighbors enhanced the degenerate energy levels due to the in-phase magnetic dipole oscillation perpendicular to the array plane [64]. Figure 3-3(a), 3(b) and 3(c) show the measured transmission spectra, which verified the simulated results by showing the similar transmission spectra for the 24, 33 and 60 μm sized SRRs, respectively. In the measured data, the linewidth of the Fano resonance is limited by the material loss and the measurement resolution by showing a relative broader resonance than the simulated transmitted spectra.

Figure 3-2. Simulated amplitude transmission. (a), (b) and (c) Simulated Fano resonance of the 24, 33 and 60 μm SRR with varying periodicities from 29 to 60, 39 to 80 and 70 to 140 μm, respectively.
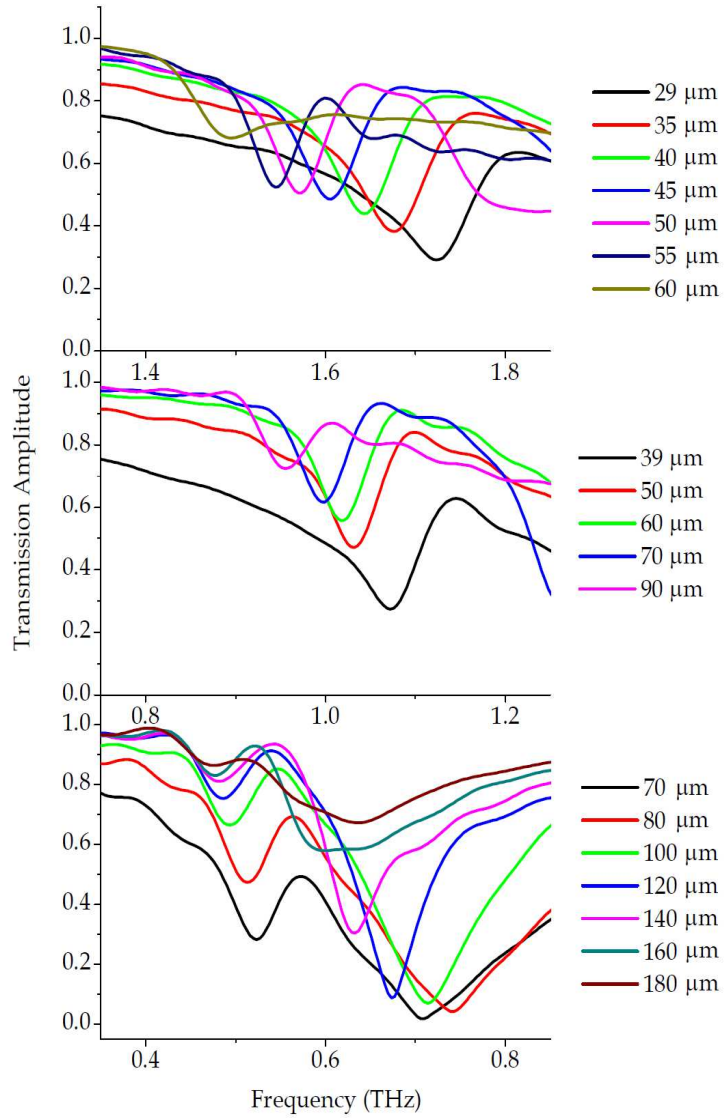
Figure 3-3. Measured amplitude transmission. (a), (b) and (c) Measured Fano resonance of the 24, 33 and 60 μm SRR with varying periodicities from 29 to 60, 39 to 90 and 70 to 180 μm, respectively.
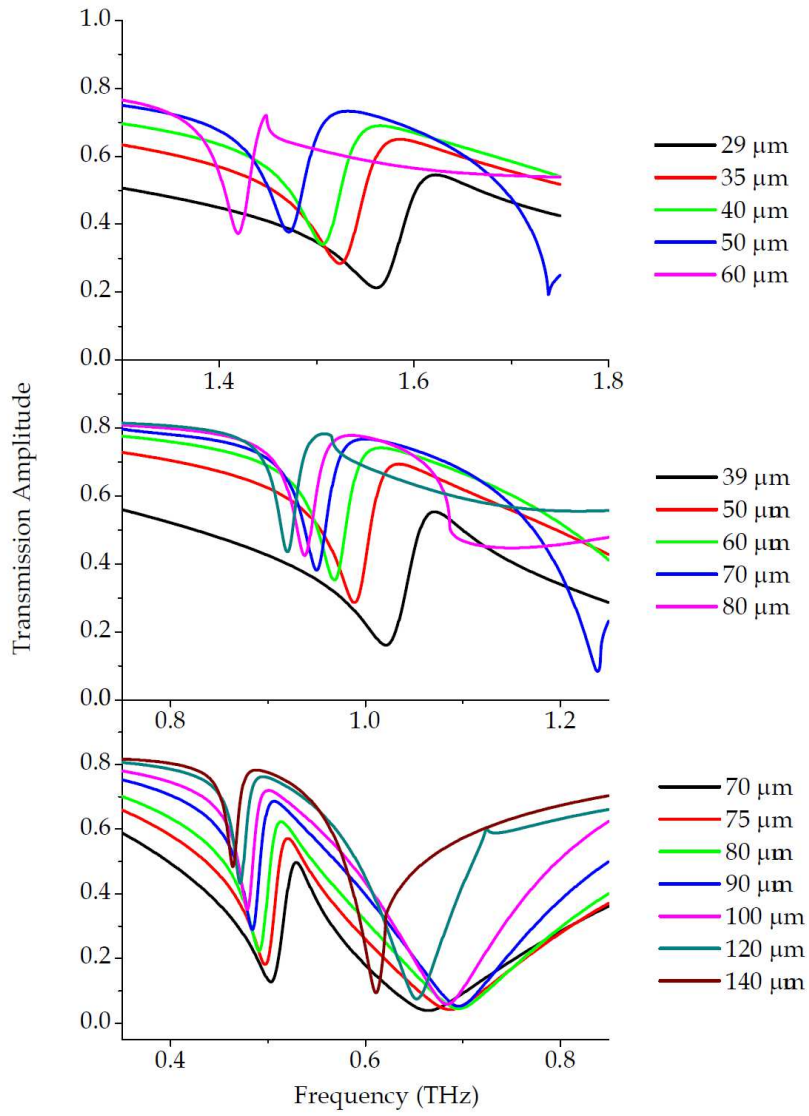
3.4 Data Analysis

In order to further explore the frequency shift of the Fano resonance in all three different sized Fano resonators, we plot the resonance shifts in all of the Fano resonator sets with varying periodicities. The frequency shift calculated as $\Delta f = f - f_0$, where f_0 (f_{01} = 1.49 THz, f_{02} = 0.96 THz and f_{03} = 0.547 THz) is considered as the isolated Fano resonance without being influenced by the neighboring resonators at the comparable large lattice periodicity. The simulated and the measured frequency shift are plotted in terms of varying periodicity for each set of the Fano resonator arrays shown in Figure 3-4 with the black, red and blue spheres indicating the 24, 33 and 60 μm resonator arrays, respectively. As the Fano resonators become smaller, the frequency oscillates in each resonance cycle is higher dictated by the absolute scaled down dimensions of the resonators. Accordingly, the frequency shift of the smaller resonator altered more distinctly when compared to the larger resonators. It is worth noting, in order to interact with the nearest neighbors at comparatively larger lattice constants, the magnetic flux for the bigger size resonator extended to larger space by showing a much longer decayed length than that in the smaller resonator arrays in Figure 3-4. To eliminate this size effect, we will discuss the size-scaling behavior in the next chapter. The frequency red-shift with increase in the lattice constant is due to weak mutual magnetic inductance coupling of the nearest neighbors since the Fano system exhibits magnetic nature without electric dipole excitation, in which only near-field coupling of the magnetic dipoles is considered. In 24 and 33 μm Fano resonator, the frequency shift shows a linear behavior while the frequency of the 60 μm Fano resonator shifts in the form of exponential decay.

In the sub-radiant system, we analyzed the collective coherent behavior mediated the energy loss in the system for all three differently sized Fano resonators. Linewidth with respect to the periodicities is extracted from the simulation result of the Fano resonance, as presented in Figure 3-5 with the linewidth 24, 33 and 60 μm indicated by black, red and blue spheres, respectively. We use the exponential decay
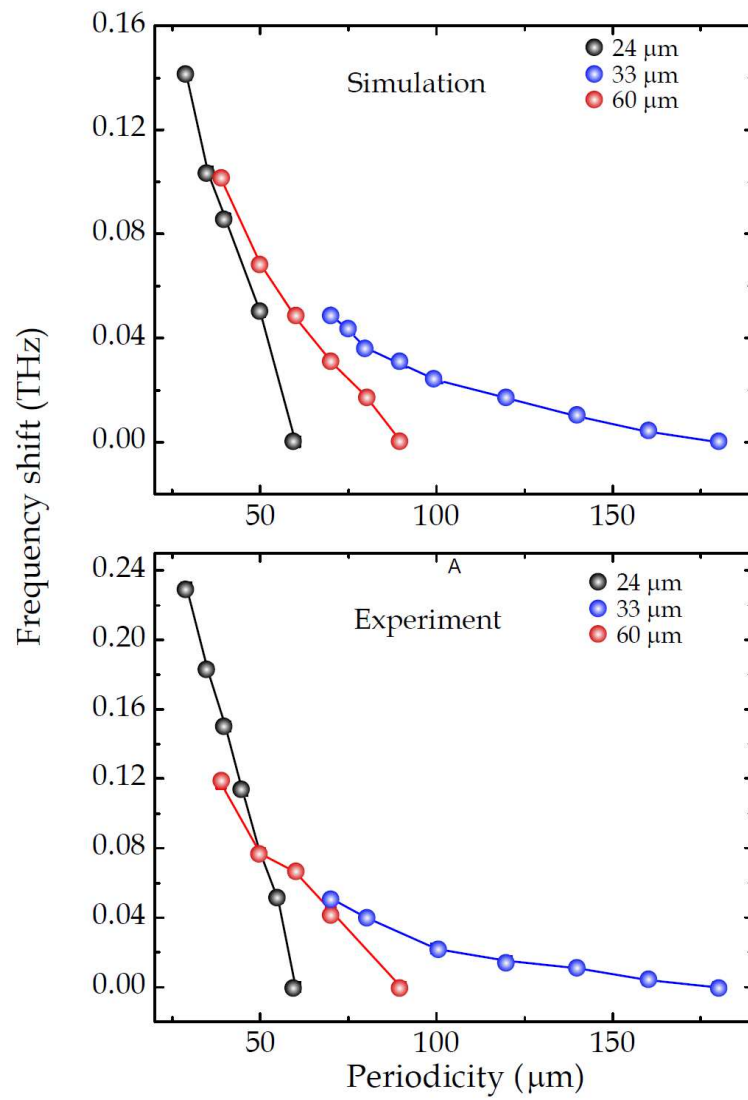
Figure 3-4. Frequency shift with respect to the periodicities (P). (a) and (b) The simulated and measured frequency shifts of the SRR arrays as a function of periodicities for 24 (black), 33 (red) and 60 μm (blue) Fano resonators.

curve $y = Ae^{-x/a} + y_0$ to fit the decay behavior of the linewidth for three sets of the Fano arrays, as shown in the solid curves in Figure 3-5. The R-square factor $R^2 = 0.99$ manifest a perfectly fitting to the exponential decay for all three linewidth varying of the Fano resonance. The fitted exponential decay rates are $t_1 = 8.7$ for 24 μm, $t_2 = 10.7$ for 33 μm and $t_3 = 19$. 60 μm sized Fano resonance with offset y_0 and the amplitude A are 0.03, 0.03, 0.01 THz and 2.4, 2.6 and 1.4, respectively for three size sets. The exponential decay rate of the linewidth raises with increase in the size of the Fano resonator since the larger resonator mediating the stronger magnetic flux radiates to broader areas than the smaller SRR arrays. The coupling strength of the external field to the Fano arrays is weaker in the 60 μm resonator by holding stronger surface currents than that in the 24 μm resonator. Consequently, the absolute dimension of the Fano resonator determines the strength of the induced magnetic flux in the system. The dissipation loss of the larger Fano resonator with higher Q factor radiation more efficiently in terms of larger decay length than that in the smaller Fano resonator.

3.5 Conclusion

In this chapter, we study the collective behavior of the near-field nearest neighbor coupling in the Fano resonator. The nearest-neighbor coupling of the Fano resonator dominates a frequency redshift with increase in the lattice constants for all three-differently sized Fano resonators due to weak magnetic inductance coupling between the neighbors. Then we find a size-dependent behavior of the exponential decay rate of the linewidth with the larger resonator corresponding to the bigger time decay rate. Next, we will continue to study on the size-scaling behaviors in the frequency shift and the linewidth varying trend.
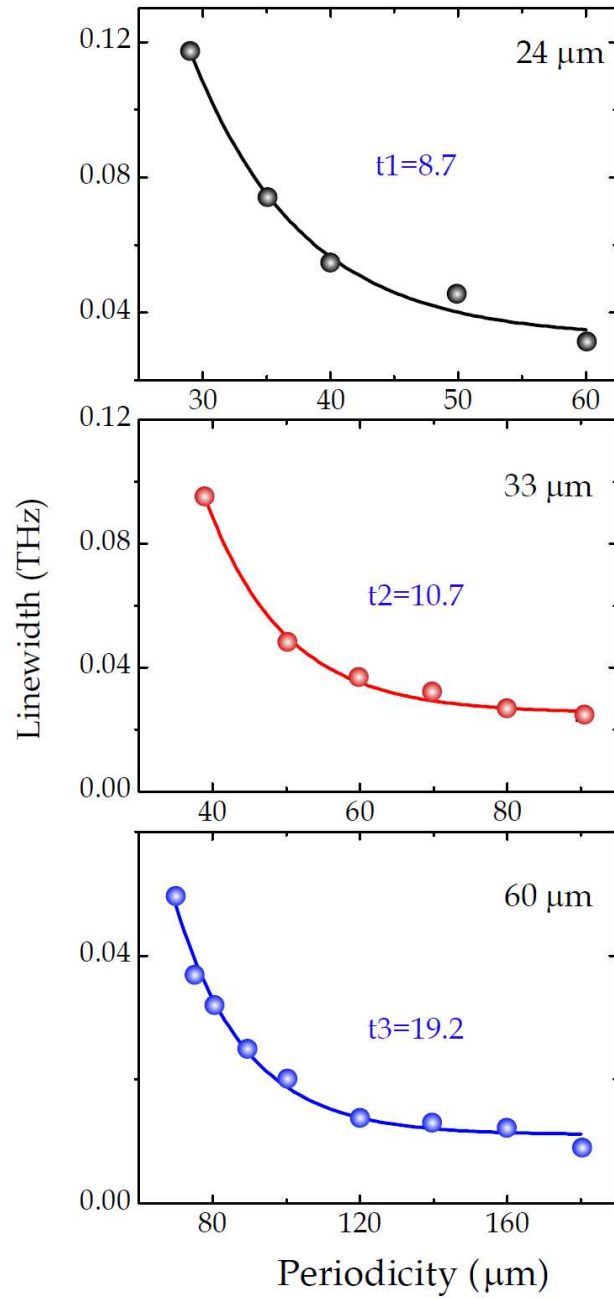
Figure 3-5. Linewidth with respect to the periodicities (P). (a), (b) and (c) are the extracted linewidth of the LC resonance as a function of periodicities from the simulation result and their exponential decay fitting curves $y = A\,e^{-x/t} + y_0$ for 24 (black), 33 (red) and 60 μm (blue) SRRs.

CHAPTER IV

UNIVERSAL BEHAVIOR IN METAMATERIALS: LORENTZ VERSUS FANO

4.1 Introduction and background

The collective coherent interactions in a meta-atom lattice is the key to functionalize the potential

applications in metasuface based photonics device. We demonstrate a collective coherent response

of the nearest neighbor coupled subwavelength resonators whose resonance shift decays in the

strong near-field coupled regime. This occurs due to the dominant magnetic coupling between the

nearest neighbors which leads to the decay of the electromagnetic near fields. In recent years, there

has been tremendous development in understanding the inter resonator near-field coupling between

dipolar resonator pairs in two-dimensional and three-dimensional plasmonic arrays that has also

resulted in excellent plasmonic rulers [30-36]. Plasmon rulers can predict the spectral shift of the

plasmon resonance based on the strength of the inter resonator near-field coupling. This unique

property allows plasmon rulers to determine extremely small angstrom scale distances in

biomolecules [32-34]. In most of the previous plasmonic coupling works, only the near-field

coupling between the metal particle pairs in the unit cell of a large array has been studied where

the coupling between different unit cells has been negligible [30-36,65-66]. There has been few

experiments and theoretical studies that directly probe the coherent collective behavior of nearest

neighbor coupled plasmonic resonators where all the resonators in the entire lattice are coupled to its nearest neighbor through their near fields [37-45]. The nearest neighbor coupling leads to a coherent behavior of the structured periodic lattice where the scattered near field of each resonator in the array determines the response of the plasmonic metamaterials. In this work, we selected two fundamental subwavelength resonator model on behalf of the symmetric and asymmetric resonant lineshapes: SRR and Fano resonator to study the collective coherence behavior of the nearest neighbor coupling in two dimension arrays. The collective scaling behavior of the coherent coupled metasurfaces are demonstrated in differently sized SRR with varying lattice constants. The spectral shift of inductive capacitive resonance show an exponential decay due to the nearest neighboring mutual inductance coupling, while in the Fano resonator, it can be modeled by the Lagrangian model. A coherent metasurface ruler (CMR) equation is identified in the form of the fractional frequency shift versus scaling periodicities, which manifest the coherent nearest metaatoms coupling strength. The CMR equation accurately predicts the near-field inductive coupling induced spectral shift in differently sized metasurfaces with varying lattice constant.

Furthermore, the dissipation loss engineered linewidth varying trend is studied in the SRR and Fano arrays. By applying the size scale, the decay of the linewidth is demonstrated to obey a perfect exponential decay with respect to scaling periodicities in both the SRR and Fano metasurfaces. The crucial finding is the different behavior in time decay rate, which persists with 0.32 in Fano arrays and is distinct in three different sized resonator arrays. We attribute this behavior to the distinguishable intrinsic resonant properties of the Fano and SRR modes.
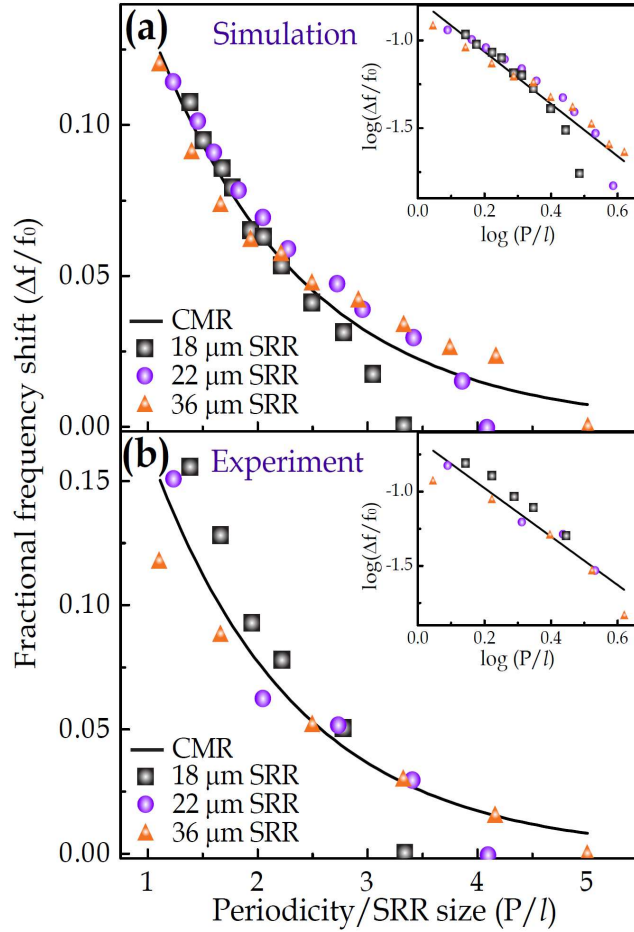
Figure 4-1. Fractional frequency shift versus scaling periodicities (a) Fractional frequency shift extracted from the simulated transmission amplitude versus scaling periodicities. The coherent metasurface ruler (CMR) equation is $\Delta f/f_0 \approx 0.28\exp\left[-(P/l)/1.38\right]$. (b) Fractional frequency shift extracted from the measured transmission amplitude versus scaling periodicities. The coherent metasurface rule (CMR) equation is $\Delta f/f_0 \approx 0.36\exp[-(P/l)/1.33)]$. The insets in (a) and (b) show the fractional frequency shift with scaling periodicities in logarithmic coordinates and corresponding linear fitting.

4.2 Coherent metasurface ruler

4.2.1 Mutual inductance model

We collected the data of three differently sized SRR sets of 18, 22 and 36 μm in side length, and the Fano sets of 24, 33 and 60 μm with asymmetry degree factor ~ 9%. The patterns are all fabricated on the 640 μm n-type Si wafer substrate with a resistivity of 12 Ohm·cm by conventional photolithography technique and followed by thermal deposition of 200 nm Aluminum film. The transmission data are collected by a photoconductive switch based 8f confocal THz-TDS and the simulated data were calculated from commercial CST microwave studio.

In order to explore the size scaling behavior, we defined fractional frequency shift as the ratio of the resonance blue shift and its intrinsic LC resonance: $\Delta f/f_0$ fractional LC resonance shift. The fractional frequency shift versus the ratio of period to the SRR size as P/l (l = side length of square SRRs) is plotted in Figures. 4-1(a) and 1(b). To our surprise, we notice that the overall fractional LC resonance shift versus P/l for all the differently sized SRRs with different periodicities show a collective behavior by obeying a single exponential decay equation $y = Ae^{-x/a}$, where $a = 1.38$ is the decay length extracted from simulated data plotted in Figure 4-1 (a). The corresponding value of the decay length from the measured data shown in Figure 4-2(b) is found to be $a = 1.33$. The insets of Figures 4-1(a) and 1(b) show the scaling behavior of fractional frequency shift with periodicity/size ratio on a log-log plot. The linear fit suggests that collective coherent behavior of SRRs obey the exponent law. The simulated and measured collective exponential decay lengths in all differently sized and different period coherent metasurfaces were found to be in good agreement. Thus, the collective coherent metasurface ruler (CMR) equation is formulated as:

$$\Delta f / f_0 = 0.28 \exp[-(P / l) / 1.38)] \tag{4-1}$$

The fractional LC resonance shift exponentially decays with increase in the lattice period to the SRR size ratio indicating that the near-field coupling among the nearest neighbor SRRs declines exponentially as the lattice size (P) increases with respect to the SRR size (l). This eventually becomes uncoupled when the P/l ratio exceeds five times (Figures 2-5(a) and 5(b)) since the fractional LC resonance blue shifting almost becomes negligible for $P/l > 5$. Largest fractional shift of the LC resonance is observed when the lattice size tends to approach the size of the SRRs. Intuitively, this behavior is obvious from the fact that the SRRs have the strongest near-field coupling when they become the closest to their nearest neighbors with strongest overlap of their magnetic flux created by the circular currents in the SRRs at the LC resonance frequency. Typically electric coupling causes red-shift of the LC resonance and the magnetic coupling causes the blue-shift. The dominant electric coupling phenomena is observed only in rectangular lattices [67]. However, in our present work, we do not observe any red-shifting of the LC resonance which is a signature of minimal electric coupling and the blue shift of the resonance is due to dominant magnetic coupling.

In order to understand the mechanism under the fractional frequency shift, we select a simple mutual inductance model due to high magnetic polarizability [68] at terahertz frequencies that describes the collective exponential decay of the fractional LC resonance shift with respect to the lattice period and the SRR size. The LC resonance frequency of a particularly sized SRR with varying periodicities depends on the change of the net inductance and the net capacitance of the LC circuit formed by the individual with an exponential function in order to compare with the CMR equation. For each SRR, there are four nearest neighbor SRRs that surround the individual SRR from its four side arms, as shown in the inset of Figure 4-2. However, only the nearest parallel SRR arms with the opposite currents have dominant mutual inductance effect on the frequency shift based on the near-field SRR. Based on the mutual inductance model, the LC resonance frequency
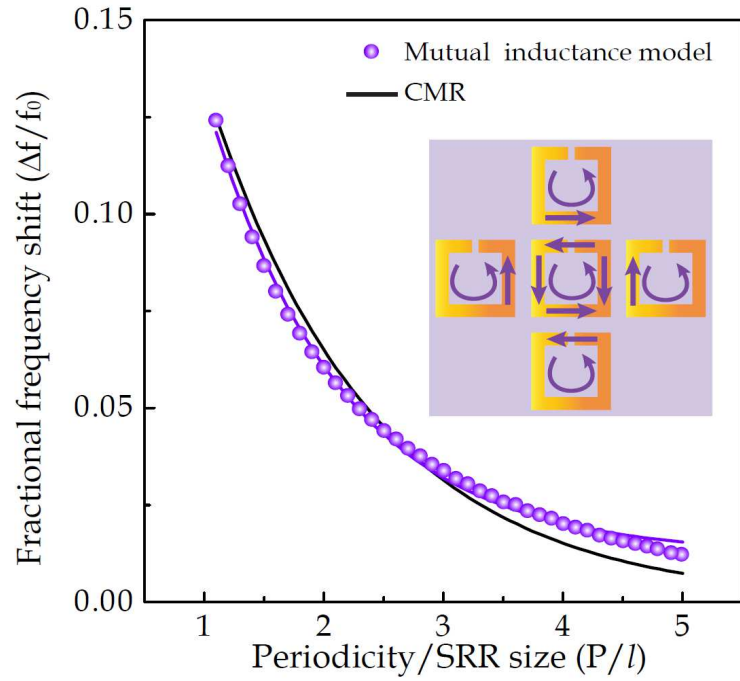
Figure 4-2. Comparison of CMR with mutual inductance model fitting. The exponential decay

fitting curves $y = A\ e^{-x/a}$, $a = 1.17$ calculated from the mutual inductance model and the coherent

metasurface ruler (CMR) equation $\Delta f/f_0 \approx 0.28\exp[-(P/l)/1.38)]$. The inset shows the surface

currents and mutual inductance of the four nearest neighbor SRRs surrounding the individual SRR.

is estimated and fitted by an exponential decay curve. Two parallel wires with the opposite current flows contributes to the net inductance of $L = Ls - M$, with Ls being the self-inductance of each SRR and M being the mutual inductance. The mutual inductance M is given in Equation (4-2) with l as the length of the conductors and d is the center-to-center distance between two wires [69.70].

$$M = \frac{\mu_0}{2\pi} l \left[\ln\left(\frac{l}{d} + \sqrt{1 + \frac{l^2}{d^2}} \right) - \sqrt{1 + \frac{d^2}{l^2}} + \frac{d}{l} \right] \tag{4-2}$$

For each specific size of SRRs with varying periodicities, the net capacitance and the self-inductance are constant while the mutual inductance varies with the change in the separation between the four neighboring SRRs. Then the modified LC resonance frequency becomes

$$f = 1/2\pi \sqrt{L_S - 4\frac{\mu_0}{2\pi} l \left[\ln\left(\frac{l}{P-l} + \sqrt{1 + \frac{l^2}{(P-l)^2}} \right) - \sqrt{1 + \frac{(P-l)_2}{l^2}} + \frac{(P-l)}{l} \right] C} \tag{4-3}$$

Here the frequency f can be plotted as a function of P/l. For the 36 μm SRR the frequency shift can be scaled and plotted shown by spheres in Figure 4-2 with the exponential fitting decay length of $a = 1.17$. Compared to the CMR equation with exponential decay length of $a = 1.38$ indicated by solid curve, the fractional LC resonance frequency shift calculated from a simplistic mutual inductance model is reasonably close to the experimental and simulated decay lengths. The difference in the value comes from the limitation of the model which is based only on individual SRR surrounded by four nearest neighbor SRRs whereas in the measurements and simulations, the response comes from the entire metasurface lattice.

4.2.1 Eulerian-Lagrangian Model

The Eulerian-Lagrangian expression was generally applied in the classical fluid filed mechanic to describe the fluid motion with respect to the space and time. Here based on the Eulerian-Labrangian model, we are able to evaluate it in the form of the charges and calculate the fraction frequency shift in the differently sized Fano resonators with scaling periodicities. The lagrangian equation in the system can be expressed as [65-67]:

$$\Im = T - V \tag{4-4}$$

Here T is the kinetic energy and V is the potential energy. In the Fano resonator, with the electric field polarized perpendicular to the gap of the ASRR, the surface currents conserved in the two arms oscillate out-of-phase. We present the net charges on each individual Fano resonator location by Q_i, since the charges in the top and bottom gaps are with the opposite signs. Served as a sub-radiative system, the minimum resistor loss render that the frequency of the Fano resonator can be simply modeled as $\omega = 1 / \sqrt{LC}$, L and C are equivalent inductance and capacitance. Then the kinetic energy and the potential energy can be rewritten as:

$$T = \frac{L}{2} \dot{Q}_i^2, \quad V = \frac{1}{2C} \dot{Q}_i^2 \tag{4-5}$$

For an individual Fano resonator, with the net change Q_i in location defined as the Lagrangian coordinate, the Lagrangian can be expressed as:

$$\Im = \frac{L}{2} \dot{Q}_i^2 - \frac{1}{2C} \dot{Q}_i^2 \tag{4-6}$$

For the Fano resonance, with the assymetric mode induced surface current only in the arms, we consider the contribution of the near-field nearest neighbor coupling is solely from the magnetic

37

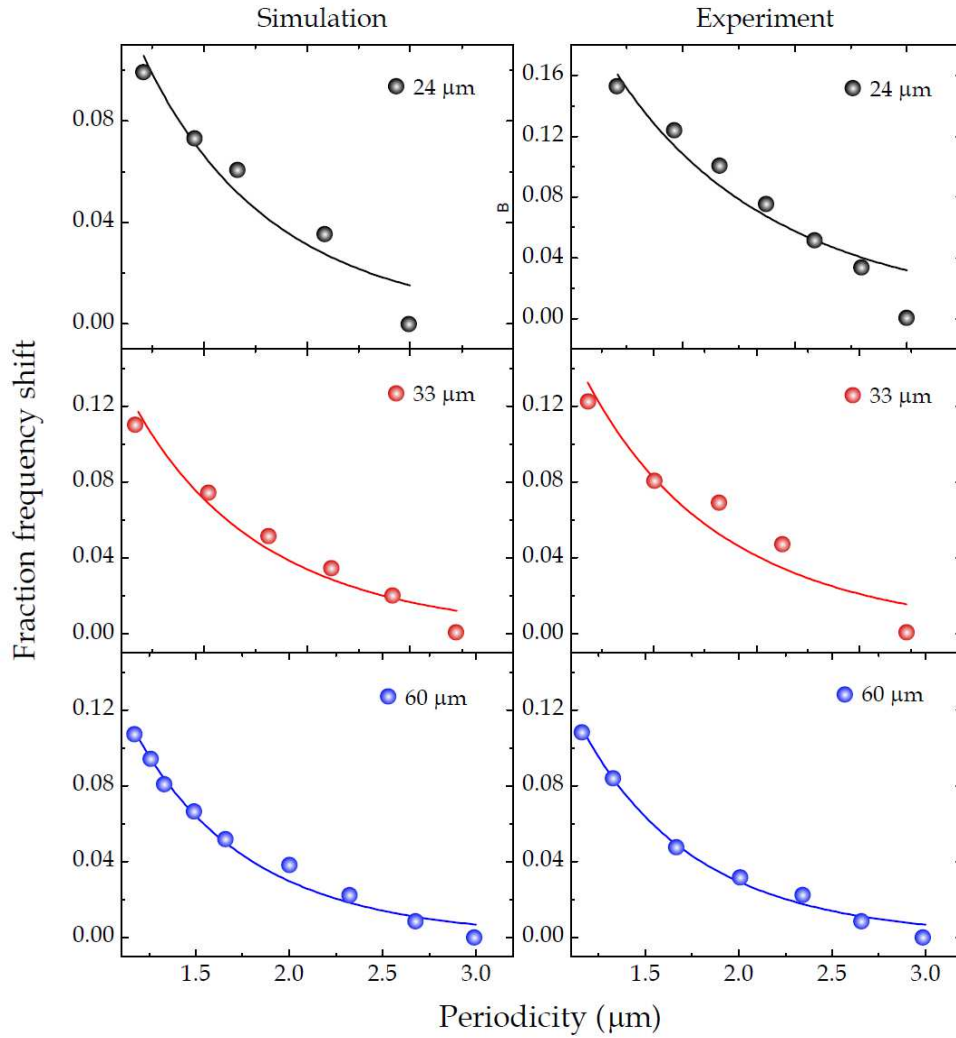**Figure 4-3**. Fractional frequency shift versus scaling periodicities. Fractional frequency shift extracted from the simulated and measured transmission amplitude versus scaling periodicities. The coherent metasurface ruler (CMR) is indicated by the solid curves in each figure. The fractional frequency shift for the 24, 33 and 60 μm Fano resonator are indicated by the black, red and blue spheres, respectively.

dipole coupling. In our Fano metasurface samples, the resonators are arranged in the square lattice constant scheme. The influence of the near-filed coupled magnetic dipoles are equal in the x and y directions. Then the lagrangian in the four-nearest neighbor coupled Fano resonator scheme can be expressed as:

$$\Im = (\frac{L}{2}\dot{Q}_1^2 - \frac{1}{2C}\dot{Q}_1^2) + 4(\frac{L}{2}\dot{Q}_2^2 - \frac{1}{2C}\dot{Q}_2^2) + 4M_H\dot{Q}_1^2\dot{Q}_2^2(\frac{1}{P^3}) \qquad (4\text{-}7)$$

where, p is the periodicity of the Fano arrays and M_H is the mutual magnetic inductance. Q_1 is the net charges of the individual center Fano resonator, while Q_2 represents the net charges in the nearest neighbor coupled resonators persisted with the equal near-field coupling effect. In our near-field system, in chapter II and III the exponential decay of the linewidth manifests the resonant dissipation loss decay in the form of exponential with respect to lattice constants or separations between the two nearest neighbor resonators. It allows us to model the near-field coupled magnetic field to behave as the evanescent wave similar to the surface wave, so the decayed magnetic field versus the interaction between the magnetic inductance is rewritten as $\sim \exp(-P/t)$ with t denoting the exponential decay rate of the magnetic flux. Finally we have Lagrangian as:

$$\Im = (\frac{L}{2}\dot{Q}_1^2 - \frac{1}{2C}\dot{Q}_1^2) + 4(\frac{L}{2}\dot{Q}_2^2 - \frac{1}{2C}\dot{Q}_2^2) + 4M_H\dot{Q}_1^2\dot{Q}_2^2 \exp(-\frac{P}{t}) \qquad (4\text{-}8)$$

After substituting the Lagrangian (4-7) into the following pair of the Eulerian-Lagrange equations (4-8) and (4-9):

$$\frac{d}{dt}(\frac{\partial\Im}{\partial\dot{Q}_1}) - (\frac{\partial\Im}{\partial\dot{Q}_1}) = 0 \qquad (4\text{-}9)$$

$$\frac{d}{dt}(\frac{\partial\Im}{\partial\dot{Q}_2}) - (\frac{\partial\Im}{\partial\dot{Q}_2}) = 0 \qquad (4\text{-}10)$$

The two eigen frequencies representing the symmetric and asymmetric modes of the Fano arrays are solved as:

$$\frac{\omega_{\pm}}{\omega_0} = \sqrt{\frac{1}{1 \mp 4(M_H / L)\exp(-P/t)}}$$

(4-11)

In our Fano resonator arrays, the anti-parallel surface currents endow the magnetic dipoles transversely couple in phase, and we choose ω_+ as the eigen frequency in our system. Then the fractional frequency shift can be expressed as:

$$\frac{\Delta f}{f_0} = \sqrt{\frac{1}{1 - 4k_H \exp(-P/t)}} - 1$$

(4-12)

Here $k_H = M_H/L$ represent the magnetic inductance coupling coefficients. To explore the size scaling behavior, we defined fractional frequency shift as the ratio of the resonance blue shift and its Fano resonance at largest periodicities $\Delta f/f_0$, where f_0 is also considered as the individual Fano resonance without coupling to the neighbors. Figure 4-3 shows the fractional frequency shift from the simulation (left column) and the measurement (right column) with respect to the scaling periodicities, defined as the ratio of period to the Fano resonator size as P/l.

It is crucial to notice that the fractional Fano resonance shift for all the different sized Fano resonators with scaling lattice periodicities show a collective universal behavior by obeying the same fraction frequency shift curve with similar field decay rate, which is calculated based on the size scaling lagrangian model:

$$\frac{\Delta f}{f_0} = \sqrt{\frac{1}{1 - 4k_H \exp(-\frac{P}{l}/t)}} - 1$$

(4-13)

The magnetic coupling coefficient $k_H = 0.25$ is obtained by the fractional frequency curve fitting. The corresponding decay rate of the evanescent magnetic field extracted from the simulation results are 0.71, 0.73 and 0.70 for 24, 33 and 60 μm Fano resonators. It significantly predicted a size scaling behavior of fractional frequency shift with periodicity/size ratio of the Fano resonance dictated by obeying one coherent metasurface ruler equation. The exponential decay rate of the magnetic extracted from the measurement are 0.89, 0.78 and 0.69 for 24, 33 and 60 μm Fano resonators. The experimental result shows the reasonable consistency with the simulated result, as shown in Figure 4-3.

To probe the size-independent behavior, the overall fractional frequency shifts $\Delta f / f_0$ extracted from the simulation and measurement are illustrated in Figure 4-4. The overall simulated fractional shift of the Fano resonance versus P/l for all the different sized Fano resonator with different periodicities show a collective behavior by obeying a single coherent metasurface ruler expression in equation (4-13), with $t = 0.71$ extracted from the curve fitting,

$$\frac{\Delta f}{f_0} = \sqrt{\frac{1}{1 - \exp(-\frac{P}{l}/0.71)} - 1} \qquad (4\text{-}14)$$

In the measurement, the corresponding magnetic inductance coupling coefficient is $t = 0.79$, which is very close to the simulated value. The experiment result is reasonably consistent with the simulated result. The little discrepancy of the fractional frequency shift of the smaller Fano resonator in the measurement are mainly due to the measurement restrictions, where the excitation area of the metasurface arrays in measurement is fixed as $\pi(3.5/2)^2$ mm^2. It leads to much more numbers of the meta-atoms stimulated in the 24 μm than that in the 60 μm Fano arrays, which result in a frequency blue-shift [48]. However, in the simulation, this effect is neglected by setting the infinite unit cell boundaries.

41
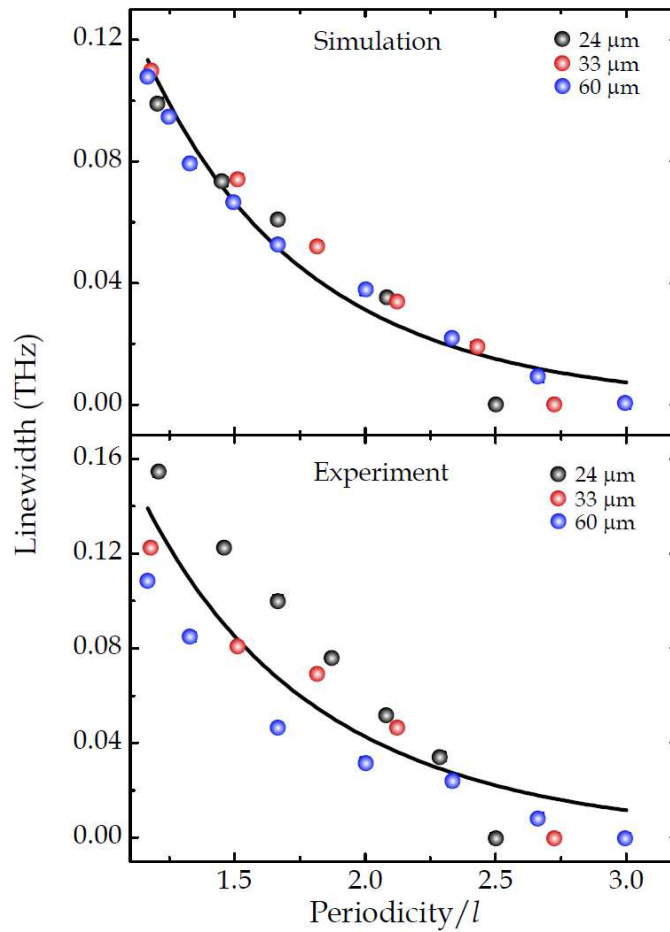
Figure 4-4. Overall fractional frequency shift versus scaling periodicities (a) Fractional frequency shift extracted from the simulated transmission amplitude versus scaling periodicities. The coherent metasurface ruler (CMR) equation is $\Delta f/f_0 \approx (1/(1-\exp(-(P/l)/0.71)))^{0.5}-1$. (b) Fractional frequency shift extracted from the measured transmission amplitude versus scaling periodicities. The coherent metasurface rule (CMR) equation is $\Delta f/f_0 \approx (1/(1-\exp(-(P/l)/0.79)))^{0.5}-1$.

4.3 Universal and distinct behavior in radiation loss properties

In order to understand the universal behavior in radiation loss properties, we analyze the size scaling behavior by plotting the linewidth of the Fano resonance versus scaling periodicities (P/l) of the Fano resonance, as shown in the top row in Figure 4-5. The linewidth is decreasing as the Fano resonator has a denser packing, where the strong coupling between the Fano resonators contribute to the numerous degenerate levels. When the separation of the resonators expanded, the individual Fano resonator will only offer one discrete energy level with minimum radiation loss of the system. The linewidth of the Fano resonance obeys the exponential decay for all three differently sized Fano resonators with the equation formatted as $L = \mathrm{Aexp}(-(P/l)/t)+y_0$. To our surprise, the exponential decay rate of the linewidth versus the scaling periodicities (P/l) remain almost constant by obtaining the similar time decay rate of 0.36 0.32 and 0.32 for 24, 30 and 60 μm Fano resonators, respectively. This size scaling universal behavior signified that the near-filed nearest neighboring coupling mediated collective energy dissipation loss of the differently sized Fano resonators decay at a fixed rate.

To probe the nature of the linewidth varying trend, we compare the linewidth varying between the LC and Fano resonators. Figure 4-5 bottom row shows the linewidth size scaling behavior of the LC resonator, by fitting the exponential decay curve in terms of the scaling periodicities, the decay lengths are 0.75, 0.66 and 0.45 for the 18, 22 and 36 μm Fano resonator. The decay rate of the linewidth in the LC resonance is decreased with increasing size of the SRR. In other words, the energy dissipation loss vanishes more rapidly in larger individual Lorentzian resonator than it in the smaller resonator. In the SRR resonator arrays, the Q factor is enhanced with the increase in the SRR size, where the surface currents are trapped more tightly in larger SRRs. Consequently, the

higher Q factor of the LC resonance contributes to an energy radiation process to external free space in a more efficiently way than that in the low Q factor case dictated by more radiation loss.
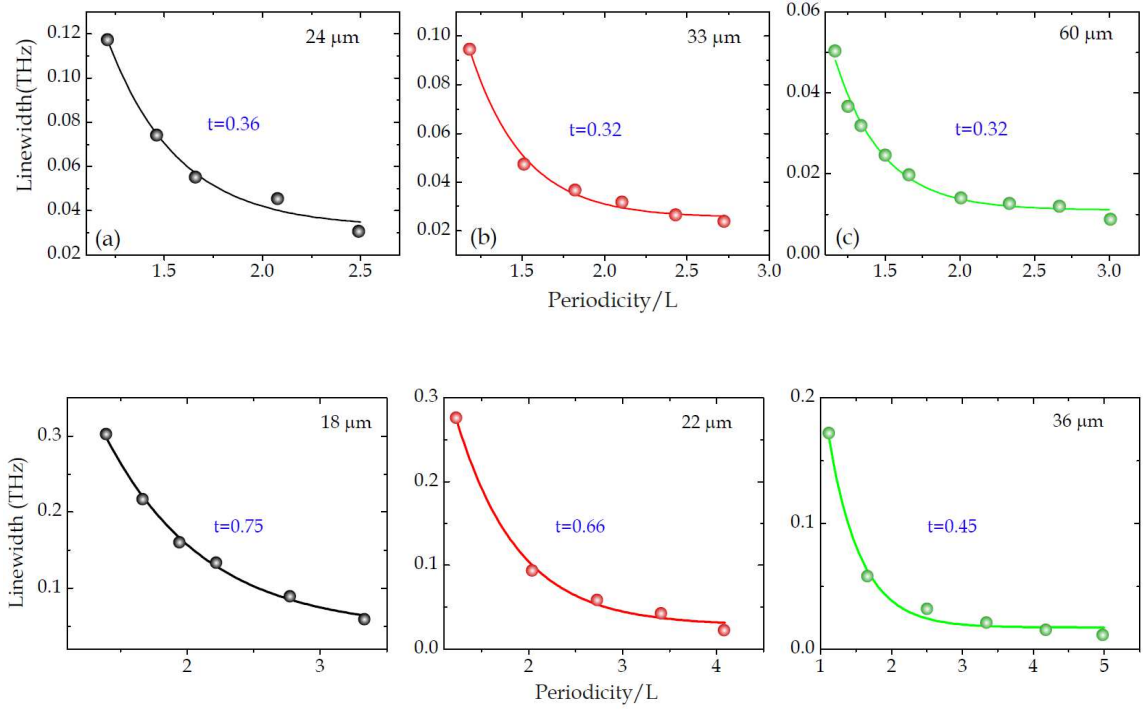
Figure 4-5. Comparison of linewidth decay between the LC and Fano resonance versus the scaling periodicities. Top row represents the linewidth of the Fano resonance versus the scaling periodicities for three differently sized resonators 24 (black), 33(red) and 60 (green) μm and the corresponding exponential decay fitting $y = Ae^{-x/t}+y_0$ is presented in solid curves. Bottom row shows the linewidth varying trend for three sets of SRR, with black, red and green spheres indicating 18, 22 and 36 μm SRRs. The exponential decay fitting is presented in solid curves in each Fano arrays.

4.4 Comparison of the Fano and SRR system

To understand the different dissipation loss feature of the LC and Fano resonance, we examine the resonant mode nature of the SRR and Fano resonators. The schematic surface currents and induced electric and magnetic dipoles are shown in Figure 4-6(a) and 6(b). To excite the LC resonance, with the electric field parallel to the gap of the SRR, a circular surface current as an analogue of a LC circuit with the maganetic dipole perpendicular to the metasurface plane is induced. In the near-field coupling map of the SRR arrays, the magnetic dipoles are transversely coupled in the plane while the electric dipoles are coupled both transversely and longitudinally [66,67]. The intricate coupling behavior of the electric and magnetic dipoles leads to a size-dependent behavior of the energey disspation loss with respect to the scaling periodicities. On the contrary, the Fano resonance is excited by the electric polarized field perpendicular to the two gaps. The surface currents located on the left and right arms oscillate out-of-phase, which forms a magnetic dipole conserved in ASRR. In contrast, the electric feature is degraded by the destructive interference of the surface currents. With the weak net surface currents conserved in the Fano arrays, the electric dipoles and their interactions are neglected. In the Fano resonance system, we consider the collective coherent coupling only exists in the magnetic dipole coupling.

 As the electric surface currents are anti-parallel aligned in the arrays, the nearest neighboring interactions cause the surface currents to cancel by each other. After the cancellation effect of the surface currents, the Fano resonator arrays is simplified to an configuration with only left and right arms survived at the edge of the array, as shown in Figure 4-7[16]. This is also the reason why the Fano arrays behave as a sub-radiate system, in which there are very rare electric or magnetic dipole that can couple to the external light field or radiate to the free space. It leads to a size-independent

behavior in the energy dissipation loss in three-differently sized Fano resonator arrays. Thus, the

exponential decay rate of the three sized resonator arrays are keeping almost constant at 0.32.
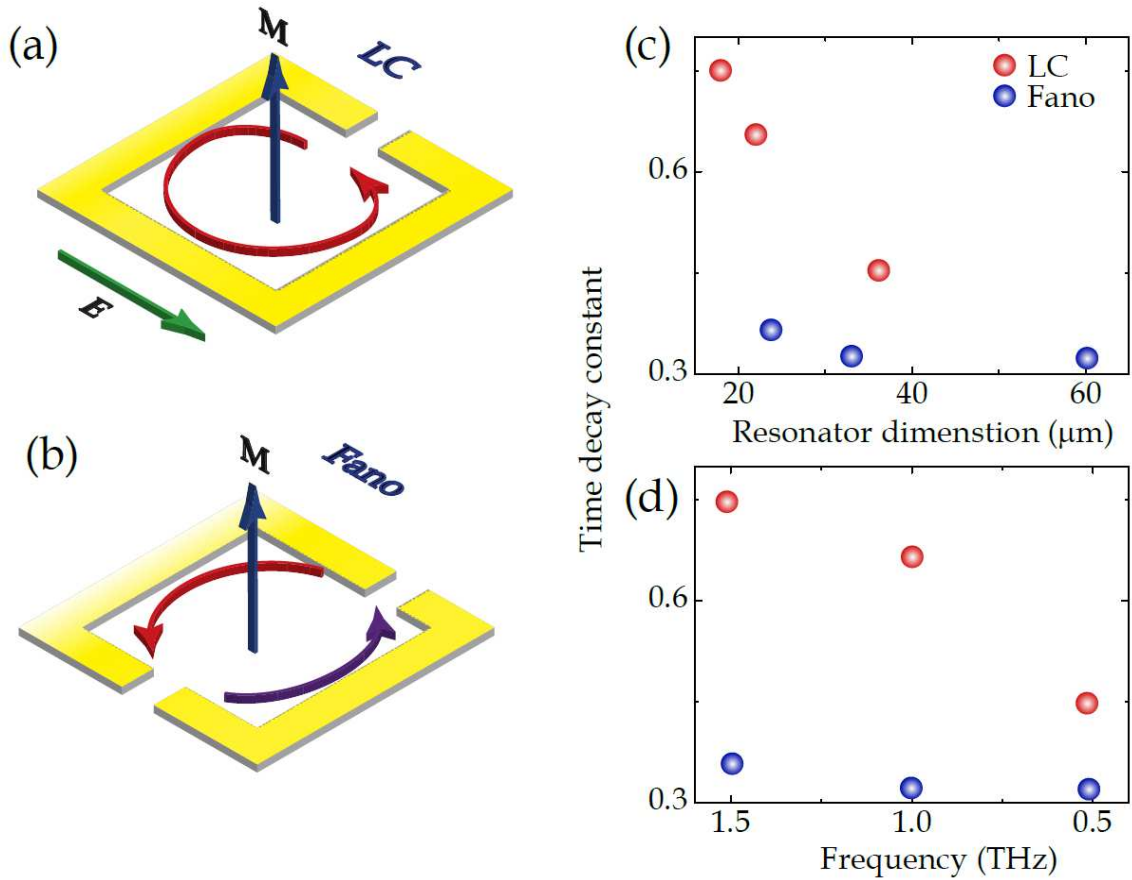
Figure 4-6. Comparison of time decay rate of the LC and Fano resonance. (a) and (b) show

schematic surface currents and corresponding induced electric and magnetic dipoles. (c) Time

decay rate with respect to resonator dimension. (d) Time decay rate versus the central frequency.

Red and blue spheres indicate the LC and Fano systems, respectively.

The different mode nature of the LC and Fano resonance rendered the LC system behave as a radiative system while the Fano system served as non-radiative system. The time decay rate of the LC and Fano resonance are plotted versus the dimension of the resonator and the rough center resonance frequency in Figure 4-6(c) and 6(d). The time decay rate is decreasing with increase in the dimension of the SRR and also the resonance frequency. In the Fano systems, the time decay rate holding a constant due to sub-radiate feature in the system.
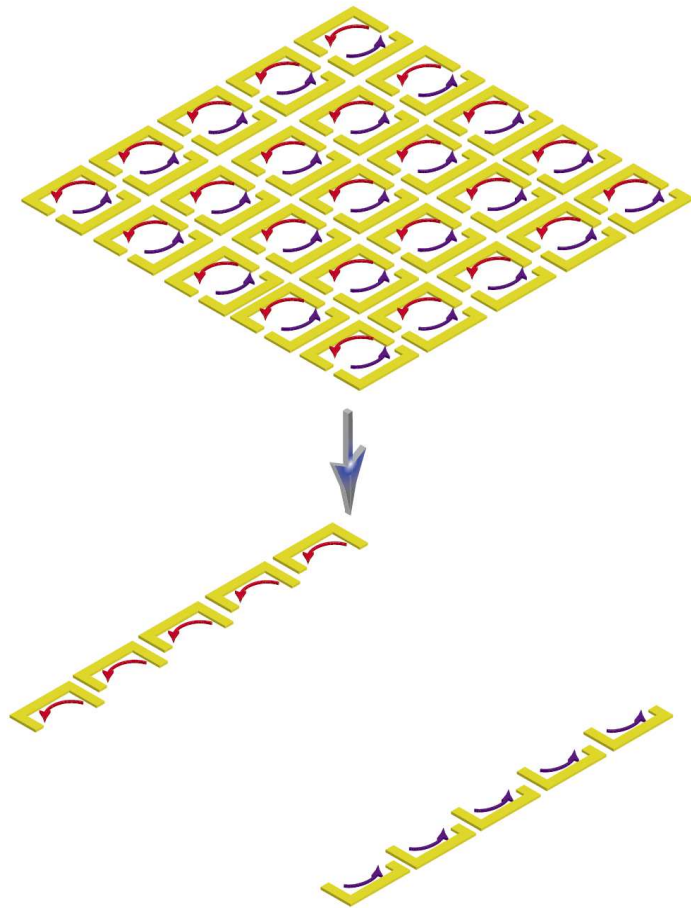
Figure 4-7. Schematic surface currents cancellation behavior in Fano resonator metasurface [16].

4.5 Conclusion

In summary, we demonstrated the universal behavior in two fundamental modes Lorentzian mode and the Fano mode. Collective coherent metasurface ruler equation can predict the lattice size or the distance between the two nearest meta-atoms by observing the fractional resonance shift in the transmission spectra of the SRR and the Fano resonator metasurface array. By applied mutual inductance in LC resonance and Lagrangian model in the Fano system, we identified a CMR equation ruler for each mode. The SRR arrays are considered as a radiative system while the Fano arrays persist a non-radiative feature. The linewidth in terms of the scaling periodicities associated with the energy dissipation loss are discussed in SRR and Fano resonators. Although the trend of the linewidth all decay in form of perfect exponential, the decay rate exhibits distinct behavior in SRR and the Fano resonance. The time decay constant keeps constant in all three differently sized Fano arrays while the time decay constant in the SRR system varies. We attribute this behavior to the different mode nature of the LC and Fano resonance by analyzing the surface currents and the dipoles coupling behaviors. The identification of the CMR equation opens up avenues to design metasurface resonance based rulers that could be used to measure distances in dynamic material/biological systems. Identification of the collective coherence in metasurfaces across the broad electromagnetic domain would allow efficient design of flat metasurface based lasers and optics, such as lasing spasers, flat lenses, and ultrasensitive planar sensors.

CHAPTER V

FAR-FIELD COUPLING VIA LATTICE MODE MATCHING IN METAMATERIALS

5.1 Introduction and background

One century ago in 1902, Woods discovered that a sharpness of the bright and dark patterns shown in reflection spectrum of a metal grating at certain incidence angle, later referred to Wood's anomaly [71,72]. Based on this idea, similar phenomena were observed in other systems such as the propagation of surface plasmons [73-74]. The scattered wave vector matched the periodicities of the grating or other periodic structures through the modulation of the incidence angle. Thus, the energy and shape of the scattered light radiation can be tailored through varying angles. Motivated by the capability of the lineshape modulation of the light, we study on the diffraction mode management in metamaterials. Extreme low radiation loss feature is pursued in order to improve the design for potential metadevices due to radiation loss, which is degrading the performance of the device. However, there are challenges encountered, such as non-radiation loss in terms of the metal loss, radiation loss in terms of the mode nature and dimensions of the resonator design. All these factors lead to a restriction on enhancement of the Q factor. Without altering the mode nature, the Q factor is hard to enhance dramatically by adjusting the material and dimensions of the subwavelength resonators.

Based on the wood's anomaly, Walther, *et al* reported in 2009 that they obtained the high Q factor in periodic metamaterials by coupling the structures radiative behavior. It was demonstrated that the odd mode resonant lineshape of the LC resonator can be narrowed by tuning the lattice periodicities [75-76]. However, in their finding they claimed that the even eigen mode of the LC resonator was forbidden since the electric potential stimulated by the external field is not symmetric. In our work, we demonstrated that the Q factor of the even mode of the LC resonator can also be tailored by managing the diffraction mode match in simulation and experiment. We conclude that one of the most efficient way to increase the Q factor is the diffraction mode management, which can depress the radiation loss and increase the Q factor of the resonance dramatically. The diffraction management is demonstrated to be of a universal applicability to metasurfaces, which is suitable to various resonant modes and different resonator dimensions. The diffraction mode highly depresses the radiation loss of the LC (n = 1), Dipole (n = 2) and Quadrupole (n = 3) modes. An of order magnitude increase in Q factor is achieved by tuning the far-field diffraction through engineering the periodicities. Such precise tailoring and control of the resonances in a metasurface lattice could have potential applications in loss engineering, sensing, and design of high-Q metamaterial cavities.
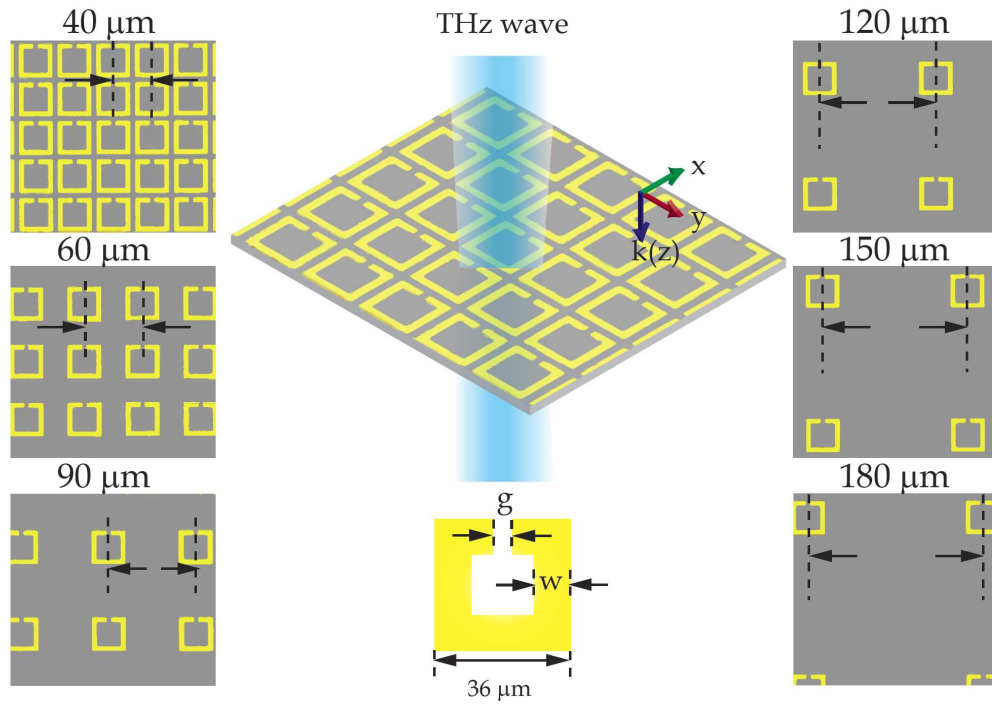
Figure 5-1 Microscopic image of metasurace samples. The dimensions of the square SRR is 36 μm, $w = 6$ μm and $g = 3$ μm. For the fixed size resonator, the lattice constant is varying between 40 - 180 μm as shown in the insets.

5.2 Sample preparation and characterization

In order to manage the far-field diffraction radiation, the SRR are chose as the common resonator, as shown in Figure 5-1. The size of the square SRR is 36 µm with width $w = 6$ µm and gap $g = 3$ µm. A set of 36 µm SRRs with lattice constants: 40, 60, 90, 120, 150, and 180 µm were fabricated, as shown in the microscopic images in Figure 5-1 insets. The metasurface samples fabricated on a n-type 640 µm silicon substrate by conventional photolithogphy technique. The 200 nm thick Aluminium film was thermally deposited after developing the patterned photoresist layer. In order to study the effect solely from the diffaction, a set of 36 µm SRR with lattice constant ranging from 40 to 180 µm are mesured by *8f* confocal terahertz TDS as described in Chapter II. With the terahertz beam normally incident on the metasurface sample, the transmission of the electrical field polarized parallel and perpendicular to the gap (*x* and *y* in figure 1) are measured for the purpose of multi-mode excitation.
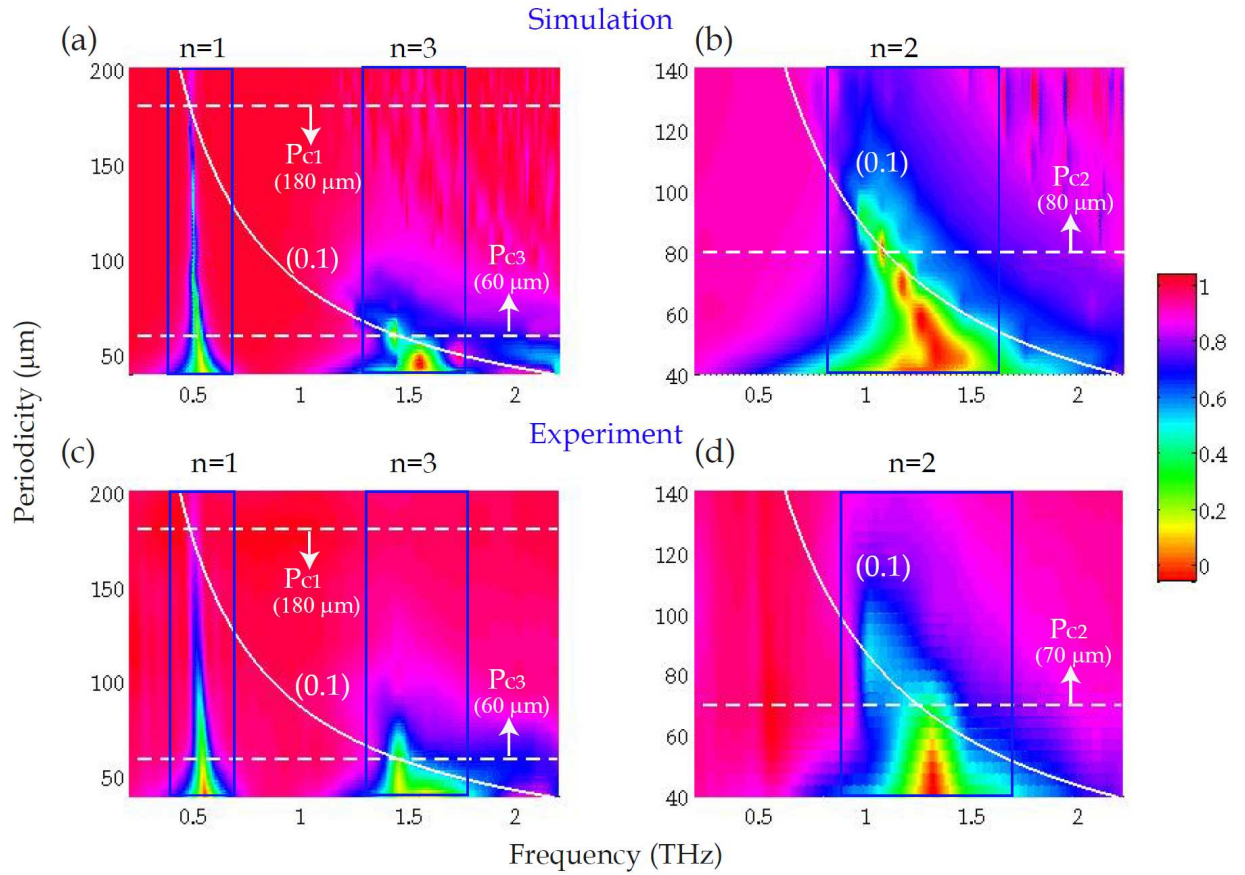
Figure 5-2 Simulated and measured transmission modes map. (a) and (c) Simulated and measured transmission for the LC (n = 1) and Quadrupole modes (n = 3) when square periodicity is varying from 40 to 200 μm. (b) and (d) Transmission map for Dipole mode (n = 2) with the periodicity changing from 40 to 140 μm. The solid curves represent the first diffraction mode (0, 1) for three modes, while the critical peirodicity Pc_1, Pc_2 and Pc_3 are indicated by the dashed lines.

5.3 Transmitted dispersion map

With the electric field parrallel to the gap of SRR (y direction), the odd modes n = 1 and n = 3 are excited, as indicated in figure 5-2(a), the simulated transmission mode map. The colors indicate the transmission amplitude strengh (see the scale bar), with the x axis denoting the frequency and the y axis presenting the periodicity variation. At 0.5 THz, the loretzaion mode (n = 1) is becoming more narrower with an increase in the periodicity. The same behavior was also observed in the quadrupole mode around 1.5 THz. The modes are significantly compressed in large and small periodicity range for n = 1 and n = 3 respectively. To illustrate this diffraction management behavior, the diffraction order related to the matching frequency in the square SRR arrays can be expressed as [75,77]:

$$f^2 = (\frac{c}{n_s P})^2 \times (i^2 + j^2) \tag{5-1}$$

where P and f are the periocidity and frequency, n_s is the refractive index of the substrate and c denotes the speed of light in vaccum. The intergers pair (i,j) specifies the order of the diffraction mode. In our mode management, we only consider the first diffraction mode since it is the most significant mode, and it can be simplified to

$$f = \frac{c}{n_s P} \tag{5-2}$$

The coresponding first diffraction mode description is indicated by the solid curves in Figure 5-2. The first fundamental diffration mode curve and each resonanant mode intersects at the critical periodicity. P_{c1} = 180 μm and P_{c3} = 60 μm denoting the critical periodicity for n =1 and n =3 correspondingly, are indicated by the dashed line in figure 5-2(a). The higher resonant frequency of the qudrupole mode shrinks the critical periodicity compared to the lorentzain mode excited at low frquency. The even mode n =2 with the dipole nature are excited with the electrical field

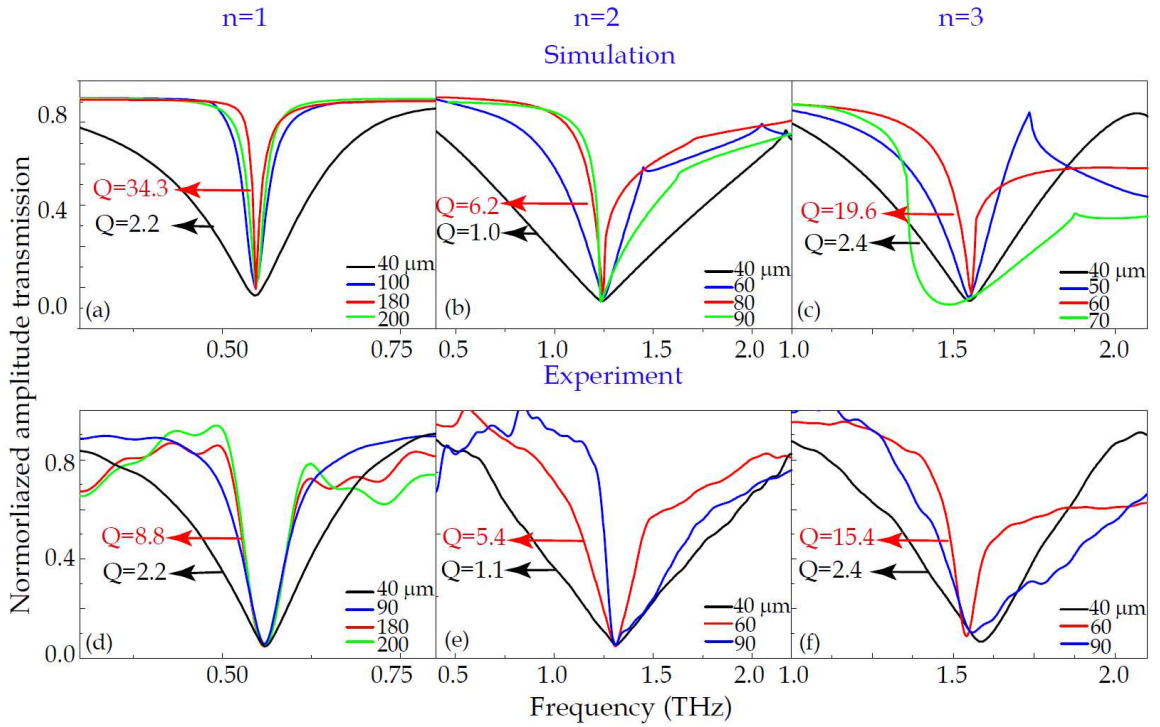**Figure 5-3** Normalized simulated and measured transmission spectra. Simulated (a)-(c) and measured (d)-(f) spectra which are normalized to keep the transmission minimum coincident on one point. The selected sample sets with varying periodicities for n = 1, n = 2 and n = 3 are shown. The comparison between the maximum and minimum *Q* factors of the diffractive mode and non-diffractive mode are labeled on the figure.

polarized towards the *x* direction, as shown in Figure 5-2(b) and 2(d) for the simluation and measured results. We also found that the mode is extremely broad at 40 µm, and becomes the narrowest when the lattice constant reaches the critical periodicity 80 µm. All three modes follow the same trend of the mode change. It shows the broadest feature in the small perioidicity and becomes narrow down with the increase in the periodiciity, then suddenly shrink to the narrowest at the critical periodicity point, and later the mode envolves to broad again and vanishes finally. By simply varying the periodicities, the diffraction coupling of the metamolecule array distinguishly manages all three differenty types of the resonant mode from the broad to narrow shape. During the mode compressing process by engineering the diffraction mode matching, we also observed a red shift due to mutual inductance coupling disscussed in chapter II. The measured transmission maps shown in Figure 5-2(c) and 2(d) are consistent with the simulation result, except that the Lorentzian mode in the measurement is wider than the simulation due to the limitation of the resoluation in normal THz-TDS measurement.

5.4 Data Analysis

Figure 5-3(a), 3(b) and 3(c) show the calculated normalized transmission amplitudes of the lorentzain, dipole and quadrupole modes. The transmission minimum of the SRR arrays with varying periocidities are normalized to be coincident at one center in order to clearly present the management of the linewidth. At LC mode, it is essential to notice at diffraction mode matching periodicities, the *Q* factor is 15 times higher compared to that in the broadest mode at 40 µm periodicity. When the peiodicity is increasing to 200 µm, the diffraction mode mismatch broadened the mode back. Normally, without transformation of the mode nature it is almost impossible to enhance the *Q* factor is to one order of magnitude range only by adjusting the geometrical parameters of the resonator. The diffraction mode match here achieves the most simpliest way to
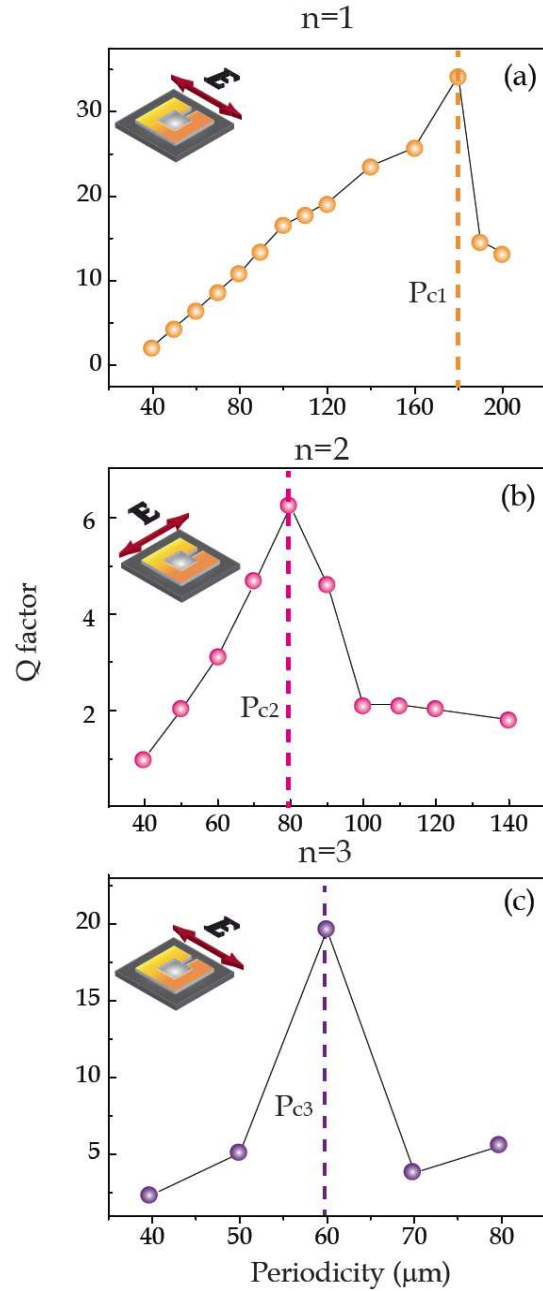
Figure 5-4 Simulated *Q* factors of LC, Quadrupole and Dipole modes. (a), (b) and c) are extracted *Q* factors of Lorentzian (n = 1), Quadrupole (n = 2) and dipole modes (n = 3) with varying periodicities 40 to 200 μm, 40 to 140 μm and 40 to 80 μm . The critical periodicities are indicated by the dashed lines for each mode.

largely modulate the Q factor of the resonance. Even for the high radition loss nature of dipole (n = 2) and quadrupole (n = 3), the Q factor are also efficiently increased from 1.0 to 6.2 and 2.4 to 19.6, respectively. Figure 5-3(d), 3(e) and 3(f) present the measured lineshape of the each mode. The ultra-narrow linewidth of the lorentzian mode at diffraction mode is limited by the resolution 57 GHz of the measurement. The extracted Q factor from the measurement of the other two modes agree very well with the simulated value.

To explore the evolution of linewidth varying by engineering the lattice mode, the simulated Q factors with periodicites are plotted in the Figure 5-4(a), 4(b) and 4(c). It is worth noting that the Q factor increases when the periodicity increases to close to the critical periodicities and degrade due to the further larger descrepency of the diffration mode mismatch. At n = 1 mode, the Q factor is 2.2 at 40 μm and gradually increases to 25 at 160 μm, then burst to 33 at the critical peirodicity 180 μm. With the further increase of the periodicity, the diffration mode mismatch leads to the abrupt drop of the Q factor of 15. The same evolutions are observed in n = 2 and 3 modes, Q = 6.2 and 19.6 are achieved at the critical periodicity at 60 and 80 um accordingly. When the lattice constant is closely approching or leaving the diffration mode matching, there is a sudden enhancement or reduction in the Q factors. Although the larger periodicities associated with the longer seperations between the indivudal resonator can gradually decrease the damping loss by isolating the neighboring metamolecule from hybridazaoin state to a tightly-bonding state [64], it can only gradually narrow down the lineshape of the reonance instead of changing the Q factor of the resonance dramatically. Then we proved that the sudden jump of the Q factor is only attributed to the diffraction mode matching.
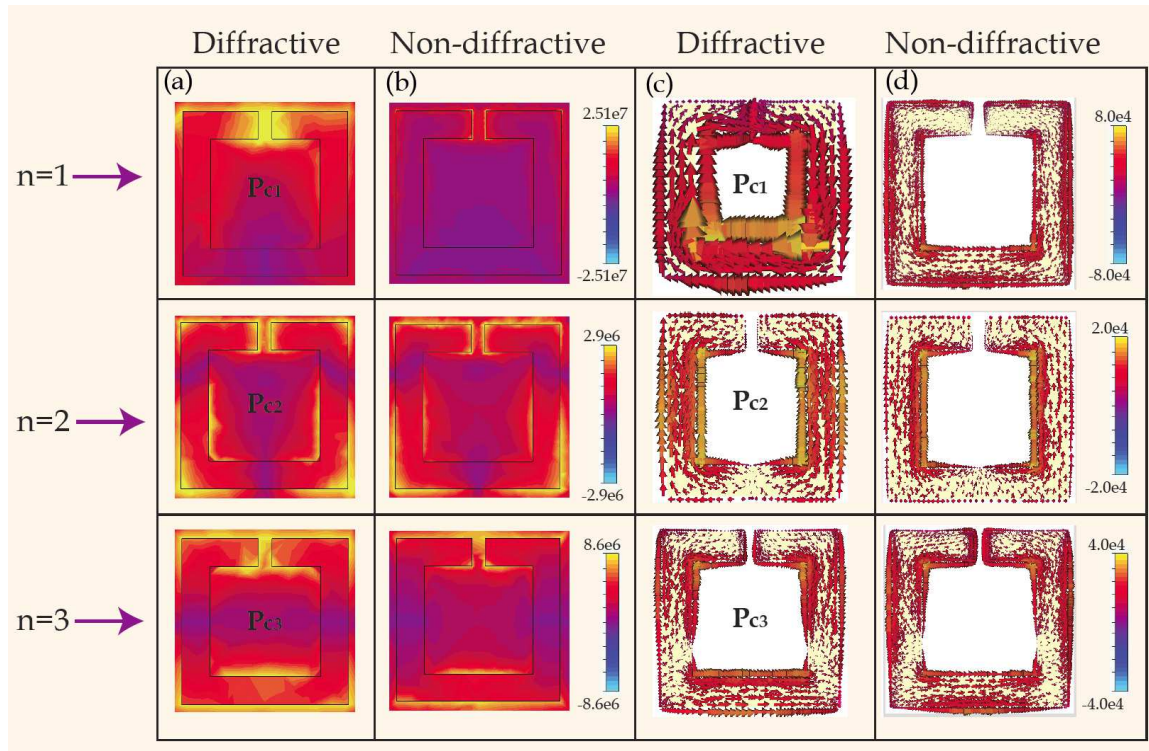
Figure 5-5 Surface currrents and electric filed of diffractive and non-diffractive mode. (a) and (c) Electrical field and surface currents of diffractive mode for Lorentzian (n = 1), Quadrupole (n = 2) and dipole modes (n = 3) with correspnding lattace constants at 180, 60 and 80 μm. (b) and (d) Electrical field and surface currents of non-diffractive mode of 40 μm lattice constant for LC (n = 1), Quadrupole (n = 2) and dipole modes (n = 3).

5.5 Electromagnetic field distribution

In order to elucidate the underlying physics mechanism on the sudden gain of the Q factor. The electric field and surface currents are simulated for the diffraion matching mode and non-diffraction mode, as shown in Figure 5-5(a) to 5(d). For n = 1 LC at diffraction matching mode with critical lattice constant P_{c1} = 180 μm, the electrical fied confined in the SRR gap is much stronger than that in the non-diffraction mode with lattice constant P = 40 μm. Accordingly, the surface currents flowing on the individual SRR in matched lattice mode are stronger than that in the non-diffraction mode. In the following two rows, the electrical field distrubtion is concented at the four corners for the dipole mode, and located at the gap and the cross grider for the qudrapole mode. We observed a field enhancement at these locations in the diffraction mode compared to the non-diffraction mode. At diffractive mode matching point, the scattered field conserved in the metasurface is constructively interferenced, which renders a high efficient energy restored in the system instead of radiating to the free space. It reveals a more tightly field confinement configuation due to low radiation loss of the resonant mode. Intuitively, the surface currents in Figure 5-5(c) are also showing more densed and powerful distribution compared to that in non-diffraction mode, as shown in Figure5-5(d).

5.6 Conclusion

We successfully tailored the line shape and the Q factor of the all the eigen modes by engineering the periodicities of the metasurface arrays. It is proved that the far-field diffraction mode matching is one of the most efficiently ways to enhance the Q factor dramatically, which is also the main distinction from the near-field coupling. We obtained an order of magnitude enhancement in Q factor by tuning the far-field diffraction mode. All three modes LC (n = 1), Dipole (n = 2) and Quadrupole (n = 3) modes under proper external field excitation can be easily tuned by varying the lattice constants. Then we observed at the diffraction mode the electric fields and surface currents are well trapped instead of radiating to the free space. In the metasurface system, the diffraction mode management allow us to expand it to a broad spectrum of electromagnetic waves from radio frequency to the visible light region.

CHAPTER VI

FANO TALKS WITH LORENTZ: ELECTROMAGNETICALLY INDUCED
TRANSPARENCY AND ABSORBANCE

6.1 Introduction and background

In recent years, the metamaterial system has been considered as a perfect system to mimic the quantum phenomenon. Benefitting from the artificially designed subwavelength meta-atoms, a number of classical analogues of quantum phenomena have been eventually realized in a metamaterial system. One of the famous quantum interference electromagnetically induced transparency (EIT) effect can be analogue in diverse metamaterial designs such as cut wires [78,79], bilayer fish-scale structures [80], SRRs [13,81-83], and asymmetric Fano resonators [84-85]. For asymmetric Fano resonator or asymmetric double SRRs with one gap deviated from the center, EIT is achieved by symmetry breaking. Motivated by the classical EIT analog in asymmetric Fano resonator, we demonstrated a dual EIT effect mimic by near-field coupling a LC resonance to a EIT band. Compared to the one transparency window emerged from the opaque background due to destructive interference for the EIT effect, two transparent windows are created in four-level tripod atomic energy system, which leads to a double EIT effect. Majority of the previous works in metamaterial based EIT systems have been focused on a single transparency window that emerges from an opaque background due to destructive interference. Here, we observe a dual transparency due to classical interference effect in planar coupled Fano-Lorentzian meta-atoms.

In previous works, double EIT has been studied mostly in multi-resonator systems [86-89]. For instance, it has been realized from the hybridization between two dark atoms in a bright-dark-dark configuration or as a coupling effect between two bright atoms in a bright-bright-dark configuration [86-88]. We study the dual transparency and absorbance effect in two resonator system by concentrically coupling a Lorentzian SRR (inner) and a Fano ASRR (outer) resonator, which results in dual EIT band and corresponding strong absorbance. It allows us to further engineer the amplitude and the width of the absorbance window by gradually scaling the size of the inner SRR and thus changing the coupling between the Fano and the Lorentzian resonators. We employed a four-level tripod quantum interference model via bright-dark-dark state coupling to interpret the observed DEIT results. Such planar terahertz metasurface associated with both of electromagnetically induced transparency (EIT) and electromagnetically induced absorption (EIA) could have the potential to be used as a multi-band slow-light devices, narrowband absorbers, and electromagnetic filters.

6.2 Sample design and fabrication

The DEIT planar metasurface system is made of two-dimensional arrays of metamolecules, which consist of two types of resonators, those are ASRR and smaller SRR located inside the ASRR, shown in Figure 6-1(a). The ASRR characterized with EIT-like feature served as the bright mode, while the SRR characterized LC feature served as the dark mode. The two resonators are properly designed to have nearly the same frequency resonance at the EIT window and LC resonance. At the spectral coupling range, frequency detuning of SRR and ASRR mainly determines the spectral position, shape and strength of transmission dip corresponding to the absorbance window. With varying inner SRR size within a fixed size ASRR, a series of planar metasurface samples were designed and fabricated. The length of SRR l_2 is varied from 19 to 22 μm, while maintaining the other geometrical parameters constant as P = 70 μm, l_1 = 60 μm, w = 6 μm, d = 10 μm and g = 3 μm. There is a transparent peak emerged in the background due to symmetry breaking in ASRR, which is characterized as the EIT peak while the SRR exhibits a Lorentzian inductive-capacitive resonance dip. The EIT peak in the ASRR is designed to yield at the diffraction mode matching region, which leads to a high Q factor of the transparency peak. Their resonance frequencies are designed exactly identical to ensure good near-field coupling between them. In Fano-Lorentzian metasurfaces system, the frequency detuning of either the EIT peak or the LC resonance dip significantly influences the spectral position and strength the of transmission dip that corresponds to the absorbance window.

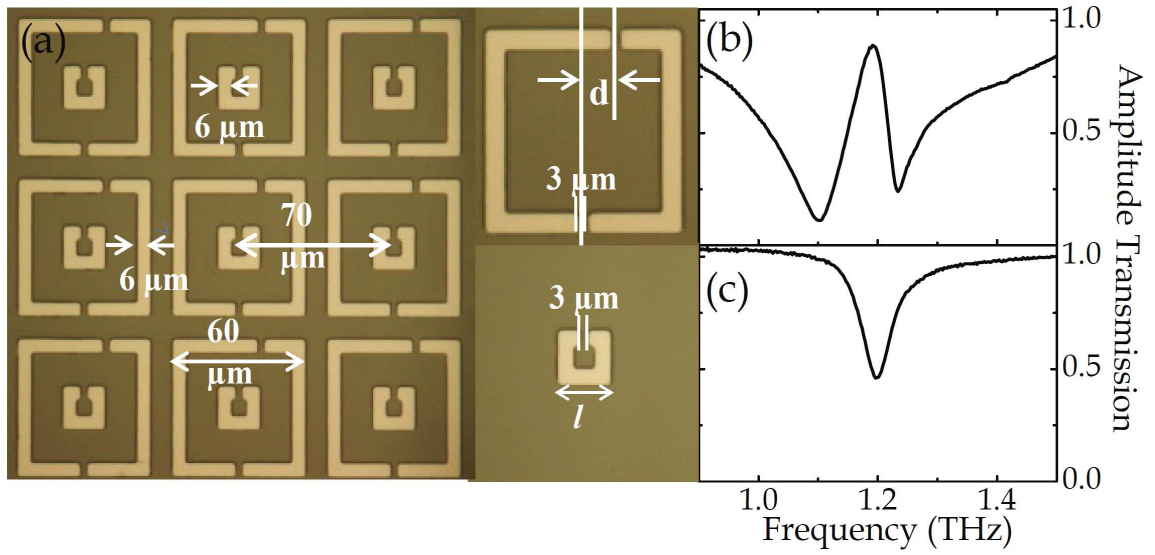**Figure 6-1**. Microscopic image of the metasurface sample. (a) Microscopic image of the planar sample with lattice constant = 70 μm, width = 6 μm, displacement d = 10 μm, length of the asymmetric Fano resonator = 60 μm, gap of SRR = 3 μm, side length l of SRR is varying from 19 to 22 μm. (b) Measured transmission amplitude of the ASRR. (c) Measured transmission amplitude of the 19 μm SRR.

6.3 Experimental characterization

We employed a photoconductive switch-based $8f$ confocal THz-TDS system to characterize the amplitude transmission spectra of the planar double EIT metasurface sample [49-50]. Illuminated by the 3.5 mm THz beam waist, at normal incidence with the electric field along the SRRs gap, the transmission amplitude is measured and defined as $|t(\omega)| = |E_t(\omega)/E_i(\omega)|$, where, the transmission spectrum $E_t(\omega)$ of the sample is normalized by $E_i(\omega)$ of the blank silicon substrate reference. . Since the sharp transmission dip corresponding to the absorbance window is generated in the narrow EIT transparency window, it means the narrower absorbance window would emerge. Thus, a unique measurement technique with high frequency resolution is required to obtain the high quality Fourier transformed frequency spectra. We attached a 1 cm thick high resistivity double-side polished silicon plate to the rear side of the metasurface sample which allowed us to delay the Fabry-Perot reflections arising from the rear surface of the metasurface substrate. This technique allowed us to scan for up to 200 ps, thus enhancing the spectral resolution from 60 GHz to 5 GHz . The measured resonant features of the coupled ASRR and the SRR of length 20 μm are shown Figure 6-1(b) and 1(c). The resonance frequencies of the classical EIT-like lineshape for ASRR and the LC resonance dip for SRR are located at ~ 1.19 THz, respectively. It shows the nearly identical resonance frequencies and the different damping rates of the EIT window and LC resonance, which ensured a strong near-field coupling between the ASRR and SRR. The transmitted terahertz time-domain pulse through the blank silicon substrate (reference), ASRR and coupled DEIT samples are shown in Figure 6-2. The inset of the Figure 6-2 shows the zoomed spectral response from 5ps to 40 ps in time domain, where the strong oscillations occur in the ASRR and planar DEIT sample compared to the reference. The oscillated sinusoid shown in Figure 6-2 top row reveals the deletion of parts of the signal in the time domain, which result in the transmission dip, thus the new envelope of the sine oscillation of planar DEIT sample indicate
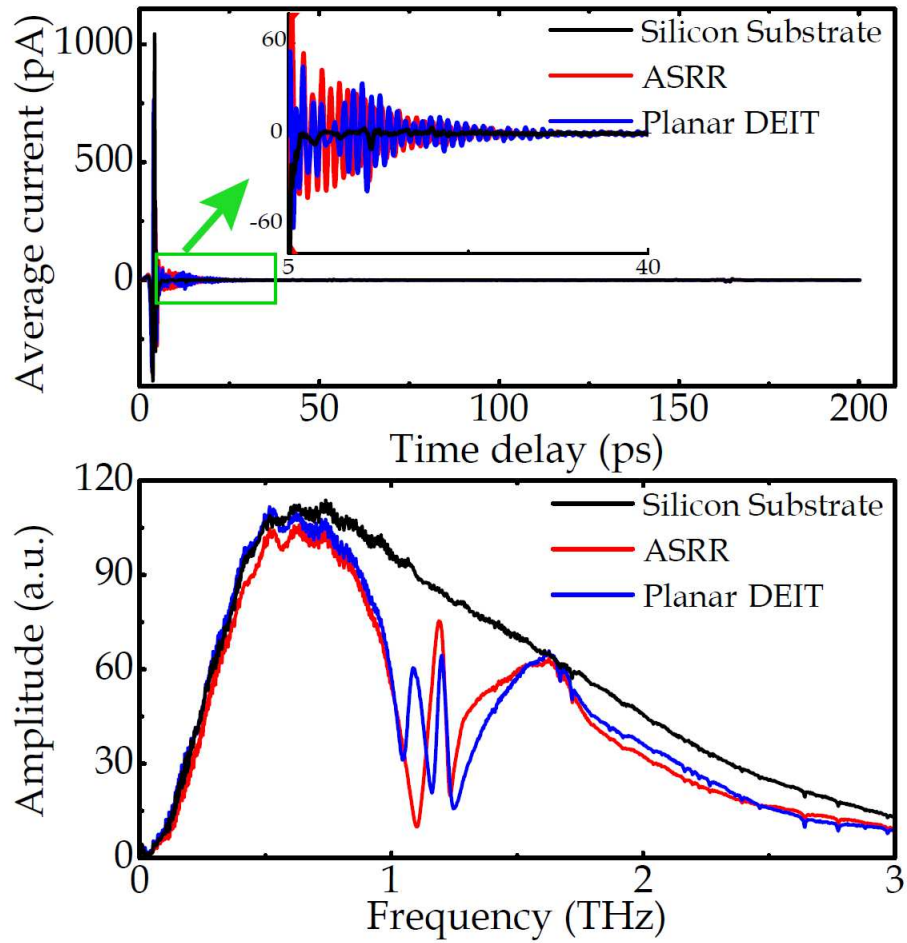
Figure 6-2. Comparison of three samples in measured time and frequency domain spectra. Top row: Terahertz time-domain spectra for comparison of blank silicon substrate as reference, ASRR and planar DEIT sample. Bottom row: Fourier transformed frequency-domain spectra of blank silicon substrate as reference, ASRR and planar double DEIT sample.

another new transmission dip created in the transparency window. The corresponding Fourier transformed frequency-domain transmission spectra for three samples are shown in Figure 6-2 bottom row. Compared to the classic EIT effect observed in bare ASRR sample, a pronounced transmission dip created in the EIT window of planar DEIT metasurface is induced through the near-field coupling between ASRR and SRR.

6.4 Transmission and absorbance spectra

We carried out a Microwave Studio to obtain the transmission response of the planar DEIT samples. With the E-field polarized along the gap arm of the resonators, the LC resonance is induced in SRR that couples with the ASRR transparency window, resulting in a pronounced dip in the transmission, which forms the absorbance window. Figures 6-3(a)-3(e) illustrate the simulated transmission spectra of the bare ASRRs and planar coupled ASRR and SRR samples with gradually increasing size of inner SRR coupled to a fixed 60 μm ASRR. In order to modulate the depth of the absorbance window, the SRRs size is designed to gradually increased to enhance the frequency detuning and alter the near-field coupling between the concentrically placed resonators. As the SRR size is increased, the absorbance dip becomes more pronounced, giving rise to a double EIT spectrum. As shown in Figures 6-3(b)-3(e), we observe that as the size of the inner SRR is increased from 19 to 22 μm, the amplitude and the linewidth of the absorption dip increases which indicates the trade-off between the Q factor and the depth of the absorbance. The corresponding simulation results for the proposed DEIT structures are shown in Figures 6-3(g)-3(i) which show good agreement with the measured results. The LC resonance in individual SRR array is as a result of the circulating currents at resonance frequency with the incident electric field is parallel with the gap of the SRR. In ASRR arrays, the transparent window occurs due to symmetry breaking which is induced by moving the top split gap away from the center (asymmetry displacement $d = 10$ μm).
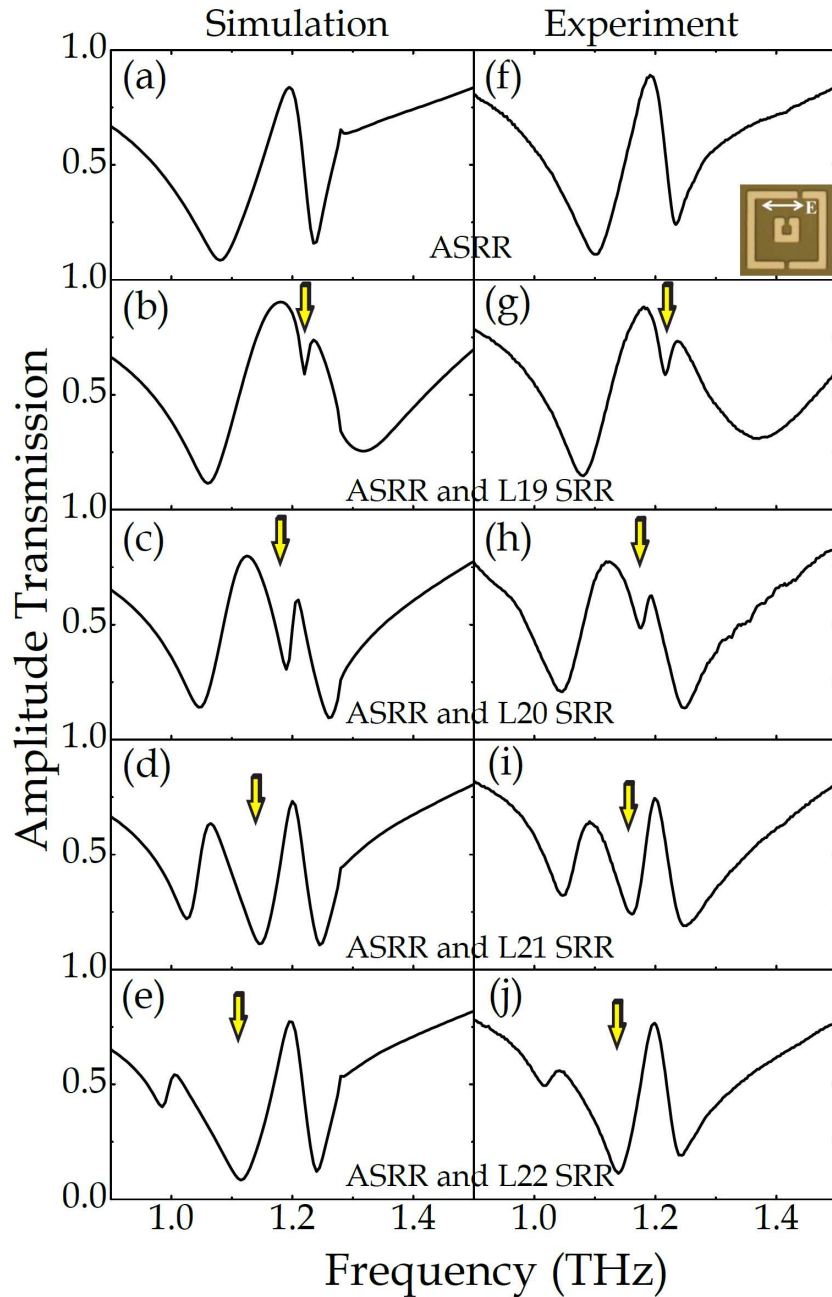
Figure 6-3 Simulated and measured transmission amplitude. Simulated (a)-(e) and measured (f)-(j) transmission spectra with the electrical field parallel with the SRR gap. (a) and (f) Transmission spectra of the ASR. (b)-(e) and (g)-(i) Transmission amplitude of the planar DEIT sample with the inner SRR size varied from 19 to 22 μm, respectively. The arrows in the figure highlight the absorbance window which located between the dual EIT windows.

The out-of-phase surface currents oscillation caused by the symmetry breaking due to the resonance frequency difference of the two metallic arms renders a destructive interference in the field. It in turn results in a sharp transparency window emerging from the background spectrum of a broad dipole resonance. When the SRR are introduced in the Fano-Lorentzian structure (we also referred as the DEIT structure), the resonance frequencies of the SRR and the ASRR are designed to have identical and possess contrasting decay rates. In such coupled system, a sharp absorbance dip induced at the center of the transparency is as a result of the interference of the fields near the resonance, which is due to the opposing phases of the near fields between the SRR and ASRR. Figure 6-4(a) and 4(b) illustrated the simulated and measured transmission spectra of the bare ASRR and proposed planar DEIT samples with E field polarized perpendicular to the SRR gap. It is worth noting that all of five curves, which exhibit the classical Fano resonance feature maintain nearly the same spectral response including ASRR, as well as the inner SRR sized varying from 19 to 22 μm. With the electric field polarized perpendicular to the gap of the SRRs, the classical Fano resonance and dipole resonance are excited in the ASRR and SRR separately. The coupling between the ASRR and SRR is forbidden due to the characterized resonance feature are not located in the effective spectral range. The experimental transmission shows good agreement with the simulated transmission spectra.

The absorbance is defined as $A(\omega) = -\ln[t(\omega)]$. We extracted the normalized absorbance spectra, as shown in Figure 6-5 to further observe the evolution of the absorbance window as the increase in the inner SRR size. Figures 6-5(a) and 5(f) show the simulated and measured spectra of the individual ASRR array, while Figures 6-5(b)-5(e) and 5(g)-5(j) depict the simulated and measured absorbance spectra for the coupled DEIT samples with varying size of the inner SRR while maintaining a fixed size of the outer ASRR. As the size of the inner SRR is gradually increased from 19-22 μm, the amplitude and width of the absorbance peak increased due to the change in the near-field coupling between the two resonators. The magnitude of the absorbance window is
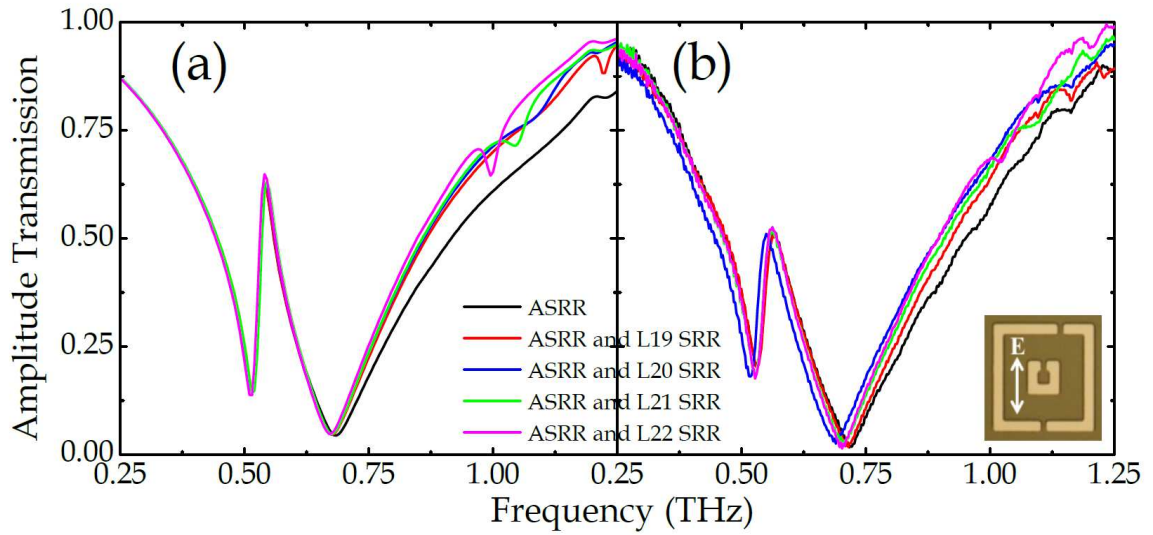
Figure 6-4. Simulated and measured transmission with E field perpendicular to the gap. Simulated (a) and measured (b) transmission spectra of the ASRR and planar DEIT samples with the electrical field perpendicular to the SRR gap. The inside SRR size are varying from 19 to 22 μm coupled with the identical ASRR.
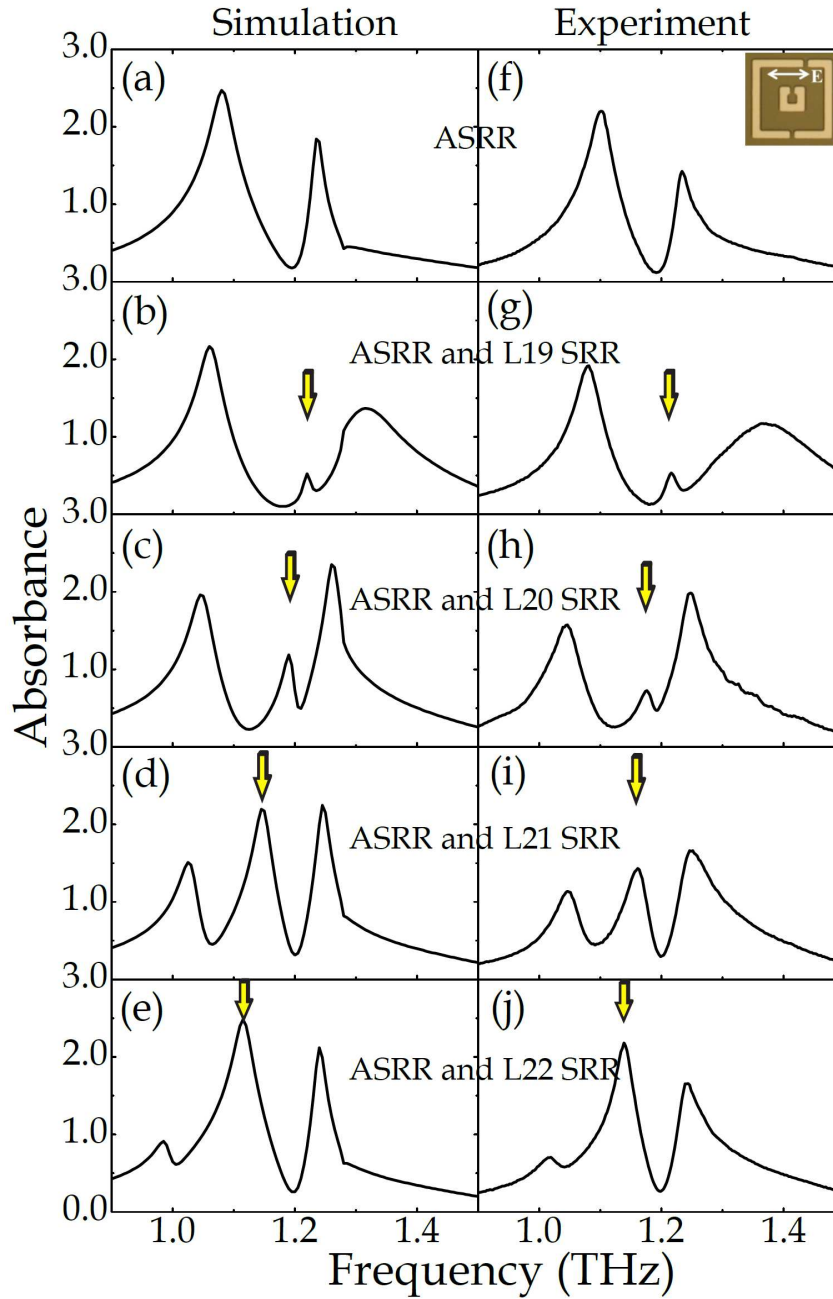
Figure 6-5 Absorbance spectra from simulated and measured transmission spectra. Simulated (a)-(e) and measured (f)-(j) absorbance spectra calculated from the transmission spectra with the electric field parallel with the SRR gap. (a) and (f) Absorbance spectra of only the ASRR.

increased from 0.53 to 2.16, while the width expands from about 10 GHz to 70 GHz, thus the Q

factor got enhanced from 27.8 to 122.0. It allows a large freedom of the modulation. The arrows in

the figure highlight the position of the absorbance peak which is located within the EIT window

6.5 Theoretical model

In order to understand the DEIT effect in the metamaterial system that gradually evolved through

the near-field coupling between the Fano and the Lorentzian resonances, we interpret it as a

classical analog of a four-level tripod quantum interference system [89]. By introducing the SRR

into the ASRR, we addressed as another metastable state joined, which result in the three-level EIT-

analog system was developed to four- level tripod DEIT-analog system (Figure 6-7(a)). This can

be analytically expressed based on the density matrix equation of motion for a system as [86,90],

$$
\begin{aligned}
&i(\delta_1 + i\gamma_1)\rho_{10} + i\Omega_{P1}/2 + i\rho_{20}\Omega_2/2 + i\rho_{30}\Omega_3/2 = 0, \\
&i(\delta_1 - \delta_2 + i\gamma_2)\rho_{20} + i\rho_{10}\Omega^*_2/2 = 0, \\
&i(\delta_1 - \delta_3 + i\gamma_3)\rho_{30} + i\rho_{10}\Omega^*_3/2 = 0.
\end{aligned}
\tag{6-1}
$$

where, ρ_{i0} are density matrix elements for the transition from $|i\rangle \to |0\rangle$ ($|i\rangle$ denotes the energy

levels $|1\rangle$, $|2\rangle$ and $|3\rangle$) with the energy levels shown in Figure 5(a), frequency detuning $\delta_i = \omega - \omega_{i0}$

with ω is angular frequency of the incident field and ω_{i0} is the resonance transition frequency from

$|i\rangle \to |0\rangle$, are the decay rates for the transition from $|0\rangle \to |i\rangle$. The transition between the $|0\rangle \to$

$|1\rangle$ is called the probe\dark transition that induced by the light field of Rabi frequency Ω_{P1}, whereas

the transition $|0\rangle \to |2\rangle$ is termed as the coupling/bright transition connected by the coupling field

of Rabi frequency Ω_2. These two transitions ($|0\rangle \to |2\rangle$ and $|0\rangle \to |1\rangle$; also called the bright and

dark transitions) form the standard Lambda (Λ) type transition that leads to the EIT window. The
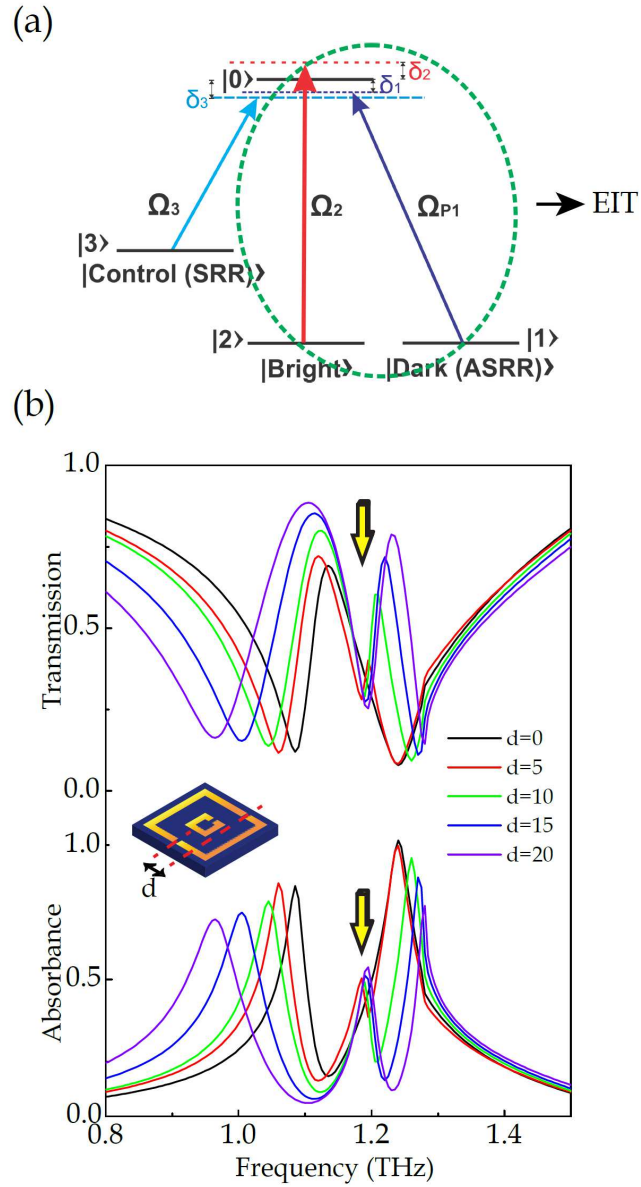
Figure 6-6 Schemes of four-level tripod system and simulated spectrum of the Fano-Lorentzian coupled resonators with assymetry sweeped. (a) Energy level diagram of the four-level tripod system that mimics the bright-dark-dark coupling in the proposed planar DEIT structure. The green dot circled states |1> and |2> correspond to the ASRR EIT resonance shown in Figure 6-3(a) and 3(f), whereas state |3> acts as a control state to modulate the DEIT resonances. δ_1, δ_2 and δ_3 are the detuning of the bright and dark excitations. (b) Simulated transmission and absorbance spectrum of the sample with the asymmetry of the Fano resonator varying from 0 to 20 μm.

transition $|0\rangle \rightarrow |3\rangle$ induced by the field of Rabi strength Ω_3 is termed as the control state, which

splits the EIT window by inducing a sharp absorption at the center of the transparency peak. Thus,

the energy level diagram of the four-level tripod system that mimics the bright-dark-dark coupling

in the proposed planar DEIT structure can be described in Figure 6-6(a). The elements in the density

matrix ρ_{20}, ρ_{10} and ρ_{30}, respectively represent the bright-dark-dark excitations in the system, as

shown in Figure 6-6(a). The SRR with the sharper linewidth is defined as the control state, also

being the quasi-dark state, while the ASRR without asymmetry is defined as the bright-dark

resonator. They are interacting to give rise to a double EIT resonance within the broad dipolar

resonance. In this system the, symmetric outer two-gap SRRs served as a bright mode with a broad

dipolar resonance. The dark states are introduced by introducing an asymmetry in the outer two-

gap SRRs to induce the SRR to ASRR by positioning the inner single gap SRR concentric to the

ASRR structure. In such a configuration of ASRR-SRR coupling, the two dark states compete with

the bright mode in a certain fashion to split the EIT resonance band into two, where the inner SRR

acts as the control state to induce a sharp absorbance at the center of the EIT window. As the SRR

size is scaled, the strength and the frequency of the transmission dip varies, which in turn controls

the nature of the DEIT peaks in the system. As shown in Figure 6-3, when the size of the inner SRR

is increased from 19 to 22 μm, the transmission dip gradually broadens and then undergoes a red

shift in the resonance frequency. In contrast, the asymmetry of the outer two-gap SRR is not being

able to dominate the coupling effect between the ASRR and concentric inner SRR, thus it served

as an EIT dark state. Figure 6-6(b) shows the transmission and corresponding absorbance spectra

of the ASRR coupled with the inner SRR of length 20 μm, while the asymmetry d of ASRR is

varied from 0 to 20 μm. Without the asymmetry, the coupling between the outer two-gap SRR and

the inner concentric SRR render the classical EIT effect, which implies that the four-level tripod

system is degraded to a classic three-level scheme (represented by levels |2>, |0> and |3> in Figure

6-7(a)). As the asymmetry is introduced, a transmission dip and corresponding small absorbance emerged. However, the absorbance window maintains stable without any spectral shift, when the asymmetry of ASRR is increasing from 5 to 20 μm. This is because under such configuration the coupling distance between the SRR and ASRR is kept constant and the shift in the resonance frequency of the ASRR is negligible which explains the observed zero shift in the frequency of the absorbance peak. In the engineered control state, the red shift in the resonance is due to gradual frequency mismatch between the ASRR and SRR resonators.

6.6 Data analysis

In order to elucidate the coupling mechanism between the SRR and ASRR, we simulated the surface currents and the electric field distribution of the individual ASRR array, individual SRR array and the coupled DEIT array, as shown in Figures 6-7(b), 7(e), 7(h) and 7(c), 7(f) 7(i), respectively. In the ASRR arrays, the distribution of surface currents and the electric field observed at the EIT transmission peak frequency reveals a quadrupole nature. At frequency 1.19 THz, the out-of phase currents on the adjacent arms of ASRR significantly reduces the radiation loss from the scattered field, which contributes to a transparency window, as shown in Figures 6-7(a), 7(b) and 7(c). The excitation of the LC resonance in the SRR structure are dictated by the circular surface currents and the strong electric field confinement in the gap of the SRR resonator, as shown in Figure 6-7(e) and 7(f). In the coupled ASRR and SRR system, the optical properties of the system is dictated by the nature of interference between the surface currents of the inner SRR and two branches of the quadrupole featured in the ASRR. When the two resonators are coupled together, the trapped electromagnetic energy associated is dictated by the loss of the electromagnetic field, which leads to a transmission dip within the EIT window. As the size of the inner SRR is gradually
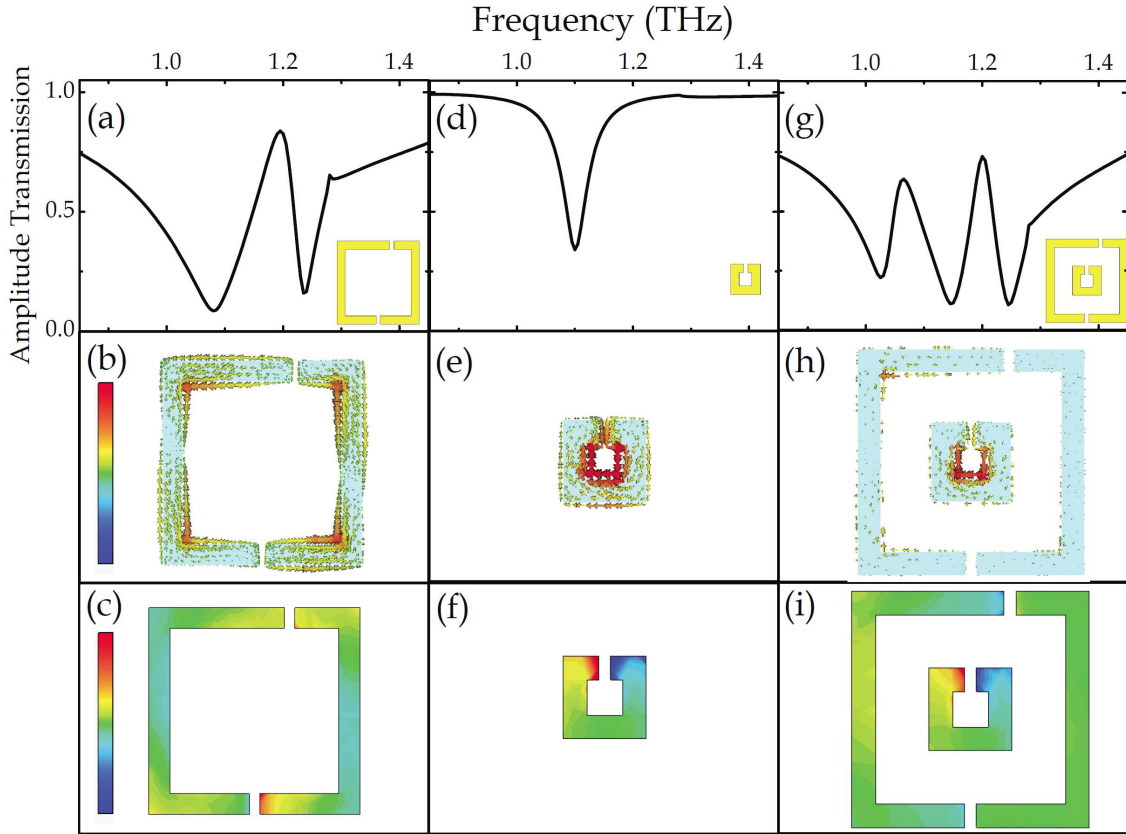
Figure 6-7 Surface currents and electric field of individual and coupled ASRR and SRR. (a), (d) and (g) simulated transmission spectra of the only ASRR, only SRR and ASRR coupled with SRR metasurface arrays. (b) and (c), (e) and (f), (h) and (j) Simulated electric field distribution and surface currents of only ASRR, only SRR and coupled ASRR with SRR, respectively.

increased from 19 to 22 µm, the coupling between the ASRR and SRR decreases, which leads to a strong deviation in the surface currents of the SRR and ASRR in the coupled DEIT system. By solving the coupled equations (6-1) in the steady state approximation, the optical coherence Im (-$\rho 10$) corresponding to transmission amplitude of the four-level tripod model system can be obtained in Figures 6-8(a)-8(d). It illustrates the evolution of the optical coherence response Im (-$\rho 10$) of the planar DEIT samples, which is consistent with the observed transmission spectra shown in Figures 6-3(g)-3(j). We obtained a good agreement of our theoretically models data with the observed transmission evolution for the coupled Fano-Lorentzian metasurface samples, through finely adjusting the transition frequencies, coupling strengths and the decay rates. To probe the variation of the coupling effects between the ASRR and SRR resonators, the surface current distributions on the gradually increasing size of inner SRR and ASRR are presented in Figures 6-8(e)-8(h) and 8(i)-8(j), respectively. When the sized of inner SRR is increasing from 19 to 22 µm, the strength of the surface currents concentrated on the inner SRR is pronouncedly weakened, which is mainly due to the increase in the frequency offset between the ASRR and SRR, leading to a significant increase in the coupling strength. The frequency match configuration between the ASRR and the SRR resonators are designed at 22 µm SRR size with fixed outer ASRR size. Furthermore, the enlarged inner SRR reduces the separation between the ASRR and SRR, and further enhances the near-field coupling between them. It is worth noting that matching the resonance frequencies of the EIT window and the LC resonance of the two resonators lead to extremely higher quality factor absorbance window ($Q \sim 122$ for the inner SRR size of 19 µm). This fascinating phenomenon allows us to engineer the intensity and the Q factor of the absorbance window by manipulating the coupling between the quadrupole and LC resonance modes.
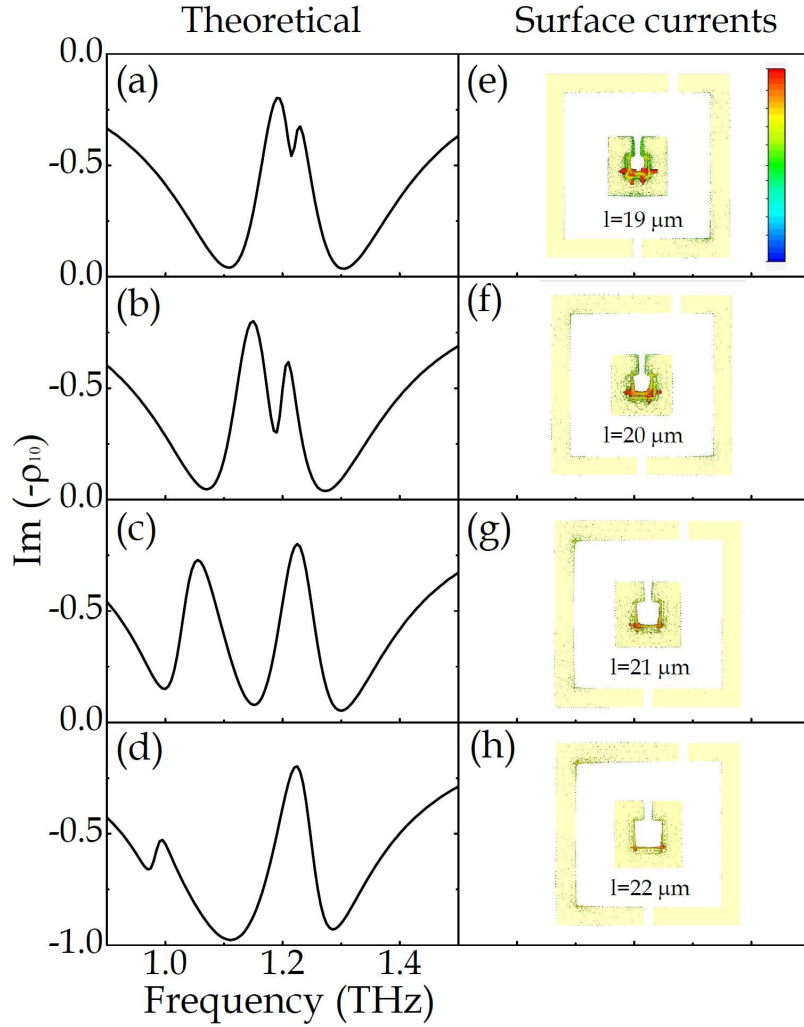
Figure 6-8 Theoretical four-level optical coherence and surface currents. (a)-(d) Optical coherence of four level tripod model corresponding to the transmission spectra the planar DEIT sample with the inner SRR size varying from 19 to 22 μm, respectively. (e)-(h) Simulated surface currents of the planar DEIT sample with the inner SRR size increasing from 19 to 22 μm, respectively.

6.7 Conclusion

Double electromagnetically induced transparency and absorbance is demonstrated in near-field coupling planar asymmetric Fano resonator and the common split-ring resonator. By introducing one Lorentzian resonator in the center of the Fano resonator, which results in superimposed destructive interference of the excitation scattering fields, we observed a strong absorbance window generated in the middle of the metamaterial induced transparency window. Manipulating the SRR dimension coupling with the same SRR leads to the modulation of the absorbance window with adjustable linewidth and magnitude. Furthermore we apply an atomic four-level tripod quantum interference model to fit evolution of the optical coherence corresponding to the transmission spectra for the variations of the inner SRR size, which validate the simulated and measured results. These DEIT analog metamaterial allows the potential applications on photonics switch, planar sensor, storage and communications

CHAPTER VII

CLASSICAL ANALOGUE OF ELECTROMAGNETICALLY INDUCED ABSORPTION IN A

THREE-RESONATOR METASURFACE SYSTEM

7.1 Introduction and background

Classical analog of EIT in metamaterials has been demonstrated extensively by its attractive

potential applications in light storage, slow light and sensing [78-80]. However, the counterpart of

EIT, electromagnetically induced absorption (EIA) has been studied rarely in coupled metamaterial

systems. Near-field coupling scheme in the subwavelength resonators gives rise to ability to mimic

the quantum phenomena in metamaterials. The EIT analog is a result of the coupling between a

bright and a dark resonator, where the destructive interference of the resonance modes delivers a

sharp window of nearly perfect transmission within a broad absorption band. The EIT effect has

been recently mimicked in various metamaterial approaches, including cut-wires, bilayer fish-scale

structures, split-ring resonators and asymmetric Fano resonators [78-85]. Compared to the

destructive interference of the coupled EIT resonators, a constructive interference of different

excitation pathways would lead to a new fascinating phenomenon EIA. This effect has been

realized in two coupled resonator systems by introducing a retardation-induced phase shift in an

intermediate coupling regime [18,92], or by manipulating their dissipative loss and coupling

strength [19], or by stimulating them with different phase via oblique incidence [93].

Here, we study the EIA effect in a vertically coupled three resonator metamaerials [94]. A well-defined absorption resonance is developed in the EIT window enabling a unique double-peak transparency, due to the magnetic resonance induced by the near-field coupling of the three resonators. The analog of EIA opens up a new route to advanced photonics devices.

7.2 Sample design and preparation

The three-resonator metasurface system comprised of three types of the resonators, those are I-shaped structure at the top layer, four-SRR structure at the middle layer and a cut-wire at the bottom layer. Each layer is aligned with the structural centers coinciding with the x-y plane and is then integrated with polyimide as a dielectric spacer separating the different layers. The I-shaped resonator and the cut-wire serve as the bright modes, while the four-SRR structure serve as the dark mode with a nearly identical resonance frequency and different damping rates. Figure7-1(a) shows the schematic diagram of the three-layered EIA metamaterial unit cell. The geometry of the individual resonators with detailed parameters as $P_x = P_y = 120$ μm, $t_1 = t_2 = 10$ μm, $l_1 = 110$ μm, $l_2 = 83$ μm, $t = 42$ μm, $w = 10$ μm, $a = 47$ μm, $d = 13$ μm and $g = 10$μm are labeled in Figure7-1(b). Figure7-1(c) displays a microscopic image of the fabricated sample and shows a perfect alignment between the three-layer resonators. The three-resonator EIA metasurface system was fabricated on a 625 μm thick isotropic silicon substrate ($\varepsilon_s = 11.96$) using conventional photolithography process and thermal metallization of 200 nm thick Al films. The bar structures in the bottom layer were first patterned on the bare Si substrate, followed by 10 μm polyimide spacer ($\varepsilon_p = 2.96 + 0.27i$) on it. After the cure-heating cycles, the four-SRR structure in the middle layer was aligned
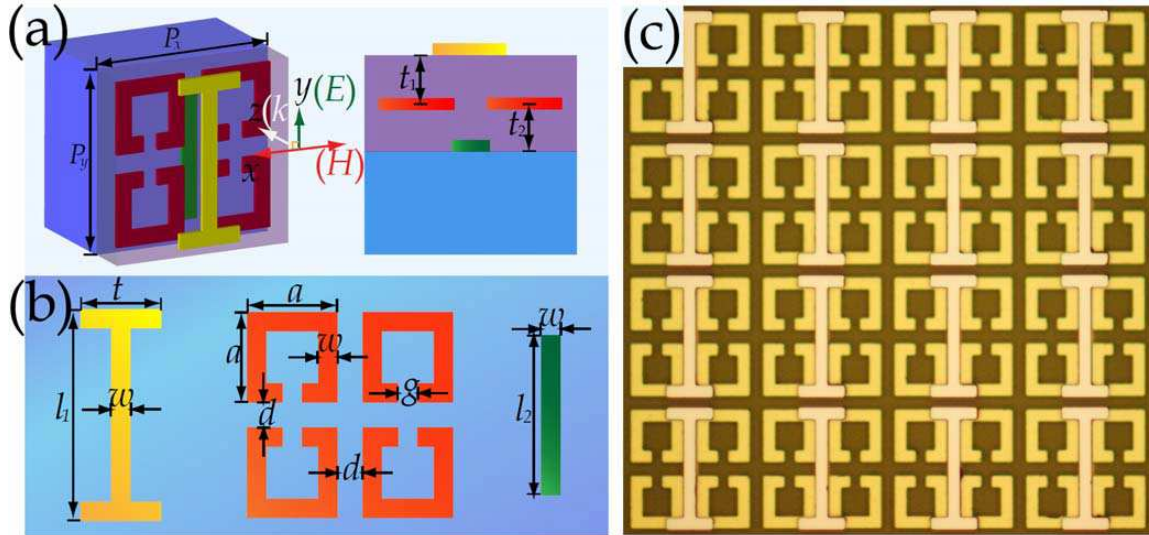
Figure 7-1. Schematic and microscopic image of EIA sample. (a) Schematic diagram of the three-layered EIA metamaterial unit cell. (b) Schematic of individual resonators. $P_x = P_y = 120$ μm, $t_1 = t_2 = 10$ μm, $l_1 = 110$ μm, $l_2 = 83$μm, $t = 42$ μm, $w = 10$ μm, $a = 47$ μm, $d = 13$ μm and $g = 10$ μm, respectively. (c) Microscopic image of the EIA sample (figure adapted from Ref. [95]).

and patterned on the polyimide spacer. Then, the second 10 μm polyimide spacer was applied and followed by the final I-shaped structure alignment patterning.

7.3 Experimental set-up

In order to investigate the optical properties of the EIA three-resonator metasurface system, the transmission $t(\omega)$ and reflection spectra $r(\omega)$ at normal incidence were measured by terahertz transmission and reflection system. The frequency-dependent absorption was then calculated as $A(\omega) = 1 - |t(\omega)|^2 - |r(\omega)|^2$. The amplitude transmission of the EIA metamaterial was measured using photoconductive antenna based $8f$ confocal transmission terahertz time-domain spectroscopy (THz-TDS) system with the minimum beam diameter illuminated on the sample being 3.5 mm, which is showed on chapter II Figure 2-2[50]. The amplitude reflection spectrum was measured using the same-type but reflective THz-TDS system, which is showed on figure 7-2[96]. The reflected terahertz beam is guided through a beam-splitter (BS), M3, M4 and M5 from the sample to the receiver. The amplitude transmission and reflection are defined as $t(\omega) = |E_{st}(\omega)/E_i(\omega)|$ and $r(\omega) = |E_{sr}(\omega)/E_i(\omega)|$, respectively; where $E_{st}(\omega)$ is measured transmission spectrum, and $E_{sr}(\omega)$ is the reflection spectrum. They are both normalized by $E_i(\omega)$ with respect to the transmission or reflection amplitude of air and an aluminum coated silicon wafer, respectively.

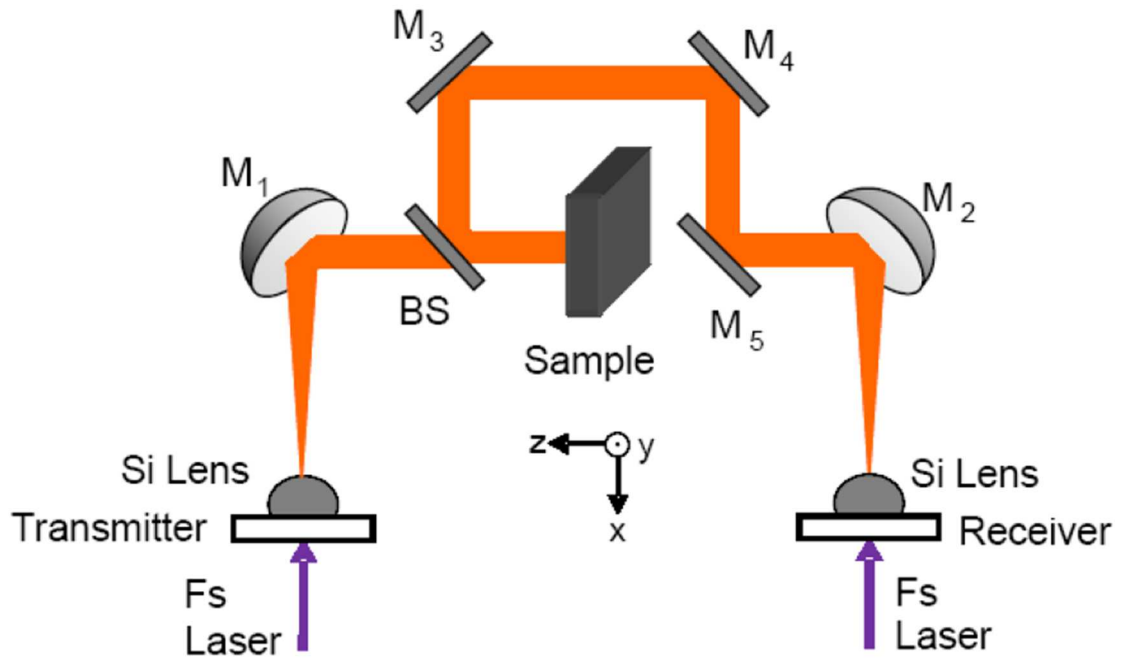**Figure 7-2**. Schematic diagram of the reflection THz-TDS (figure adapted from Ref. [96]).

7.4 Numerical, experimental and theoretical result

Numerical simulations of the EIA system were performed using the CST Microwave Studio. The transmission, reflection and absorption spectra are showed in the Figure 7-3(b). A pronounced sharp absorption resonance located at 0.58 THz is induced within the transmission EIT window through the three-coupled resonators. It is worth noting that at the EIA central frequency, unlike the previous reports [92-93], where the reflection spectrum was normally characterized as a resonance peak not a strong resonance dip in our case. This unique property impart a distinct pronounced absorption peak to the three-resonator metasurface system. The experimental transmission, reflection and absorption are shown in Figure 7-3(a) with a relative sharp EIA window of 70 GHz, which is in good agreement with simulation. We also found that the coupling effect in the EIA system is independent of whether the metamaterial is excited from the top or the bottom bright resonator. This is due to the extremely small spacer thickness which is $\sim \lambda/25$ of the terahertz wavelength. We confirmed this by exciting the metamaterial sample from the top layer as well as from the bottom layer and obtained identical transmission spectrum in the measurements and the simulations. To physically describe the resonance behaviors of the three resonators in the EIA system, three coupled equations (in rotating-wave approximation) were used [94]:

$$
\begin{aligned}
\dot{x}_t &= -i\omega_t x_t - i\kappa_{t-m} x_m - \gamma_t x_t + ig_t E, \\
\dot{x}_m &= -i\omega_m x_m - i\kappa_{t-m} x_t - i\kappa_{b-m} x_b - \gamma_m x_m, \\
\dot{x}_b &= -i\omega_b x_b - i\kappa_{b-m} x_m - \gamma_b x_b + ig_b E.
\end{aligned} \tag{7-1}
$$

where x_t, x_m, x_b; ω_t, ω_m, ω_b; γ_t, γ_m, γ_b are the amplitudes (corresponding to the level $|t\rangle$, $|m\rangle$ and $|b\rangle$ in quantum interpretation), resonance frequencies and damping rates of the top, middle and bottom resonators, respectively. g_t, g_b are coupling strength of the top and bottom resonators to the external field E. The intermediate resonator can only be excited by the coupling from the top resonator with coupling coefficient κ_{t-m} and the bottom resonator with coupling coefficient κ_{b-m}. According to Eq.
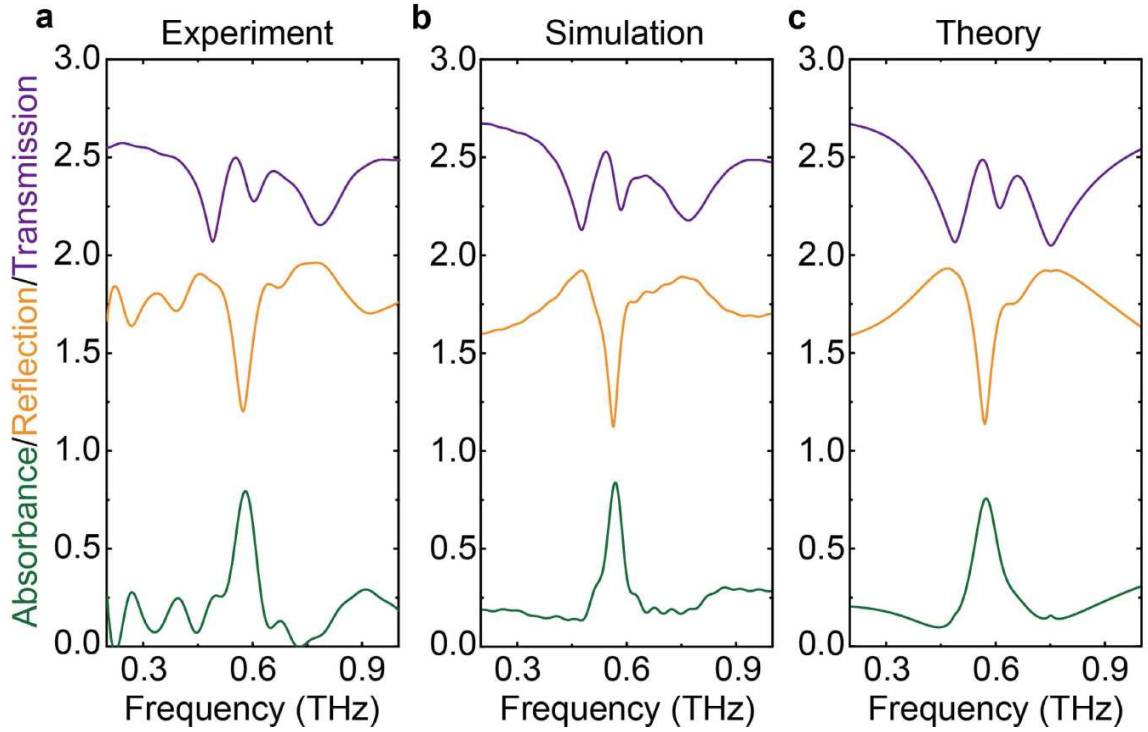
Figure 7-3. Amplitude transmission, reflection and absorption spectra. (a) Experimental, (b) simulated and (c) theoretical spectra of the amplitude transmission, reflection and absorption at normal incidence y-polarized wave. In (c), the parameters used in the calculation are: $\omega_t = 2\pi \times 0.61$ THz, $\omega_b = 2\pi \times 0.60$ THz, $\omega_m = 2\pi \times 0.64$ THz; $\gamma_t = 2\pi \times 0.018$ THz, $\gamma_m = 2\pi \times 0.013$ THz, $\gamma_b = 2\pi \times 0.007$ THz, $g_t = 2\pi \times 5.57$ MHz, $g_b = 2\pi \times 87.54$ MHz, $\kappa_{t\text{-}m} = 2\pi \times 0.0001$ THz and $\kappa_{b\text{-}m} = 2\pi \times 0.13$ THz, $d_p = 20$ μm, $d_s = 625$ μm. The offsets along the y-axis reflection and transmission are 1.0 and 2.0, respectively (figure adapted from Ref. [95]).

(7-1), we obtain the susceptibilities of the two bright resonators χ_t and χ_b, respectively. Thus the transmission and reflection coefficients at the two interfaces with bright resonators are calculated utilizing the method described in ref. [13]:

$$t_{1-\beta-2} = \frac{2cn_1}{c(n_1+n_2)-i\omega\chi_\beta},$$

(7-2)

$$r_{1-\beta-2} = \frac{c(n_1-n_2)+i\omega\chi_\beta}{c(n_1+n_2)-i\omega\chi_\beta}, \quad \beta = t,b.$$

(7-3)

Eq. (7-2), (7-3) are obtained under the case that the incident wave passes through metamaterial layer β from medium 1 with refractive index n_1 to medium 2 with refractive index n_2. Here c is the light velocity in vacuum and ω represents the angular frequency. With these obtained coefficients, we calculate the overall transmission and reflection coefficients of the EIA system, where the multi-reflection effect in the thin polyimide layer is also considered. Figure 7-3(c) shows the calculated result based on the model, showing excellent agreement with the measurements and the simulations.
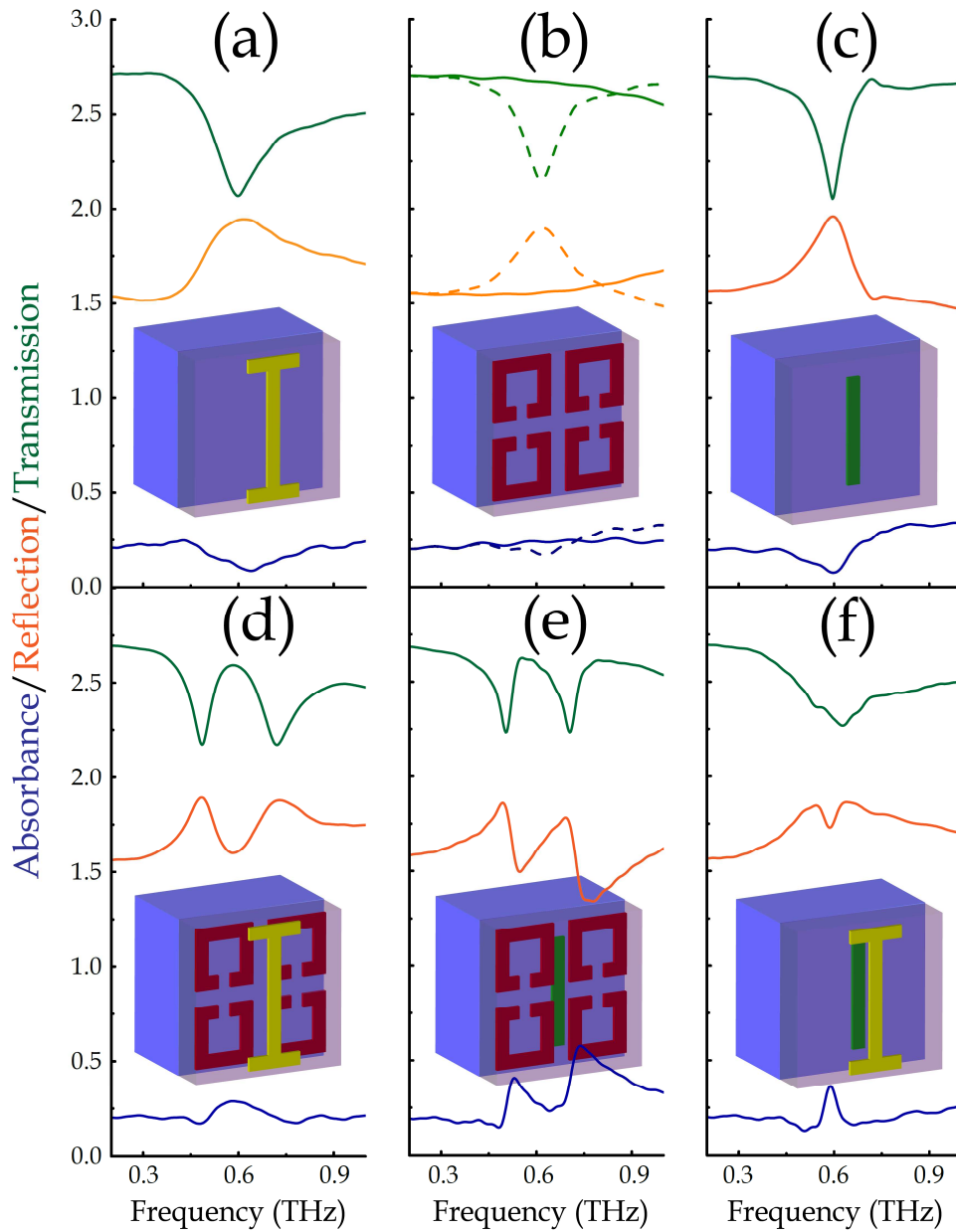
Figure 7-4. Simulated spectra of individual and cascaded resonators. Amplitude transmission (green), reflection (orange) and absorbance (blue) spectra of individual resonators (a), (b), (c) and three cases of two combined resonators (d), (e), (f), as indicated by the inset diagrams. All the solid curves are obtained under the normally incident *y*-polarized wave, while the dash curves in (b) are achieved under the normal incidence *x*-polarized wave (figure adapted from Ref. [95]).

7.5 Data analysis

To explore the coupling effect between the resonators within a unit cell, we performed simulations on the individual resonators and combinations of two of these resonators. Figure 7-4 presents the simulated transmission, reflection and absorbance spectra of various structures under y-polarized incident (solid curves) and x-polarized (dashed curves, in Figure 7-4(b) only) wave, respectively. The incident wave polarized along the y direction directly excited the I-shaped and the cut-wire resonators (Figure 7-4(a) and 4(c)) whereas the four-SRR resonator could not be directly excited (Figure 7-4(b)). When the I-shaped and four-SRR resonators (Figure 7-4(d)), or the cut-wire and four-SRR resonators are combined together (Figure 7-4(e)), a typical EIT type spectral response is observed with a pronounced transparency window. Therefore, the I-shaped and the cut-wire resonators act as the bright modes as they are directly excited by the incident field, while the four-SRR resonator acts as the dark mode resonator since they are excited by the near-field coupling from the bright mode resonators. Furthermore, it is interesting to see that when the two bright resonators are cascaded together (Figure 7-4(f)), the coupling between them results in a broader but weaker resonance. However, none of the absorbance spectra in Figure 7 displays an absorption resonance which is as strong as that in the three-resonator system, although the cases in Figure 7-4(e), 4(f) reveal a small absorption feature. Therefore, the remarkable EIA effect in the proposed multilayer system is indeed attributed to the vertical coupling between all the three resonators. In addition, retrieved effective real and imaginary components of permittivity ε_{eff} and permeability μ_{eff} shown in Figure 7-4(g), 4(h), 4(i) correspond to the three cases of two cascaded resonators, as shown in Figure 7-4(d), 4(e), 4(f), respectively. The classical dispersion caused by the EIT effect is observed in Figure 7-4(g) and 4(h).

To further explore the physical process, we calculated the electromagnetic surface current distributions of selected designs. For the bright resonators, the surface currents of the top I-shaped resonator and bottom cut-wire resonator display $a \sim 0.4\pi$ phase difference at the resonance

frequency. In other words, when the current in the I-shaped resonator is the strongest, the current in the cut-wire resonator nearly becomes the weakest, and vice versa, as seen in Figure 7-5(a) and 5(b). After adding the four-SRR resonator as the middle layer, the surface current distributions in the two bright resonators are significantly altered because of their near-field coupling with the dark SRRs in the intermediate layer. Figure 7-5(c), and 5(d) indicate that there is a phase difference of π between the I-shaped and cut-wire resonators at the peak absorption frequency. As a result, the anti-parallel currents form a magnetic dipole, as indicated by a current ring. Different from the trapped mode in the planar metamaterial, The EIA metamaterial system can also be considered as the analog of the quantum four-level atomic system with two different excitation paths: $|0\rangle \rightarrow |t\rangle$ and $|0\rangle \rightarrow |b\rangle \rightarrow |m\rangle \rightarrow |t\rangle$, as well as $|0\rangle \rightarrow |b\rangle$ and $|0\rangle \rightarrow |t\rangle \rightarrow |m\rangle \rightarrow |b\rangle$ as shown in Figure 7-5(e), which constructively interfere with each other when dark SRR resonator drastically change the resonance phase of the two bright resonators, thus leading to the EIA effect. It can be clearly seen that the surface currents at the top and bottom resonators are both enhanced in comparison with the case shown in Figure 7-5(a), and 5(b). Here t, m and b represent the top, middle and bottom resonators, respectively. It should be noticed that the EIA effect described here does not convert the transparency window into a dip (inserting the second bright resonator into the cases shown in Figure 7-5(c), and 5(d), but rather creates an absorption resonance within the transparency window. This may be due to different damping rates of the two interference paths. Another feature of the proposed EIA system is that at the peak absorption frequency, the middle four-SRR resonator remains dormant. This is caused by the coupling between the top and bottom resonators that are canceled out with each other, owing to the opposite current directions. Namely, its two excitation pathways: $|0\rangle \rightarrow |t\rangle \rightarrow |m\rangle$ and $|0\rangle \rightarrow |b\rangle \rightarrow |m\rangle$ interfere destructively with each other. To confirm that the absorption phenomenon is resulted from the near-field coupling induced magnetic response, effective parameters of the EIA metamaterial are retrieved [97].
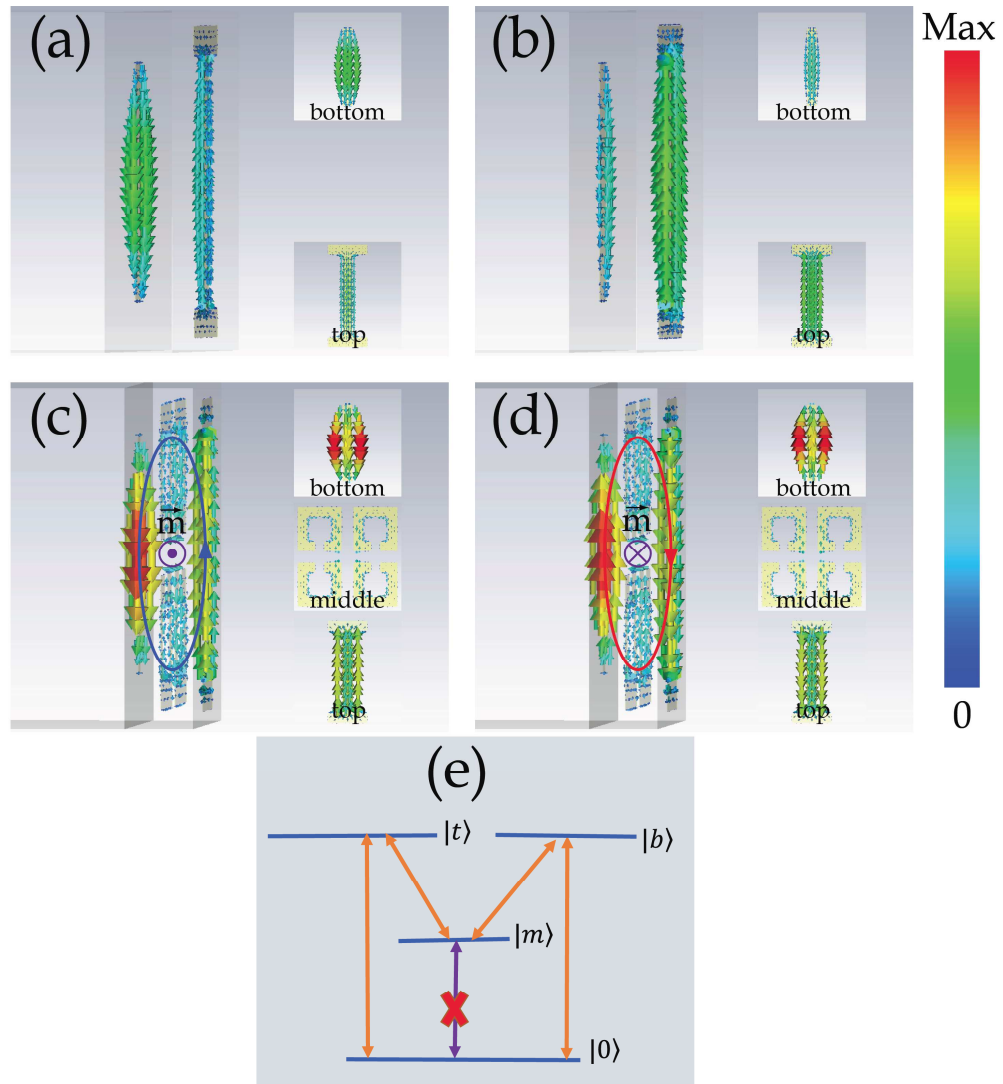
Figure 7-5. Simulated surface current distributions and diagram of four-level energy. (a), (b) For the case shown in Fig. 7-4(f) with $\varphi = 1.44\pi$ and 1.83π at resonance frequency. (c), (d) For the three-layer case with $\varphi = 1.44\pi$ and 0.44π at the peak absorption frequency. (e) four-level atomic system with two different excitation paths. Insets: corresponding surface current distributions of each layer resonator (figure adapted from Ref. [95]).

The three-layered structure in the polyimide is treated as an effective medium, as illustrated in Figure 7-6(a). By using the simulated transmission and reflection results, we obtained the effective permittivity ε_{eff} and permeability μ_{eff}, respectively, as shown in Figure 7-6(b) and 6(c). It is observed that μ_{eff} changes dramatically at the peak absorption frequency owning to the anti-parallel currents. Meanwhile, the anti-parallel currents reveal a weak contribution ε_{eff} since the electric response of the top and bottom resonances tend to cancel each other due to the π phase difference. This is clearly demonstrated in Figure 7-6(b) that the other two resonances without anti-parallel currents only contribute to ε_{eff}.
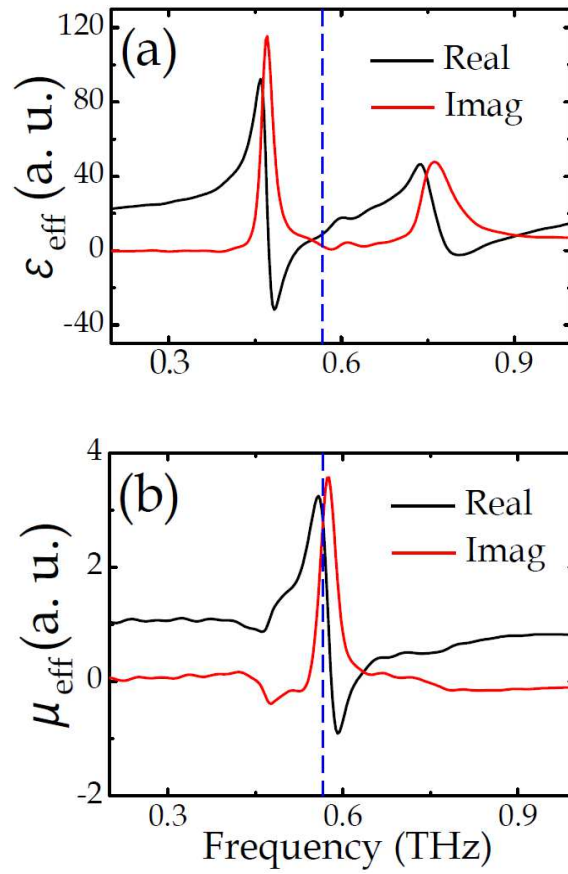
Figure 7-6. Effective permittivity and permeability. (a) and (b) Retrieved effective permittivity ε_{eff} and permeability μ_{eff} of three-resonator EIA metamaterial (figure adapted from Ref. [95]).

7.6 Conclusion

We demonstrate the quantum phenomenon of EIA in a vertically coupled three-layer classical metasurface. The scheme relies on a three-coupled-resonator unit cell, where a strong absorption resonance is induced from the magnetic response. The near-field coupling mechanism presented here would allow the design of EIA analogs across a broad spectrum of the electromagnetic waves. This composite metamaterial design also opens up a new route to classical analogs of quantum effects leading to photonic devices with promising applications in light switching, absorption, and sensing.

CHAPTER VIII

CONCLUSION AND FUTURE PLAN

8.1 Conclusion

Over the past decade, the exploration of novel photonics devices has concentrated on reproducing the classic and quantum effects in special exotic materials rather than in conventional bulk optical materials. In this dissertation, terahertz metasurfaces are studied in two mainly two aspects: collective coherent behavior and implementation of classical analog of quantum optics phenomena. Composed by artificially constructed metaatoms with ordered lattice periodicity alignment, collective coherent interaction in a meta-atom lattice is the key to understand the multifarious applications and functionalities. In the thesis, the collective coherence in nearest neighbor coupled metasurface is demonstrated in symmetric and asymmetric modes. Then a universal behavior in fractional frequency shift and linewidth of resonances are identified in the Lorentzian and Fano resonators. As the metasurface is an ideal platform to realize the quantum optics phenomena that are generally limited by rigorous experimental conditions, we successfully mimic the EIT and EIA in the near-field coupled subwavelength resonator system.

Interactions of the composite metamolecules play an essential role in the electromagnetic properties of metasurfaces. The near-field coupling effect of the subwavelength neighboring metamolecules dominated the collective coherence of the metasurface arrays. We study the frequency shift for all three differently sized SRRs and the Fano resonators covered from 0.5-1.5 THz. As the lattice constant is increased, the narrow trend of the linewidth is observed for all three differently sized SRR and the Fano arrays. These interesting behaviors allow us to identify a series of coherent universal scaling behavior. By analyzing the fractional frequency shift with the scaling lattice constants, we recognized a coherent metasurface ruler in the form of exponential decay due to mutual inductive coupling in the LC mode. For the Fano resonator arrays, based on the Lagragian model, we found that the fractional shift can also be persisted with a coherent metasurface ruler. Then, we further compare the universal behavior of the energy dissipation loss decay behavior with respect to the size scaling periodicities in SRR and the Fano arrays. We demonstrated that the time decay rate of the linewidth in the SRR arrays are size-dependent while it keeps constant in all different sized Fano arrays due to the cancellation effect of the Fano arrays. Identification of the collective coherence in metasurfaces enables us to explore the device for flat lenses, terahertz modulator and ultrasensitive planar sensors.

In addition to the near-field coupling mediating the collective coherent behavior, the far-field diffraction coupling can effectively tailor the lineshape of the eigen modes in metasurface arrays. We prove that diffraction mode management can depress the radiation loss and increase the Q factor of the resonance consequently. We obtained an order of Q factor gain in the LC ($n = 1$), Dipole ($n = 2$) and Quadrupole ($n = 3$) modes. All of the eigenmodes can be tailored in terms of diffraction mode matching by simply varying the lattice constants of the arrays. This work is promising in optimizing the design of subwavelength photonic devices.

Classical analogue of quantum phenomenon has been a popular topic across the broad electromagnetic spectrum from optics to microwave in metamaterial systems. Next, motivated by the idea of the induced transmission dip within the EIT window, we proposed a configuration to couple the EIT band to a Lorentzian resonance. In order to increase the frequency resolution of our measurements and make it consistent with the numerical result, a high resolution long scan measurement involved in broad δf confocal THz-TDS are employed to characterize the narrow transmission dip in the EIT window. This scheme leads to a dual transparency bands and a strong absorbance in the system due to interference between a bright and two dark modes. The two dark modes are defined as the asymmetric degree of the Fano resonator and the lorentzain mode of the SRRs. By adjusting the size of the SRR, the evolution of the absorbance window is capable to be modulated both in linewidth and magnitude. Finally, we use a density matrix equations based four-level tripod quantum system to theoretically model the absorbance of the Fano-lorentzian metasurfaces.

Compared with the extensively studied on EIT, EIA has been only explored rarely. Distinguished from the previous work, we demonstrate the genuine absorption by designing a vertically coupled three-resonator metasurface system. Due to constructively interference, a well-defined absorption peak within the EIT transparency window is achieved experimentally, which agrees well with the numerical simulation. Combined with the theoretical model and retrieved parameter, we demonstrate that the EIA occurred in the three-layer metasurface system is due to a magnetic resonance induced by the near-field coupling between the two bright and one dark resonators. This classical analog of EIA allows us to design novel photonics devise, such as narrow-band filters, switches and terahertz modulators.

8.2 Future plan

Actively controlled light modulation is always an interesting topic to purse. Being motivated by the Chapter VI, we simulate the active control of the dual transparency band. It shows that the dual transparency band can be converted to one transparency or a single dipole band by shorting the ASRR or SRR. Extreme high Q factor is an important subject to purse as well. By coupling the Fano resonance to the LC resonance, two Fano resonances emerged with higher Q factors. The Fano resonator coupled with two opposite orientations of Lorentzian resonators are proposed. The corresponding samples fabrication and the measurements will be carried out.

Next, we modeled a high efficiency dual band absorber based on Fano resonators due to abrupt change of the phase diagram. One of the absorption band can be tailored by engineering the asymmetry degree of the Fano resonator with the modulation varying from 0.3-0.9. From the simulation it is worth noting that the asymmetry degree, collective coherence behavior, spacer thickness and the permittivity of the analyte can alter the phase diagram with a sudden change. These fascinating phenomena are related to the modulation of the radiation and non-radiation losses. I will continue to probe this subject based on initial simulation work.

REFERENCES

1. Pendry, J. B., Holden, A. J., Robbins, D. J., & Stewart, W. J. (1999). Magnetism from conductors and enhanced nonlinear phenomena. *Microwave Theory and Techniques, IEEE Transactions on*, *47*(11), 2075-2084.

2. Yen, T. J., Padilla, W. J., Fang, N., Vier, D. C., Smith, D. R., Pendry, J. B., & Zhang, X. (2004). Terahertz magnetic response from artificial materials. *Science*, *303*(5663), 1494-1496.

3. Smith, D. R., Padilla, W. J., Vier, D. C., Nemat-Nasser, S. C., & Schultz, S. Composite medium with simultaneously negative permeability and permittivity. *Physical review letters* **84**, 4184-4187 (2000).

4. Shalaev, V. M. Optical negative-index metamaterials. *Nat. Photon.* **1**, 41-48 (2007).

5. Soukoulis, C. M., Linden, S. & Wegener, M. Negative refractive index at optical frequencies. *Science* **315**, 47-49 (2007).

6. Fang, N., Lee, H., Sun, C., & Zhang, X. Sub–diffraction-limited optical imaging with a silver superlens. *Science* **308**, 534-537 (2005).

7. Zhou, F., Bao, Y., Cao, W., Stuart, C. T., Gu, J., Zhang, W., & Sun, C. (2011). Hiding a realistic object using a broadband terahertz invisibility cloak. *Scientific reports*, *1*.

8. Yu, N., Genevet, P., Kats, M. A., Aieta, F., Tetienne, J. P., Capasso, F., & Gaburro, Z. (2011). Light propagation with phase discontinuities: generalized laws of reflection and refraction. *science*, *334*(6054), 333-337.

9. Ni, X., Emani, N. K., Kildishev, A. V., Boltasseva, A., & Shalaev, V. M. Broadband light bending with plasmonic nanoantennas. *Science* **335**, 427-427 (2012).

10. Zheludev, N. I., & Kivshar, Y. S. From metamaterials to metadevices. *Nat. Mater.* **11**, 917-924 (2012)Silva, A., Monticone, F., Castaldi, G., Galdi, V., Alù, A., & Engheta, N. (2014). Performing mathematical operations with metamaterials. *Science,343*(6167), 160-163.

11. Tsakmakidis, Kosmas L., Allan D. Boardman, and Ortwin Hess. 'Trapped rainbow' storage of light in metamaterials. *Nature* **450,** 397-401 (2007).

12. Gu, J., Singh, R., Liu, X., Zhang, X., Ma, Y., Zhang, S. & Taylor, A. J. (2012). Active control of electromagnetically induced transparency analogue in terahertz metamaterials. *Nature communications*, *3*, 1151.

13. Sekitani, T., Zschieschang, U., Klauk, H., & Someya, T. Flexible organic transistors and circuits with extreme bending stability. *Nat. Mater.* **9**, 1015-1022 (2010).

14. Wang, L., Uppuluri, S. M., Jin, E. X., & Xu, X. Nanolithography using high transmission nanoscale bowtie apertures. *Nano Lett.* **6**, 36a1-364 (2006).

15. Zheludev, N. I., Prosvirnin, S. L., Papasimakis, N., & Fedotov, V. A. (2008). Lasing spaser. *Nature Photonics*, *2*(6), 351-354.

16. Plum, E., Fedotov, V. A., Kuo, P., Tsai, D. P., & Zheludev, N. I. (2009). Towards the lasing spaser: controlling metamaterial optical response with semiconductor quantum dots. *Optics express*, *17*(10), 8548-8551.

17. Taubert, R., Hentschel, M., Kästel, J., & Giessen, H. (2012). Classical analog of electromagnetically induced absorption in plasmonics. *Nano letters*, *12*(3), 1367-1371.

18. Tassin, P., Zhang, L., Zhao, R., Jain, A., Koschny, T., & Soukoulis, C. M. (2012). Electromagnetically induced transparency and absorption in metamaterials: the radiating two-oscillator model and its experimental confirmation. Physical review letters, 109(18), 187401.

19. Walther, B., Helgert, C., Rockstuhl, C., Setzpfandt, F., Eilenberger, F., Kley, E. B., & Pertsch, T. (2012). Spatial and spectral light shaping with metamaterials. *Advanced Materials*, *24*(47), 6300-6304.

20. Feng, L., Xu, Y. L., Fegadolli, W. S., Lu, M. H., Oliveira, J. E., Almeida, V. R., ... & Scherer, A. (2013). Experimental demonstration of a unidirectional reflectionless parity-time metamaterial at optical frequencies. Nature materials, 12(2), 108-113.

21. Lawrence, M., Xu, N., Zhang, X., Cong, L., Han, J., Zhang, W., & Zhang, S. (2014). Manifestation of P T Symmetry Breaking in Polarization Space with Terahertz Metasurfaces. *Physical review letters*, *113*(9), 093901.

22. N. Yu, P. Genevet, M. A. Kats, F. Aieta, J. P. Tetienne, F. Capasso, and Z. Gaburro, "Light propagation with phase discontinuities: Generalized laws of reflection and refraction", Science **334**, 333–337 (2011).

23. Yu, N., Genevet, P., Kats, M. A., Aieta, F., Tetienne, J. P., Capasso, F., & Gaburro, Z. (2011). Light propagation with phase discontinuities: generalized laws of reflection and refraction. *science*, *334*(6054), 333-337.

24. Sun, S., Yang, K. Y., Wang, C. M., Juan, T. K., Chen, W. T., Liao, C. Y., & Zhou, L. (2012). High-efficiency broadband anomalous reflection by gradient meta-surfaces. *Nano letters*, *12*(12), 6223-6229.

25. Kildishev, A. V., Boltasseva, A., & Shalaev, V. M. Planar photonics with metasurfaces. *Science*, **339,** 1232009 (2013).

26. Yin, X., Ye, Z., Rho, J., Wang, Y., & Zhang, X. Photonic spin hall effect at metasurfaces. *Science*, **339**, 1405-1407 (2013).

27. Aieta, F., Genevet, P., Kats, M. A., Yu, N., Blanchard, R., Gaburro, Z., & Capasso, F. Aberration-free ultrathin flat lenses and axicons at telecom wavelengths based on plasmonic metasurfaces. *Nano Lett*. **12**, 4932-4936 (2012).

28. Yu, N. et al. Flat optics: Controlling wavefronts with optical antenna metasurfaces. *IEEE J. Sel. Top. Quant. Electron*. **19**, 4700423 (2013).

29. Hill, R. T., Mock, J. J., Hucknall, A., Wolter, S. D., Jokerst, N. M., Smith, D. R., & Chilkoti, A. (2012). Plasmon ruler with angstrom length resolution. *ACS nano*, *6*(10), 9237-9246.

30. Jain, P. K., Huang, W., & El-Sayed, M. A. (2007). On the universal scaling behavior of the distance decay of plasmon coupling in metal nanoparticle pairs: a plasmon ruler equation. *Nano Letters*, *7*(7), 2080-2088.

31. Sönnichsen, C., Reinhard, B. M., Liphardt, J., & Alivisatos, A. P. A molecular ruler based on plasmon coupling of single gold and silver nanoparticles. *Nat. Biotechnol.* **23**, 741-745 (2005).

32. Mastroianni, A. J., Claridge, S. A., & Alivisatos, A. P. Pyramidal and chiral groupings of gold nanocrystals assembled using DNA scaffolds. *J. Am. Chem. Soc.* **131**, 8455-8459 (2009).

33. Tabor, C., Murali, R., Mahmoud, M., & El-Sayed, M. A. (2008). On the Use of Plasmonic Nanoparticle Pairs As a Plasmon Ruler: The Dependence of the Near-Field Dipole Plasmon Coupling on Nanoparticle Size and Shape†. *J. Phys. Chem. A*, *113*(10), 1946-1953.

34. Liu, N., Hentschel, M., Weiss, T., Alivisatos, A. P., & Giessen, H. (2011). Three-dimensional plasmon rulers. *Science*, *332*(6036), 1407-1410.

35. Hentschel, M., Schäferling, M., Weiss, T., Liu, N., & Giessen, H. Three-dimensional chiral plasmonic oligomers. *Nano Lett*, **12**, 2542-2547 (2012).

36. Linden, S., Niesler, F. B. P., Förstner, J., Grynko, Y., Meier, T., & Wegener, M. (2012). Collective effects in second-harmonic generation from split-ring-resonator arrays. *Physical review letters*, *109*(1), 015502.

37. Jenkins, S. D., & Ruostekoski, J. (2012). Cooperative resonance linewidth narrowing in a planar metamaterial. *New Journal of Physics*, *14*(10), 103003.

38. Jenkins, S. D., & Ruostekoski, J. (2012). Theoretical formalism for collective electromagnetic response of discrete metamaterial systems. *Physical Review B*, *86*(8), 085116.

39. Jenkins, S. D., & Ruostekoski, J. (2013). Metamaterial transparency induced by cooperative electromagnetic interactions. *Physical review letters*, *111*(14), 147401.

40. Powell, D. A., Lapine, M., Gorkunov, M. V., Shadrivov, I. V., & Kivshar, Y. S. (2010). Metamaterial tuning by manipulation of near-field interaction. *Physical Review B*, *82*(15), 155128.

41. Powell, D. A., Hannam, K., Shadrivov, I. V., & Kivshar, Y. S. (2011). Near-field interaction of twisted split-ring resonators. *Physical Review B*, *83*(23), 235420.

42. Fedotov, V. A., Papasimakis, N., Plum, E., Bitzer, A., Walther, M., Kuo, P., & Zheludev, N. I. (2010). Spectral collapse in ensembles of metamolecules. *Physical review letters*, *104*(22), 223901.

43. Wallauer, J., Bitzer, A., Waselikowski, S., & Walther, M. (2011). Near-field signature of electromagnetic coupling in metamaterial arrays: a terahertz microscopy study. *Optics express*, *19*(18), 17283-17292.

44. Singh, R., Rockstuhl, C., & Zhang, W. (2010). Strong influence of packing density in terahertz metamaterials. *Applied Physics Letters*, *97*, 241108.

45. Chowdhury, D. R., Azad, A. K., Zhang, W., & Singh, R. (2013). Near field coupling in passive and active terahertz metamaterial devices. *Terahertz Science and Technology, IEEE Transactions on*, *3*(6), 783-790.

46. Al-Naib, I., Jansen, C., Singh, R., Walther, M., & Koch, M. (2013). Novel THz metamaterial designs: From near-and far-field coupling to high-q resonances. *Terahertz Science and Technology, IEEE Transactions on*, *3*(6), 772-782.

47. Xu, N., Singh, R., & Zhang, W. (2015). Collective coherence in nearest neighbor coupled metamaterials: A metasurface ruler equation. *Journal of Applied Physics*, *118*(16), 163102.

48. Grischkowsky, D., Keiding, S., Van Exter, M., & Fattinger, C. (1990). Far-infrared time-domain spectroscopy with terahertz beams of dielectrics and semiconductors. *JOSA B*, *7*(10), 2006-2015.

49. Zhang W, "Resonant terahertz transmission in plasmonic arrays of subwavelength holes", The European physical journal applied physics, **43**(01): 1-18 (2008)

50. Fano, U. (1961). Effects of configuration interaction on intensities and phase shifts. *Physical Review*, *124*(6), 1866.

51. Bianconi, A. (2002). Ugo Fano and shape resonances. *arXiv preprint cond-mat/0211452*.

52. Luk'yanchuk, B., Zheludev, N. I., Maier, S. A., Halas, N. J., Nordlander, P., Giessen, H., & Chong, C. T. (2010). The Fano resonance in plasmonic nanostructures and metamaterials. *Nature materials*, *9*(9), 707-715.

53. Kobayashi, K., Aikawa, H., Sano, A., Katsumoto, S., & Iye, Y. (2004). Fano resonance in a quantum wire with a side-coupled quantum dot. *Physical Review B*, *70*(3), 035319.

54. Kobayashi, K., Aikawa, H., Katsumoto, S., & Iye, Y. (2002). Tuning of the Fano effect through a quantum dot in an Aharonov-Bohm interferometer. *Physical review letters*, *88*(25), 256806.

55. Mirin, N. A., Bao, K., & Nordlander, P. (2009). Fano resonances in plasmonic nanoparticle aggregates†. *The Journal of Physical Chemistry A*, *113*(16), 4028-4034.

56. Sonnefraud, Y., Verellen, N., Sobhani, H., Vandenbosch, G. A., Moshchalkov, V. V., Van Dorpe, P., & Maier, S. A. (2010). Experimental realization of subradiant, superradiant, and Fano resonances in ring/disk plasmonic nanocavities. *ACS nano*, *4*(3), 1664-1670.

57. Bachelier, G., Russier-Antoine, I., Benichou, E., Jonin, C., Del Fatti, N., Vallée, F., & Brevet, P. F. (2008). Fano profiles induced by near-field coupling in heterogeneous dimers of gold and silver nanoparticles. *Physical review letters*, *101*(19), 197401.

58. Christ, A., Tikhodeev, S. G., Gippius, N. A., Kuhl, J. & Giessen, H. Waveguideplasmon polaritons: Strong coupling of photonic and electronic resonances in a metallic photonic crystal slab. *Phys. Rev. Lett.* **91,** 183901 (2003).

59. Christ, A. *et al.* Optical properties of planar metallic photonic crystal structures: Experiment and theory. *Phys. Rev. B* **70,** 125113 (2004).

60. Fedotov, V. A., Rose, M., Prosvirnin, S. L., Papasimakis, N., & Zheludev, N. I. (2007). Sharp trapped-mode resonances in planar metamaterials with a broken structural symmetry. *Physical Review Letters*, *99*(14), 147401.

61. Singh, R., Al-Naib, I. A., Koch, M., & Zhang, W. (2011). Sharp Fano resonances in THz metamaterials. *Optics Express*, *19*(7), 6312-6319.

62. Singh, R., Al-Naib, I., Cao, W., Rockstuhl, C., Koch, M., & Zhang, W. (2013). The Fano resonance in symmetry broken terahertz metamaterials. *Terahertz Science and Technology, IEEE Transactions on*, *3*(6), 820-826.

63. Yan, C., & Martin, O. J. (2014). Periodicity-Induced Symmetry Breaking in a Fano Lattice: Hybridization and Tight-Binding Regimes. *ACS nano*, *8*(11), 11860-11868.

64. Liu, H., Genov, D. A., Wu, D. M., Liu, Y. M., Liu, Z. W., Sun, C., ... & Zhang, X. (2007). Magnetic plasmon hybridization and optical activity at optical frequencies in metallic nanostructures. *Physical review B*, *76*(7), 073101.

65. Liu, N., Liu, H., Zhu, S., & Giessen, H. (2009). Stereometamaterials. *Nature Photonics*, *3*(3), 157-162.

66. Sersic, I., Frimmer, M., Verhagen, E., & Koenderink, A. F. (2009). Electric and magnetic dipole coupling in near-infrared split-ring metamaterial arrays. *Physical Review Letters*, *103*(21), 213902.

67. Merlin, R. (2009). Metamaterials and the Landau-Lifshitz permeability argument: large permittivity begets high-frequency magnetism. *Proceedings of the National Academy of Sciences*, *106*(6), 1693-1698.

68. Caniggia, S., & Maradei, F. (2008). *Signal integrity and radiated emission of high-speed digital systems*. Wiley Publishing.

69. Rosa, E. B. (1908). *The self and mutual inductances of linear conductors*. US Department of Commerce and Labor, Bureau of Standards.

70. Wood, R. W. (1902). XLII. On a remarkable case of uneven distribution of light in a diffraction grating spectrum. *The London, Edinburgh, and Dublin Philosophical Magazine and Journal of Science*, *4*(21), 396-402.

71. Wood, R. W. (1902). On a remarkable case of uneven distribution of light in a diffraction grating spectrum. *Proceedings of the Physical Society of London*, *18*(1), 269.

72. Ghaemi, H. F., Thio, T., Grupp, D. E., Ebbesen, T. W., & Lezec, H. J. (1998). Surface plasmons enhance optical transmission through subwavelength holes. *Physical review B*, *58*(11), 6779.

73. Brolo, A. G., Gordon, R., Leathem, B., & Kavanagh, K. L. (2004). Surface plasmon sensor based on the enhanced light transmission through arrays of nanoholes in gold films. *Langmuir*, *20*(12), 4813-4815.

74. Bitzer, A., Wallauer, J., Merbold, H., Helm, H., Feurer, T., & Walther, M. (2009). Lattice modes mediate radiative coupling in metamaterial arrays. *Optics express*, *17*(24), 22108-22113.

75. Wallauer, J., Bitzer, A., Waselikowski, S., & Walther, M. (2011). Near-field signature of electromagnetic coupling in metamaterial arrays: a terahertz microscopy study. *Optics express*, *19*(18), 17283-17292.

76. Wood, R. W. (1935). Anomalous diffraction gratings. *Physical Review*,*48*(12), 928.

77. Zhang, S., Genov, D. A., Wang, Y., Liu, M., & Zhang, X. (2008). Plasmon-induced transparency in metamaterials. *Physical Review Letters*, *101*(4), 047401.

78. Liu, N., Weiss, T., Mesch, M., Langguth, L., Eigenthaler, U., Hirscher, M., ... & Giessen, H. (2009). Planar metamaterial analogue of electromagnetically induced transparency for plasmonic sensing. *Nano letters*, *10*(4), 1103-1107.

79. Papasimakis, N., Fedotov, V. A., Zheludev, N. I., & Prosvirnin, S. L. (2008). Metamaterial analog of electromagnetically induced transparency. *Physical Review Letters*, *101*(25), 253903.

80. Cao, W., Singh, R., Zhang, C., Han, J., Tonouchi, M., & Zhang, W. (2013). Plasmon-induced transparency in metamaterials: Active near field coupling between bright superconducting and dark metallic mode resonators. *Applied Physics Letters*, *103*(10), 101106.

81. Tassin, P., Zhang, L., Koschny, T., Economou, E. N., & Soukoulis, C. M. (2009). Low-loss metamaterials based on classical electromagnetically induced transparency. *Physical review letters*, *102*(5), 053901.

82. Weis, P., Garcia-Pomar, J. L., Beigang, R., & Rahm, M. (2011). Hybridization induced transparency in composites of metamaterials and atomic media. *Optics express*, *19*(23), 23573-23580.

83. Singh, R., Al-Naib, I. A., Yang, Y., Chowdhury, D. R., Cao, W., Rockstuhl, C., & Zhang, W. (2011). Observing metamaterial induced transparency in individual Fano resonators with broken symmetry. *Applied Physics Letters*,*99*(20), 201107.

84. Cao, W., Singh, R., Al-Naib, I. A., He, M., Taylor, A. J., & Zhang, W. (2012). Low-loss ultra-high-Q dark mode plasmonic Fano metamaterials. *Optics letters*, *37*(16), 3366-3368.

85. Sun, Y. Q. Y. Y., Tan, W., Liang, L., Jiang, H. T., Wang, Z. G., Liu, F. Q., & Chen, H. (2012). Metamaterial analog of quantum interference: From electromagnetically induced transparency to absorption. *EPL (Europhysics Letters)*, *98*(6), 64007.

86. Yin, X., Feng, T., Yip, S., Liang, Z., Hui, A., Ho, J. C., & Li, J. (2013). Tailoring electromagnetically induced transparency for terahertz metamaterials: From diatomic to triatomic structural molecules. *Applied Physics Letters*, *103*(2), 021115.

87. Kim, J., Soref, R., & Buchwald, W. R. (2010). Multi-peak electromagnetically induced transparency (EIT)-like transmission from bull's-eye-shaped metamaterial. *Optics express*, *18*(17), 17997-18002.

88. Zhu, L., Meng, F. Y., Fu, J. H., Wu, Q., & Hua, J. (2012). Multi-band slow light metamaterial. *Optics express*, *20*(4), 4494-4502.

89. Drake, G. W. (Ed.). (2006). *Springer handbook of atomic, molecular, and optical physics*. Springer Science & Business Media.

90. Taubert, R., Hentschel, M., & Giessen, H. (2013). Plasmonic analog of electromagnetically induced absorption: simulations, experiments, and coupled oscillator analysis. *JOSA B*, *30*(12), 3123-3134.

91. Tassin, P., Zhang, L., Zhao, R., Jain, A., Koschny, T., & Soukoulis, C. M. (2012). Electromagnetically induced transparency and absorption in metamaterials: the radiating two-oscillator model and its experimental confirmation. *Physical review letters*, *109*(18), 187401.

92. Verslegers, L., Yu, Z., Ruan, Z., Catrysse, P. B., & Fan, S. (2012). From electromagnetically induced transparency to superscattering with a single structure: a coupled-mode theory for doubly resonant structures. *Physical review letters*, *108*(8), 083902.

93. Qu, K., & Agarwal, G. S. (2013). Phonon-mediated electromagnetically induced absorption in hybrid opto-electromechanical systems. *Physical Review A*, *87*(3), 031802.

94. Zhang, X., Xu, N., Qu, K., Tian, Z., Singh, R., Han, J., Agarwal, GS. & Zhang, W. (2015). Electromagnetically induced absorption in a three-resonator metasurface system. *Scientific reports*, *5*.

95. Lu. X, Studies of surface plasmons and localized surface plasmons at terahertz frequencies, Thesis (2008).

96. Chen, H., Zhang, J., Bai, Y., Luo, Y., Ran, L., Jiang, Q., & Kong, J. A. (2006). Experimental retrieval of the effective parameters of metamaterials based on a waveguide method. *Optics Express*, *14*(26), 12944-12949.

VITA

Ningning Xu

Candidate for the Degree of

Doctor of Philosophy

Thesis: COLLECTIVE COHERENT BEHAVIOR AND CLASSICAL ANALOGUE OF QUANTUM PHENOMENA IN TERAHERTZ METASURFACES

Major Field: Photonics

Biographical:

Education:

Completed the requirements for the Doctor of Philosophy in Photonics at Oklahoma State University, Stillwater, Oklahoma in May, 2016.

Completed the requirements for the Master of Science in photonics and technology at Nankai University, Tianjin, China in 2010.

Completed the requirements for the Bachelor of Science in physics at Jilin University, Changchun, Jilin in 2006.

Experience: Research assistant, School of Electrical and Computer Engineering in Oklahoma State University, 2012-2016.
Teaching assistant, Department of Physics in Oklahoma State University, 2010-2012.
Visiting student, Department of Physics in University of Arkansas, 2009-2010.

Professional Memberships: OSA Student Membership